Design and fabrication of a continuous flow mixer for investigating protein folding kinetics using focal plane array Fourier transform infrared spectroscopy

Moeed Haq

Master of Science

Department of Food Science and Agricultural Chemistry
McGill University
Montreal, Quebec, Canada

A thesis submitted to the Faculty of Graduate Studies and Research in partial fulfillment of the requirements of the degree of Master of Science

August 2008

Your file Votre référence
ISBN: 978-0-494-67035-4
Our file Notre référence
ISBN: 978-0-494-67035-4

ABSTRACT

This thesis presents the design, fabrication, and testing of a micromixing device intended for use in investigating protein dynamics on a microsecond timescale by Fourier transform infrared (FTIR) spectroscopy. Numerical modeling of flow was implemented to predict the influence of flow rates and geometric variations on mixing performance in three passive mixers. The simulation models were validated by experimental measurements using optical and infrared detection. The optimum level of mixing was observed in a multi-lamination mixer that combined thin filaments of differing fluids in an alternating manner. The multi-laminates were transferred onto polished calcium fluoride infrared-transparent optical windows by lithographic processing of an Epon-based polymer, SU-8. A rigid seal between two microchannels was accomplished through thermal bonding of an unexposed resist layer, which acted as a thermal epoxy under the influence of temperature. The multi-lamination mixer was used to study the changes in the secondary structure of β-Lactoglobulin in deuterated phosphate buffer under varying physicochemical conditions by time-resolved FTIR spectroscopy using focal plane array detection. Upon a pH jump from pH 2 to neutral pH, a gradual loss of α-helical content, accompanied by an increase in random coils and turns was observed within 2 ms of mixing. In a second kinetic experiment, mixing of a neutral-pH solution of β-Lactoglobulin with a 60% trifluoroethanol solution resulted in the formation of an α-helical intermediate with an accompanying increase in intramolecular β-sheet structure within 500 μs of mixing. These results indicate that the multi-lamination mixer designed and fabricated in this study is well suited for investigations of protein dynamics on the micro- to millisecond timescale by time-resolved FTIR spectroscopy.

SOMMAIRE

Cette thèse démontre la conception, la fabrication et l'évaluation d'une micro-chambre de mixage pour l'étude de la dynamique de réactions des protéines sur l'échelle de la microseconde, par spectroscopie infrarouge à transformée de Fourier (FTIR). Une modélisation numérique de l'écoulement de fluide a été utilisée pour évaluer l'influence du flux et la de géométrie de la chambre de mixage sur la performance de trois procédés passifs de mélange. La modélisation a été validée par des mesures expérimentales utilisant des détecteurs optique et infrarouge. Le niveau optimum de mélange a été atteint en utilisant un processus de mélange multi-laminaire combinant par alternation de fins filaments de différents fluides. Les unités multi-laminaires ont été transférées sur des surfaces optiques de fluorure de calcium transparent à l'infrarouge par un processus lithographique utilisant un polymère à base de Epon SU-8. Un scellage thermique effectué par activation de résine époxy assure l'étanchéité des micro-canaux. Le mixeur multi-laminaire a été utilisé dans l'étude des changements dans la structure secondaire de la β-Lactoglobuline dans une solution tampon de phosphate deuterée sous différentes conditions physico-chimiques par spectroscopie FTIR avec un détecteur plan focal. Quand le pH passe de 2 à neutre, on observe, en dedans de 2 ms après le mélange, une perte graduelle du contenu α-hélicoïdal qui s'accompagne d'une augmentation des structures désordonnées et aléatoires. Lors d'une deuxième expérience cinétique, le mélange d'une solution neutre de β-Lactoglobuline avec une solution 60% de trifluoroéthanol a produit un intermédiaire α-hélice avec une augmentation de la structure couche- β intramoléculaire en l'espace de 500 μs. Ces résultats démontrent que le système de mixage multi-laminaire développé et utilisé pour cette recherche serait approprié dans l'étude de la dynamique des protéines dans l'ordre de la milli à la microseconde, par spectroscopie infrarouge à transformés de Fourier (FTIR).

ACKNOWLEDGEMENTS

I would like to express my sincere gratitude to my supervisor, Dr Ashraf Ismail, for providing me with an opportunity to explore the emerging field of microfluidics. His continued support and encouragement was the invaluable glue that held things together even when the epoxy didn't. I also wish to thank Dr Jacqueline Sedman for her suggestions and insight, as well as for her careful editing of my thesis. Additional thanks are extended to the members of the Food Science Team: Andrew, Ahmed, Alex, Laura, Pedro, and Zubair, who helped me with my experiments.

Furthermore, I would like to acknowledge the staff members at McGill's Nanotools facility for their technical support and expertise. Special thanks go to Donald Berry and Neal Lemaire for their assistance in my training and for providing creative solutions for day-to-day fabrication needs. In addition, I appreciate the valuable contributions made by Matthieu Nannini and Vito Logiudice which were critical for the success and development of the fabrication recipe.

Finally, I wish to thank my family for their continuous support and patience. I am forever indebted to my parents for encouraging my educational pursuits.

TABLE OF CONTENTS

LIST OF FIGURES

LIST OF TABLES

LIST OF ABBREVIATIONS

ANS – 1-anilino-8-naphthalene sulfonate

BLG – β-lactoglobulin

CaF2 – Calcium fluoride

CCD – Charged coupled device

CD – Circular dichroism

CF – Continuous-flow

CNC – Computer numerical control

FPA – Focal plane array

FTIR – Fourier transform infrared

HF – Hydrofluoric acid

HMDS – Hexamethyldisilazane

IPA – Isopropanol

LIF – Laser induce fluorescence

NaOD – Dueterated Sodium Hydorxide

NMR – Nuclear magnetic resonance

Pe – Peclet number

PEB – Post exposure bake

PEEK –Polyetheretherketone

PGMEA – Propylene glycol methyl ether acetate

PR – Photoresist

Re – Reynolds number

SAXS – Small angle X-ray scattering

SB – Softbake

SF – Stopped-flow

SNR – Signal to noise

TFE – Trifluoroethanol

Trp – Tryptophan

μTAS – Micro-Total Analysis Systems

WiW – Within Wafer

WtW - Wafer to Wafer

1. Introduction

1.1 Background

In recent years, the miniaturization of analytical instruments has led to the realization of micro-Total Analysis Systems (μTAS) that integrate several laboratory functions on a single microchip. A typical chip includes a micropump that dispenses sub-microliter volumes of liquid into a microfluidic network where it is subjected to various sample preparation procedures such as filtration, enrichment, separation, and mixing. An on-chip chemical sensor then monitors the progress of the chemical and biological processes under investigation. The use of automated dispensers and on-chip sensors minimizes the possibility of human error from the experiment. At the same time, it reduces analysis times and improves the likelihood of detecting low concentration levels. Since the microfluidic network requires small amounts of reagent, the cost of experimentation is greatly reduced. These networks can provide a safe platform for conducting potentially hazardous chemical experiments while reducing the amount of waste production.

Rapid mixing of reagents is perhaps the most commonly implemented procedure within μTAS. It is essential for initiating biological processes such as enzyme catalysis, protein folding, and ligand interaction that occur on the sub-millisecond timescale. However, the miniaturization of channels results in an alteration of flow phenomena causing a suppression of inertial effects by viscous forces. These effects are crucial for generating turbulence to achieve efficient mixing. In their absence, the flow profile in microchannels falls within the laminar regime, where mixing is primarily achieved by diffusion. In order to increase the mixing efficiency of fluids in microchannels, several mechanisms utilizing active or passive means have been proposed and implemented.

1.2 Rationale & Objective

1.2.1 Rapid Mixing

The ability to mix microliter volumes of liquid in microchannels is obstructed by the prevalence of laminar flow conditions. Under these conditions, fluid segmentation is restricted and a significant amount of time is required to form of a homogenous blend between two liquids. One method to accelerate mixing relies on a reduction in microchannel dimensions to increase the diffusive penetration of molecules between liquid streams. However, such a reduction increases the pressure drop within the channel, which consequently opposes the flow of liquid. For practical reasons, the

dimensions of the microchannel are optimized to permit adequate fluid actuation through a pressure-driven mechanism.

Active means of enhancing mixing efficiency rely on the use of external agents to push the flow profile towards turbulence. Transient pulsing, ultrasonic and acoustic agitation, mechanical stirring, and electrokinetic vibration of fluid are some of the active methods designed to facilitate mixing in microchannels (Green et al., 2007). In contrast, passive methods employ geometric variations in mixer design to alter the flow profile. Popular techniques include multi-lamination, flow focusing, flow obstruction, and chaotic mixing (Nguyen and Wu, 2005). Both active and passive techniques seek to increase molecular diffusion by enhancing the contact surface and diminishing the diffusion distance between adjacent fluid streams.

While active mixers have an edge over passive devices in terms of mixing efficiency, they are difficult to fabricate and require external power sources for operation. Furthermore, active mixers can generate electric fields and heat during operation, which may damage biological samples present within the fluid. On the other hand, passive devices are easier to fabricate and can withstand mechanical wear and tear. In light of the advantages offered by passive mixers, the focus of this thesis is on developing a microchannel device capable of passively mixing two liquids in the shortest time possible.

1.2.2 Detection

The second objective of this study is to use the mixing capability of the microfluidic device to rapidly alter the chemical environment of a protein sample. The time evolution of conformational changes within the protein will be probed by a suitable detection technique.

As mentioned before, a miniaturized total analysis system must have on-chip detection capabilities for monitoring ultra-low concentration levels of analytes. There have been numerous attempts to integrate various detection schemes with microfluidic systems; however, results have been less than satisfactory due to scaling issues. Two on-chip methods that have gained prominence in recent years are electrochemical and optical detection. The former technique measures the electrical response of redox species via embedded microelectrodes, while the latter technique uses photodiodes to monitor light-induced changes in photoactive compounds (Schwarz and Hauser, 2001).

Given the inherent difficulty of integrating detection elements with microfluidic systems, researches have had to rely on traditional off-chip methods for detection. Most studies have

reported the use of optical methods, which offer a non-invasive, real-time approach for following dynamic events in sample volumes. Depending on the wavelength of light, these optical methods are classified into various spectroscopic techniques, namely ultraviolet-visible absorbance, fluorescence, infrared absorbance, and Raman scattering. A survey of the literature indicates laser-induced fluorescence (LIF) as the dominant optical detection technique in microfluidics (Reyes et al., 2002).

Due to the linear dependence of light absorbance on channel pathlength, a scale down of channel dimension for microfluidic applications decreases the sensitivity of absorbance detection techniques. Compared with absorbance spectroscopy, LIF continues to achieve high sensitivity and low detection limits even at smaller channel pathlengths. This is attributed to a precise control over emission and excitation wavelengths that reduces signal interference from other species. However, fluorescence spectroscopy has its shortcomings in that most biological compounds, for example proteins, do not exhibit natural fluorescence, and therefore require derivatization with fluorophores. This time-consuming and costly process limits the applicability of fluorescence detection.

Infrared spectroscopy provides an alternate detection technique suitable for analyzing biological species confined to small pathlengths. The technique avoids costly sample preparation procedures such as labeling or covalent modification, and it provides a means for sampling biomolecules in their native state. It is based on the interaction of infrared light with the vibrations of chemical bonds leading to a change in the dipole moment of the molecule. Since large molecules, such as proteins, have vibrational contributions from an enormous number of chemical bonds, infrared spectroscopy cannot detect contributions from individual bonds. Instead the molecular vibrations are localized to specific modes, among which the backbone amide I mode is the most widely studied in infrared spectroscopy. This mode, contained in the mid-infrared spectrum, can be used as an effective marker to monitor protein folding events due to its sensitivity to hydrogen bonding, dipole-dipole interactions, and backbone conformations (Krimm and Bandekar, 1986).

1.2.3 Time Resolved Fourier Transform Infrared Spectroscopy

The past two decades have seen infrared spectroscopy make a transition from dispersive instruments to Fourier transform spectrometers to obtain faster and more accurate chemical information from small spatial domains. The absence of entrance and exit slits in FTIR spectrometers minimizes signal attenuation, which consequently allows greater discrimination between smaller spectral peaks. At the same time, an indirect approach of measuring the temporal coherence of the infrared light source through a Michelson interferometer allows all frequencies

present in the infrared domain to be measured simultaneously. This has enabled conventional mercury cadmium telluride (MCT) detectors, operating with a mirror velocity of 6 cm/s and a spectral resolution of 4 cm^{-1}, to complete one scan in 25 μs. However, the need to acquire high-resolution spectra requires averaging of consecutive scans. This time consuming process not only limits the temporal resolution of the technique to the millisecond domain, but it also requires a triggering method capable of repeatedly initiating the biological process under investigation (Lüdeke et al., 2006).

One approach for pushing the time resolution of FTIR spectroscopy to the microsecond domain involves the use of a synchrotron light source for sample irradiation. The superior spectral brightness and collimation of the light beam enables the acquisition of high resolution (in terms of S/N) data with fewer scans (Kulka et al., 2004). However, the high cost related to synchrotron radiation makes this technique impractical. A more elegant approach for enhancing temporal resolution involves rapid mixing of solvents within a microfluidic channel. The progress of the reaction is monitored at various points within the channel by translating the infrared beam in the x-y plane. With knowledge of the beam diameter and flow rate along the channel, the series of spectra acquired from various locations can be separated in time (Kauffmann et al., 2001). Thus, the time resolution of the technique is determined by flow rates and infrared beam diameter.

The integration of multi-element focal plane array (FPA) detectors to FTIR spectrometers has opened up the possibility of simultaneously acquiring numerous spectra with excellent spatial resolution over a large sampling region. Despite this increase in spatial resolution, the imaging technique suffers in the context of temporal resolution from time loss due to signal averaging. This problem is compounded by the presence of additional detector elements that consume extra time for signal acquisition. However, both these limitations can be overcome by coupling an infrared imaging system to a continuous flow microfluidic mixer. With this approach, the time resolution of detection is determined by the spatial distance between detector elements and the flow rate.

By combining FTIR-FPA spectroscopy with microfluidic mixing, it is theoretically possible to achieve a sub-100 microsecond time resolution. For instance, a typical 32x32 detector FPA yields a spatial resolution of 6 μm. With this spatial resolution, it is possible to image a fluid sample, moving at a linear flow rate of 0.1 m/s, with a 60 μs temporal resolution. This time resolution is sufficient to follow the early kinetic events encountered during protein folding.

1.2.4 Protein Folding: Hypothesis and Experimental Verification

Time-resolved studies of protein folding date back to 1961 when Anfinsen conducted his classical experiment aimed at understanding the fundamental processes that govern a protein's ability to fold to its native state from a random coil (Anfinsen et al., 1961). In the years following that experiment, numerous theoretical models have been proposed that predict the nature of protein folding. Most of these models propose a hierarchic folding mechanism where: (i) the native structure sequentially forms around a nucleus, or (ii) a collapsed state with native-like secondary structure accumulates initially, followed by formation of native elements.

Experimental evidence suggests that under appropriate conditions, a protein spontaneously folds to its native state within a few seconds. Peptides with less than a 100 residues fold into a helix without intermediates in a two-state transition. The process usually occurs within 100 μs and involves a rapid compacting of the random coil (Kubelka et al., 2004). Conversely, large proteins often fold through intermediary stages, which can either exist on the folding pathway, or as an off-pathway kinetic trap. Since these reactions occur in the sub-millisecond time domain, the exact nature of the intermediates can be investigated by spectroscopic methods.

A circular dichroism (CD) study of the milk protein β-Lactoglobulin suggests the formation of a burst phase intermediate in the first 18 ms of folding from a denatured state (Kuwajima et al., 1996). Due to the significant dead time of the experiment, important kinetic information within the first 18 ms could not be obtained. Nonetheless, the intermediate is seen to possess non-native α-helices that transition to β-sheets in the later stages of folding. Due to this unusual result, researchers have postulated a non-hierarchic mechanism involved in folding of β- Lactoglobulin.

As a final objective, this thesis will attempt to confirm the results of circular dichroism studies by investigating the folding mechanism of β- Lactoglobulin by time-resolved FTIR spectroscopy.

1.3 Thesis Outline

Chapter 1 delved into the background of μTAS and discussed the objective and rationale of implementing time resolved FTIR spectroscopy for probing dynamic events in microfluidic mixers.

Chapter 2 reviews the fundamentals of microfluidics with an emphasis on the complexity of mixing fluids at low Reynolds number.

Chapter 3 examines the available literature on the design and fabrication of microfluidic mixers. It opens with a brief comparison of rapid mixing techniques with other triggering methods such as

temperature-jump and pressure-jump. Next, the focus turns to passive mixing strategies that have been implemented to achieve ultra-rapid, homogenous mixing. The final section explores the fabrication methods designed for glass and crystalline substrates and concludes with a review of various detection probes employed for observing protein folding kinetics.

Chapter 4 presents a detailed explanation of the various processes encountered during device fabrication and reports on the optimization procedures implemented to create a reproducible model.

Chapter 5 assesses the mixing performance of three passive micromixers through numerical modeling and subsequent experimental validation. A multi-lamination mixer is identified as having a superior mixing efficiency compared to the other two mixers.

Chapter 6 reports the experimental methodology and subsequent results obtained from two experiments aimed at investigating secondary structure modifications in β-Lactoglobulin. The multi-lamination mixer from Chapter 5 is used to trigger a monomer→dimer transition of an acidified protein solution by a rapid pH jump from pH 2 to neutral pH. For the second experiment, a native protein is rapidly mixed with trifluoroethanol (TFE) and the progress of the reaction is monitored by FPA-FTIR spectroscopy.

2. Theoretical Aspects of Micromixing

2.1 Overview

From a distance, microfluidics may seem like a miniature version of its macroscale counterpart; however, scaling brings forward some aspects of fluid dynamics that could easily be neglected in the macroscopic domain. As a result, certain equations describing the physics of conventional, macroscopic systems need to be abandoned before considering flow phenomena on small scales. Developing a sound intuition regarding the effects occurring on the microscale is essential for establishing microfluidic functionalities such as fluid mixing, separation and transport.

Mixing begins with the segmentation of two homogeneous fluids into a heterogeneous blend of finely dispersed elements between which diffusion occurs to yield a homogeneous sample. Diffusion, by its nature, is a random process and hence requires significant time to complete. Nonetheless, mixing can be accelerated with a reduction in the size of the dispersed elements such that the area available for diffusion increases. At a macroscopic scale, this is achieved through high-speed convection mixing involving turbulence. Unfortunately, fluid flow in microchannels is dominated by viscous forces that restrict segmentation. Thus, with knowledge of flow phenomena occurring at microscale, other techniques need to be developed to enhance mixing.

2.2 Flow Regimes

Flow is usually characterized as one of two regimes: laminar or turbulent. The distinction between these regimes is described by the Reynolds number (Re), which relates the inertial forces to the viscous forces acting on the fluid. Inertial forces stem from the inherent momentum of the fluid particles, while intermolecular interactions and friction between fluid molecules and the walls of the container account for viscous effects.

In laminar flows, characterized by a low Reynolds number, the adjoining layers of fluid move parallel to one another. Viscous forces within these layers cause a slowdown of all transport processes since the transfer of momentum, heat and mass has to rely on molecular diffusion (Hardt and Schonfeld, 2007). At higher Reynolds number, inertial effects start to destabilize the regular flow patterns, resulting in unpredictable, irregular turbulent flow. While transport processes increase substantially as a result, more energy needs to be expended to offset the large pressure drops encountered during chaotic flow.

The transition from the laminar to the turbulent regime occurs at a critical Reynolds number of 2300 for liquid flows in circular pipes. The Reynolds number is defined as Equation 2-1:

$$Re = \frac{v_s D}{\nu} \qquad \text{Equation 2-1}$$

where v_s and ν are the average velocity and viscosity of the fluid, respectively, and D is the diameter of the circular channel. In case of a rectangular channel of width a and height b, the diameter is represented by Equation 2-2:

$$D = \frac{2 \times a \times b}{a+b} \qquad \text{Equation 2-2}$$

For microfluidic devices, the channel dimensions typically range from 1 to 100 μm in width and height. Moreover, aqueous solvents are usually driven at flow velocities below 0.1 m/s. Inserting these values into Equation 2-1 yields a Reynolds number of 10, thus indicating the laminar nature of microscale flows. Consequently, mixing between adjacent fluid streams flowing through a microchannel relies on diffusion only.

2.3 Microscale Transport Processes

2.3.1 Diffusion

In the absence of an external field, liquid and gas molecules have a tendency to randomly move about their central position through a stochastic process termed Brownian motion. Intermolecular collisions resulting from this movement tend to confine the molecules; however, the absence of any restoring force allows them to move about freely. The statistical outcome of this random process is referred to as diffusion. By its nature, diffusion tends to increase entropy and is therefore thermodynamically favorable.

The mathematical basis for diffusion was developed by German scientist Adolf Fick, who used a semi-permeable permeable membrane to observe the movement of particles from a region of high concentration to a region of low concentration. He concluded that the diffusion rate (j) was proportional to the diffusion coefficient D, the area available for diffusion A, and the concentration gradient with respect to distance (Equation 2-3):

$$j = -DA\frac{\partial c}{\partial x} \qquad \text{Equation 2-3}$$

Hence it is theoretically possible to increase the diffusion rate by increasing either one of these factors. The diffusion coefficient for large spherical molecules was derived by Einstein as Equation 2-4:

$$D = \frac{kT}{\gamma} \qquad \textbf{Equation 2-4}$$

where k is the Boltzmann constant, T is the absolute temperature, and γ is the frictional constant. Equation 2-4 shows the temperature dependence of the diffusion coefficient, with elevated temperatures favoring the process of diffusion.

Einstein went further to characterize the random behavior of single molecules by relating their displacement (x) to their diffusion coefficient (Equation 2-5):

$$x = \sqrt{2Dt} \qquad \textbf{Equation 2-5}$$

This equation has been particularly helpful in designing microfluidic devices geared towards diffusive mixing. By reducing the width of the channel, which equates to reducing molecular displacement (x), the diffusion time (t) between molecules in adjacent streams can be reduced by two orders of magnitude (Wang et al., 2002).

2.3.2 Advection

In fluids, convective heat and mass transfer takes place through the process of diffusion, discussed above, as well as by advection, which involves mass transport by large-scale motion of currents in the fluid. The transport of pollutants on the surface of a river is an example of advection.

In microscale flows, the transport of fluid particles along the channel is predominantly due to advection. This can be established by examining the Peclet number (Pe), which is the ratio between mass transport due to advection along the channel and mass transport by diffusion across the channel. Molecules within a fluid element, having moved a distance Z along the channel via advection, will require time (t_d) to diffuse across the channel width (d). This scenario is depicted in Figure 2-1.

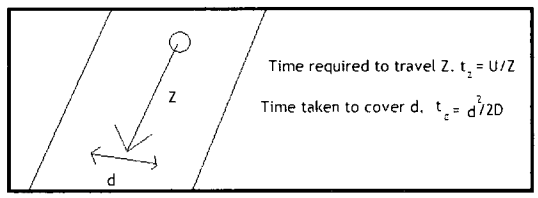

Figure 2-1: Relationship between advection and diffusion

By equating the time taken for the two processes, and recognizing that channel width is proportional to advection distance Z, a relationship between advection and diffusion can be formulated (Equation 2-6):

$$Pe = \frac{U_o d}{D} \qquad \text{Equation 2-6}$$

Despite their small channel widths (d) and low flow rates (U_o), microfluidic devices tend to have a Pe >> 1. This amplification can be attributed to the low diffusivity coefficient D associated with molecules ($\sim 10^{-9}$ m^2/s). A high Peclet number indicates the dominance of advection in microflows, and consequently long channel lengths are required for diffusion-based mixing between adjacent streams to complete in acceptable time-scales.

2.3.3 Chaotic Advection

A primary precursor to efficient mixing is the chaotic stretching and folding of fluid elements brought about by turbulence. These inertial effects are dampened in microscale flows where the integrity of fluid streams is maintained by a linear flow profile. Hence the notion that laminar flows can produce chaotic particle trajectories to quell viscous linearity had a profound effect in the development of micromixers.

Termed chaotic advection, the concept was introduced by Aref in 1990 and involves the formation of transverse flows that exponentially stretch, fold and break fluid elements (Aref, 1990). These transverse flows can be generated actively through an external disturbance or passively by structural features. The latter approach employs periodic changes (intervals) in the geometry of the microchannel or exploits boundary layer effects to generate secondary flows. At each regular interval, the fluid elements are stretched into thinner laminae causing their surface areas to increase relative to their volumes. A large concentration gradient ($\partial c/\partial x$) develops as a result. Next, the laminae are reoriented with the aid of secondary flows, thereby causing the interfacial area (A) between them to increase substantially. Both these effects accelerate the rate of diffusion according to Equation 2-3. The impact of chaotic advection on the concentration profiles of two adjacent streams is illustrated in Figure 2-2.

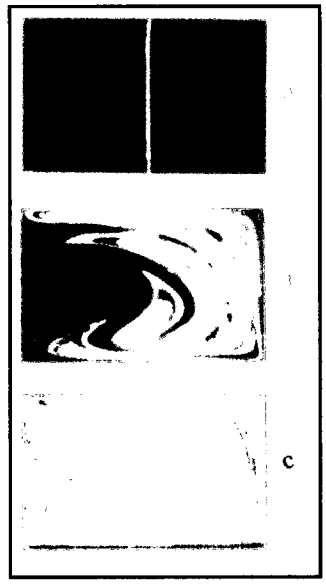

Figure 2-2: Chaotic advection between two fluid streams (Wiggins and Ottino, 2004)

2.4 Summary

With a scale down of device size, viscous forces, which played an insignificant role at macroscopic dimensions, start to surface in microfluidic systems. Consequently, the flow of liquids is restricted to the laminar regime where mass and heat transfer has to rely on molecular diffusion to be effective. This time-consuming process is impractical for μTAS applications, which require ultra-fast mixing of reagents prior to detection. Hence mixing at small scales is an engineering challenge that requires innovative solutions to overcome the dominance of laminar flow conditions and enhance diffusion rates.

From a review of transport processes occurring in microscale devices, it is concluded that diffusion rates are governed by three factors, namely diffusion coefficient, area available for diffusion, and concentration gradient. Since diffusion coefficients are sensitive to thermal changes, a rapid temperature jump can enhance diffusion rates between adjacent liquids. However, this approach is not suitable for microfluidic systems because temperature gradients tend to neutralize rapidly. In contrast, an increase in concentration gradient or an increase in diffusion area can lead to favorable diffusion rates. Both approaches have been utilized in various mixer designs, which are presented in Chapter 3.

3. Literature Review

3.1 Overview

This chapter surveys the available literature concerning mixer design and fabrication techniques. It opens with a brief comparison of rapid mixing techniques with other triggering methods such as temperature and pressure jump in the context of protein folding studies. In section 3.3, the focus turns to passive mixing strategies that have been implemented to achieve ultra-rapid, homogenous mixing. Fabrication methods designed for glass and crystalline substrates are discussed in section 3.4, followed by a review of detection probes for protein folding experiments in section 3.5.

3.2 Rapid Initiation of Protein Folding Reactions

In order to capture the kinetic events occurring during the early stages of the protein folding process, it is essential to induce a rapid change that pushes the conformational equilibrium of a protein towards strongly stabilizing conditions. Such a change can come in the form of a laser-induced temperature jump that can induce folding of proteins from cold-denatured states (Colley et al., 2000). However, sudden changes in temperature can interfere with signals of the detection probe or induce cavitation in solutions with low vapor pressure (Chen et al., 2005). A second triggering method exploits the expansive force of piezoelectric crystals to generate a pressure jump. This jump is strong enough to fold a protein from its cold-denatured state (Jacob et al., 1999). The technique however requires the application of large electrical voltages to elicit an optimum crystal expansion.

Triggering Method	Dead Time	Comments
Temperature Jump	nanoseconds	Applicable to cold denatured proteins
Pressure Jump	micro to milliseconds	Not strong enough to unfold proteins
Rapid Mixing	micro to milliseconds	Applicable to all proteins

Table 3-1: Comparison between various triggering methods

In contrast to the above two methods, rapid mixing of solutions is an elegant technique for initiating events. It avoids significant heating or application of extreme voltages, and it is universally applicable to all proteins. The approach can initiate folding or unfolding of proteins by a rapid change in solvent conditions (pH, denaturant concentration, etc). Table 3-1 compares the three triggering methods in terms of achievable dead times.

3.2.1 Rapid Mixing

The earliest experiment involving rapid mixing was carried out in stopped-flow mode to study kinetic events on millisecond timescales (Chance et al., 1964). The technique has prospered since that time, and is now readily integrated with analytical instruments allowing researchers to monitor events via optical (fluorescence, IR, UV) and biophysical (NMR, SAXS) probes (Arai et al., 2002, Balbach et al., 1997). A typical experiment begins with purging and filling the flow cell with a mixture of denatured protein and refolding buffer solution. The small dimensions of the flow cell and slow fluid velocity ensure the presence of laminar flow conditions, which keep mixing to a minimum. A transistor-transistor-logic (TTL) electronic pulse halts the supply of fluid to the flow cell. An ensuing shockwave that propagates through the fluid mixture facilitates the diffusion of molecules and initiates the folding process. The physical limitations of mixing small volumes of fluid by diffusion alone restrict the time resolution of stopped-flow methods to millisecond timescales. Precious milliseconds are consumed while waiting for the flow to come to a complete halt before data acquisition can begin. To further complicate things, artifacts such as cavitation, vibrations and thermal gradients, which stem from an abrupt flow arrest, obscure detection of the early stages of the reaction (Roder and Shastry, 1999).

Compared with stopped-flow methods, continuous-flow (CF) mixing techniques can reduce dead times by an order of magnitude and avoid artifacts related to stopping of flow. Although the approach was explored as early as 1985 (Regenfuss et al., 1985), it did not gain popularity until recent years. This was partly due to the lack of suitable fabrication techniques, which resulted in inefficient mixers. Newer-generation CF mixers incorporate three-dimensional elements into their design as a means of reducing mixing time to less than 50 μs (Bilsel et al., 2005). In order to induce distortions in the laminar flow profile and help improve mixing efficiency, these elements require high flow rates. Hence CF mixing techniques often consume high volumes of reagent and suffer from a significant buildup of back pressure. To counter this pressure buildup, a large force needs to be applied to push the liquids through the mixer. Such a force can jeopardize the structural integrity of the mixing device in extreme cases. In one instance, high flow rates caused variations in the optical path length of the mixer, which restricted quantitative analysis based on absorbance detection (Holden et al., 2003). Furthermore, the effect of shear forces resulting from high flow rates on the structural composition of proteins needs to be considered.

Traditional detection techniques relied on point-by-point sampling of reaction kinetics downstream from the mixer that resulted in additional reagent consumption (Roder et al., 2006). However, newer approaches involve simultaneous detection of large sampling regions using array detectors (Kaun et al., 2006, Shastry et al., 1998). Simultaneous sampling not only reduces reagent consumption but also allows signal averaging that can significantly improve data quality. Other efforts to improve signal response for continuous-flow mixing techniques have relied on increasing protein concentration and using synchrotron radiation sources (Carr et al., 1995, Fabian and Naumann, 2004).

3.3 Passive Micromixing Strategies

3.3.1 T/Y Junction Mixers

These devices use a junction to bring together two streams that flow alongside each other down a mixing channel. Mixing occurs at the junction due to chaotic interactions between the colliding streams, and across the interface from diffusion of reactant molecules. Based on flow rates, researchers have characterized three distinct mixing regimes (Figure 3-1) inside the mixer (Engler et al., 2004). At low flow rates, the fluid streams flow as smooth streamlines that follow the geometry of the mixer. Within this stratified flow regime ($Re < 40$), mixing is diffusion limited, and a long mixing channel is required to increase the residence time of adjacent streams. As flow rates are increased to moderate Reynolds numbers ($50<Re<150$), vortices begin to form at the junction that swirl flow profiles and increase the diffusion area. Although higher flow rates would normally decrease mixing efficiency because of the shorter residence time between adjacent streams, the stretching and distortion of flow profiles resulting from vortex formation has a positive effect on mixing performance. At even higher flow rates ($Re>150$), a complete breakdown of streamline flow pattern gives way to engulfment flow. Adjacent streams separate from the walls at the junction and intermingle with each other down the mixing channel, which leads to an exponential increase in mixing efficiency. Although high flow rates tend to favor mixing due to chaotic flow profiles, the homogeneity of mixing is adversely affected, and large islands of unmixed regions are observed in the mixing channel downstream from the junction (Kockmann et al., 2006).

Another group of researchers investigated the influence of geometrical variations of a T-junction mixer on the mixing performance of gases (Gobby et al., 2001). Based on results from numerical simulations, the group was able to establish a link between aspect ratio (height:width) of

the mixer and mixing length. At low aspect ratio, wall shear prevents adjacent streams from interacting with each other, and the mixer requires a long channel for adequate mixing. As the aspect ratios are increased, diffusion of gaseous molecules across the interface gains prominence, until a

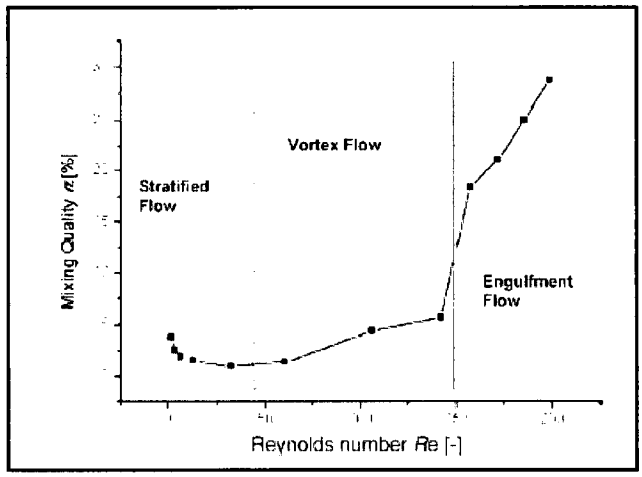

Figure 3-1: Three distinct mixing regimes of T-Mixer (Engler et al., 2004)

limiting value of 1.5 is reached after which diffusion remains unaffected. The authors also observed that a variation of the inlet branches with respect to the horizontal plane had a marginal effect on mixing performance. A +45° oriented mixer required a 2.03 mm long mixing channel for complete mixing, while a -45° oriented mixer required 2.12 mm (Figure 3-2). Moreover, the inverse Y-mixer displayed stagnant zones that contributed to dead volume.

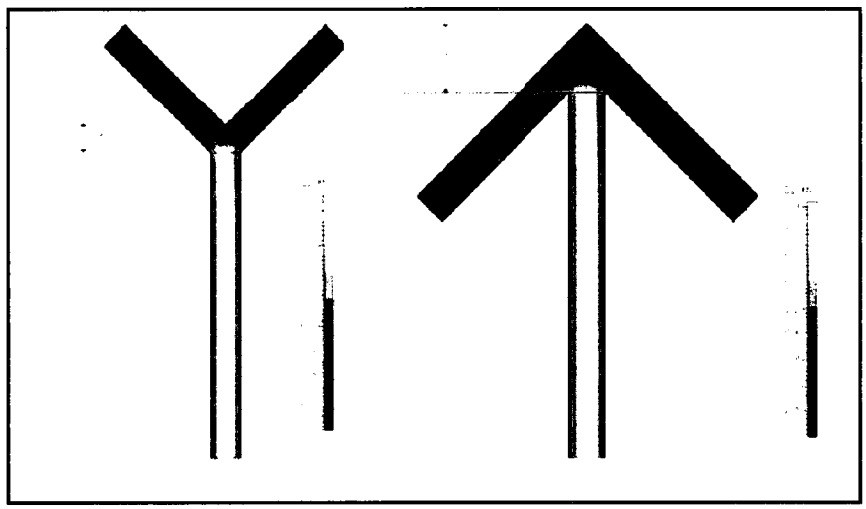

Figure 3-2: Mass fraction contours showing the distribution of tracer within the microchannel of a Y-Junction mixer (Gobby et al., 2001)

Small modifications within the mixing channel of T-junction mixers can have dramatic consequences on mixing performance. A group of researchers included static structures along the walls of the mixing channel to improve mixing efficiency and reduce unmixed regions observed at high flow rates (Wong et al., 2003). These structures are thought to play an important role in the generation of eddies and lateral velocity components that disrupt the streamline flow pattern. Such a disruption leads to the creation of a large contact area that allows molecules to diffuse more rapidly between adjacent fluid streams. At the same time, the phenomenon of boundary layer separation and reattachment in regions around these structures ensures homogenous mixing. However, a major drawback of incorporating static elements within the mixing chamber involves large pressure drops along the channel. Hence high flow rates are required to counter the fluidic resistance stemming from these structures.

3.3.2 Multiple Lamination Mixers

While T/Y junction mixers normally combine two adjacent streams, multi-lamination mixers integrate multiple streams in a single channel to create alternating layers of differing fluids. This leads to a substantial increase in the area available for diffusion. Multi-lamination can be achieved either through distributive mixing where two streams are physically split into smaller filaments and then rejoined in an interdigital fashion, or by 2D parallel lamination where multiple inlets converge into a mixing channel.

Using the principle of distributive mixing, a group of researchers devised a mixer capable of achieving 95% mixing within 15 ms when operated at flow rates between 3-200 μL/min (Bessoth et al., 1999). The device comprised of two inlets, each of which was split into 16 thinner segments using a three-dimensional mesh. At the point of confluence, the thin filaments were superimposed in a manner whereby 32 alternating layers of fluids converged into a long serpentine channel (Figure 3-3). One reason for operating the mixer at slow flow rates was to avoid cross contamination between adjacent filaments prior to the mixing chamber. Because of slow flow rates, mixing was diffusion limited, and the mixer required a long channel to ensure adequate residence times for fluid streams.

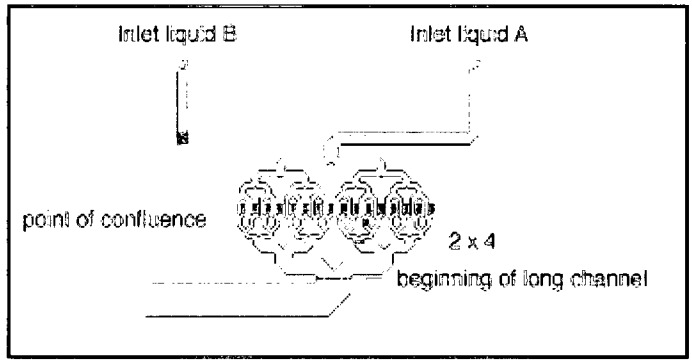

Figure 3-3: A Multi-Lamination mixer merging 32 layers of fluids (Bessoth et al, 1999)

A second group of researchers used a finer mesh to split a stream into a 25-filament comb, with each filament measuring 20 μm in width (Hinsmann et al., 2001a). By overlapping two combs, each supplied with a different solution, a 50-streamline feed comprising of alternating solutions was realized within the main channel of the mixer. Premixing of liquids in the superimposed microchannels was avoided by placing a thin metal sheet between them.

Multi-lamination through distributive mixing is an elegant technique to achieve mixing, but it involves complex fabrication processes to form an interdigital flow pattern. Furthermore, the thin channels within the comb are prone to blockage if the liquid contains particulates. Hence a simpler approach that uses multiple inlets, fed with different reagents, to create a periodic feed arrangement within the mixing channel can be pursued. One such device, shown in Figure 3-4, consists of five inlet streams that converge into a single channel (Jackman et al., 2001).

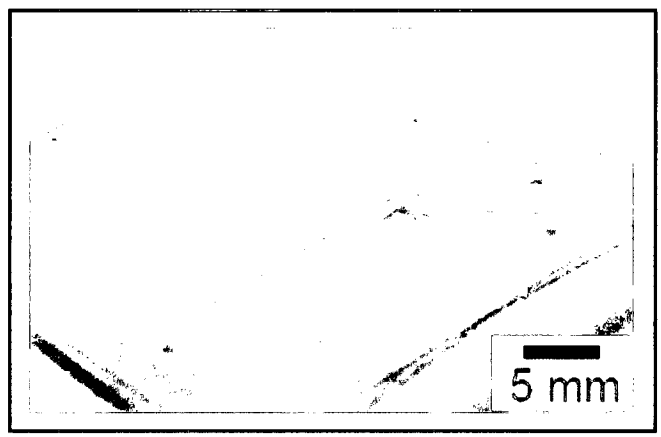

Figure 3-4: Multiple Inlets allow for multi-lamination in two dimensions. (Jackman et al, 2001)

3.3.3 Flow Focussing Mixers

In order to avoid large pressure drops along the mixing channel in multi-lamination mixers, the width of each filament is optimized such that the resulting liquid segment is rather thick (>100 μm) (Hessel et al., 2003). Consequently, diffusive penetration of molecules between streams is limited, and mixing takes a significant time to complete. One approach for improving mixing times involves a reduction in diffusion length between alternating streams. This usually entails geometric focusing that squeezes the width of the channel. In one device, called a SuperFocus mixer, triangular focusing was employed to compress the filaments by a factor of 200, from 800 μm to 4 μm. As a result, a 95% improvement in mixing was recorded within 4 ms after the flow rate was increased to 350 l/h.

Prior to the commercialization of the SuperFocus mixer, researchers investigated the influence of geometrical variations of the focusing region on mixing performance in interdigital mixers (Hardt and Schönfeld, 2003). The study compared slit-shaped, rectangular, and triangular mixing chamber geometries for a range of flow rates (Figure 3-5). Periodical profiles resulting from the interdigital feed arrangement were seen to persist for the entire length of the rectangular chamber even for slowest flow rates. This result was expected since the mixer lacked a focusing region, and mixing was diffusion-limited. Flow patterns in the triangular chamber became less periodic, and a more homogenous mixture was observed at the entrance of the rectangular outlet zone. Meanwhile, flow patterns for the slit-shaped chamber were even more complicated, especially at high flow rates (2 l/h). The outer laminae were seen to curl inwards and form recirculation zones at the entrance of the thin rectangular zone.

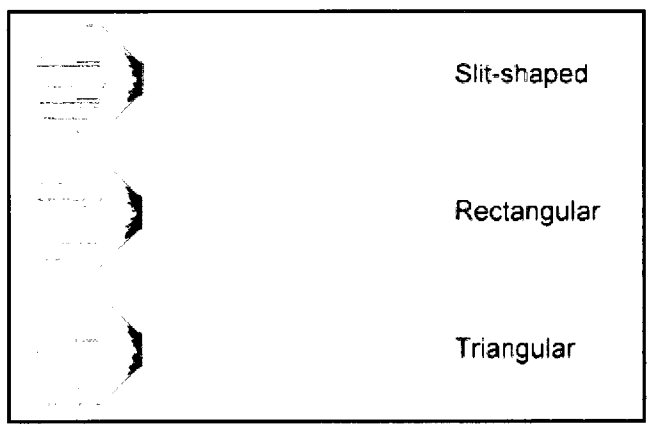

Figure 3-5: Three mixing chamber geometries employing flow focusing (Hardt and Schönfeld, 2003)

Flow focusing can also be accomplished through hydrodynamic focusing whereby a central stream is compressed by sheath flows coming from the sides. Once again, diffusion distances are reduced and molecules from the central stream can penetrate outward much more rapidly. Using this technique, a device capable of diffusive mixing within 10 μs was reported (Knight et al., 1998). The width of the central stream was controlled through adjustment of pressure driving the side flows (Figure 3-6). One drawback of hydrodynamic focusing is that it requires the use of complex fluid pumping systems that can accommodate variable flow rates.

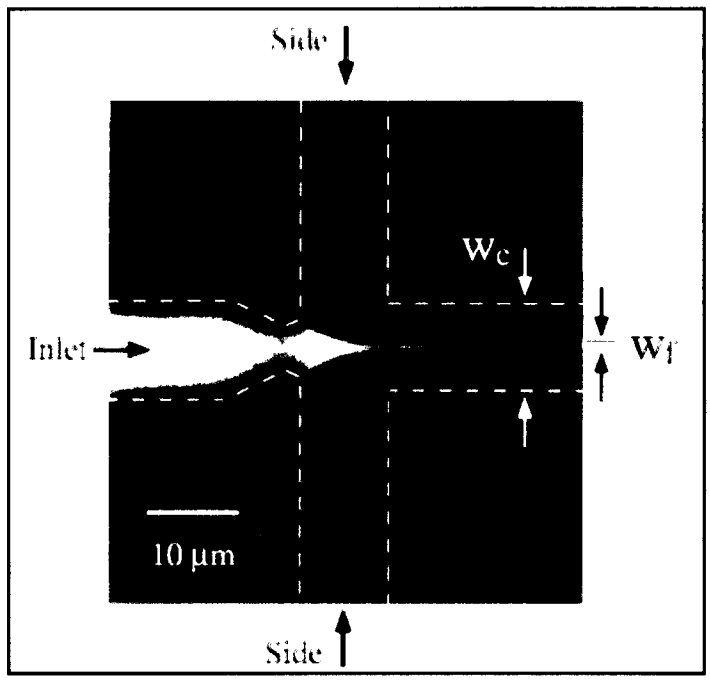

Figure 3-6: Mixing by hydrodynamic focusing. Two sheath flows constrict the central inlet flow, allowing mixing to accelerate as a result (Knight et al., 1998)

3.3.4 Chaotic Flow Mixers

The efficiency of large-scale industrial stirrers in rapidly mixing fluids stems from the generation of turbulent eddies which force fluid elements to stretch and fold in an exponential manner. Unfortunately, with a reduction in mixer dimension, flow enters the laminar regime where inertial forces responsible for generating turbulence are suppressed by viscous forces. As a consequence, special techniques have to be employed which force streamline flow to move chaotically. One such strategy employs chaotic advection to distort bulk flow (Aref, 1990). This phenomenon can be accomplished through the incorporation of obstacles within the mixing channel, by structuring

mixing elements at the surface of the channel, or by creating tortuous flow geometry, that continuously alters the direction of flow.

Numerous devices that incorporate obstacles to break up flow and create lateral mass transport have been reported (Johnson et al., 2002, Wang et al., 2002). Initial studies used computational methods to assess the effects of obstacle shape and placement position on mixing performance. It was found that obstacles placed at an offset from the center in an alternating manner had a positive effect on mixing efficiency. Moreover, roughed up diamond-shaped obstacles yielded 77% mixing compared with 56% for triangular shaped and 44% for diamond-shaped obstacles at 5 mm from junction (Figure 3-7). To verify numerical results, a mixer bearing roughed-up diamond shaped obstacles placed in an asymmetric arrangement was fabricated. Even though the mixer was operated at low flow rates (Re < 10), the obstacles were able to cause a substantial breakup and realignment of flow to improve mixing efficiency.

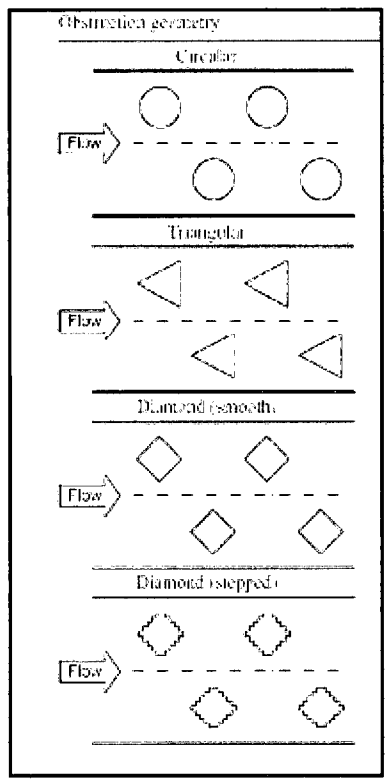

Figure 3-7: Various obstacle shapes designed to disrupt flow patterns and promote mixing (Bhagat et al., 2007)

Mixers with embedded obstacles incur large pressure drops along the channels and are thus susceptible to leakage if operated at high flow rates. At the same time, high flow rates are necessary

to overcome fluidic resistance and induce flow rearrangement that increases mixing. A compromise can be reached if obstacles are replaced by surface structures that promote secondary flows. One group of researchers used laser ablation to create slanted wells within the mixing channel of a T-junction mixer (Johnson et al., 2002). When the device was operated at low flow rates, a fluid segment was observed to break away from bulk flow and follow the contour of the wells. When mixing percentage was measured at a distance of 183 μm from the junction, the 4-well mixer achieved 75% mixing compared to just 32% mixing for a diffusion-limited T-mixer (Figure 3-8).

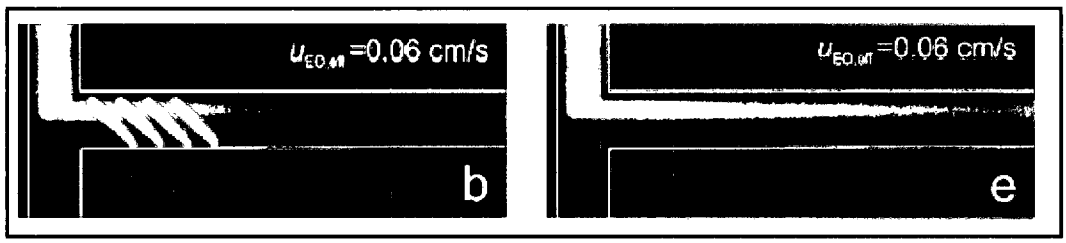

Figure 3-8: Comparison of a 4-well mixer with a T-junction mixer. The wells induce flow rearrangement that increases mixing (Johnson et al., 2002)

Instead of etching wells at the surface of the channel, another group patterned grooves on the floor at an oblique angle (Stroock et al., 2002). These groves offered anisotropic resistance to flow such that the streamline trajectory developed a helical profile along the length of the channel (Figure 3-9). Helical flows stretch and distort concentration profiles to produce a significant improvement in mixing rate. In another design, the same group increased mixing rates by a factor of five by structuring staggered herringbone grooves on the floor of the channel (Stroock et al., 2002). These structures induced a superimposition of different recirculation zones created from flow over ridges as mentioned in their previous paper. Experimental verification was carried out by running a fluorescent and a clear solution through the staggered herringbone mixer, and confocal images of the cross-section showed rapid stirring and thinning of adjacent filaments (Figure 3-10).

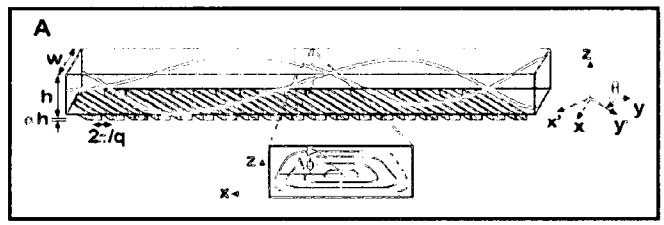

Figure 3-9: Helical flow profile observed in the presence of grooves (Stroock et al., 2002)

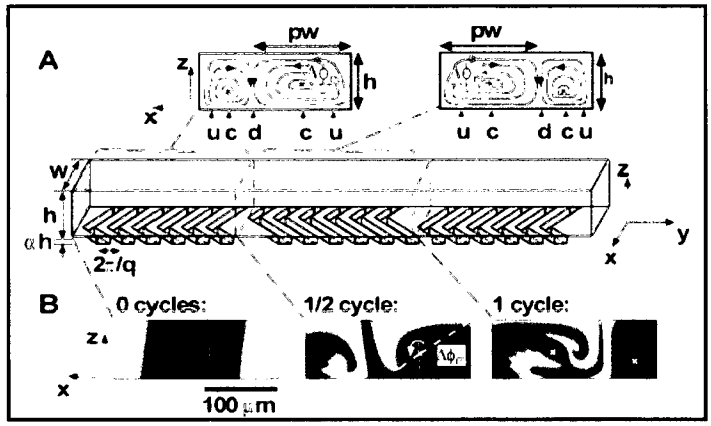

Figure 3-10: Stirring effect in a staggered herringbone mixer (Stroock et al., 2002)

Finally, chaotic advection of fluid can also result from contorting the geometry of the channel, which forces the fluid through a three-dimensional maze. This serves to produce convective currents that stretch and distort flow profile in an effort to increase the effective area available for diffusion. One reported mixer had its mixing channel convoluted into a zigzag shape that not only increased the residence time of adjacent fluid streams at slow flow rates, but also induced flow recirculation around turns at high Reynolds number (Mengeaud et al., 2002). Four geometries of different step-to-width ratios (α) were numerically evaluated in terms of mixing efficiency (Figure 3-11). The results indicate that at high Reynolds number (Re = 267), mixing performance increases proportionally as α is increased to 4, after which it decreases slightly. At either ends of this optimum value, vortices forming at the bends were confined to local regions, thereby causing minimal disruption in bulk flow.

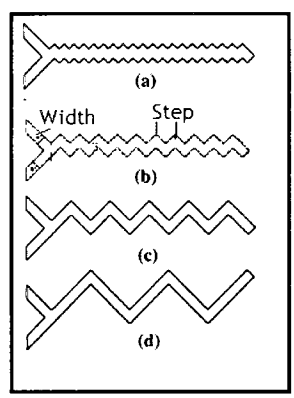

Figure 3-11: Four zigzag geometries that alter the direction of flow resulting, in an improvement in mixing (Mengeaud et al., 2002)

3.4 Fabrication techniques for glass and other crystalline substrates

3.4.1 Bulk Micromachining

Micromachining processes for glass substrates have largely been adopted from silicon processing techniques developed and refined over the years in the integrated circuit industry. However, due to variations in glass composition, these processes have to be optimized for achieving desired results. Bulk micromachining of glass is a mature technique that can define features such as rectangular pits and channels in the substrate through etching (Ronggui and Righini, 1991). The process entails protecting certain regions of the substrate through a patterned masking layer, while leaving unprotected regions vulnerable to attack by etching species.

A thin masking layer of gold or chromium is vapor deposited onto the glass substrate. Then a second deposition process uses spin coating to deposit a thin layer of photoresist over the metal. The resist is then exposed to UV light through a chrome mask bearing the geometry of the channel. The exposed regions of the resist are removed by development, while the newly exposed metal regions are etched away by chemical means. This marks out the desired channel pattern in terms of the exposed glass surface, while the metal layer masks the rest of the substrate. An appropriate etching solution then cuts through the exposed glass surface, leaving a channel in the process.

Fabrication of vertical sidewalls in glass substrates has been particularly difficult due to their poly-crystalline nature. To date, wet etching of glass has only been carried out isotropically by aggressive agents, such as hydrogen fluoride, to produce curved geometries (Chiem and Harrison, 1997). The etch rate is influenced by the concentration of the acid (3.4 μm/min at 40% HF), and therefore presents a drawback if close control of dimensions is needed. One way to alleviate this issue involves addition of ammonium fluoride, which prevents large-scale changes in HF concentration and maintains a constant pH (Jacobson and Ramsey, 1997). Wet etching of crystalline substrates can, however, be carried under mild conditions as demonstrated by one group. Using an aqueous solution of ferrous ammonium sulfate, 10 μm deep isotropic channels were etched in calcium fluoride with the help of a patterned polymer masking layer (Pan et al., 2004).

Due to the precautionary conditions required when dealing with hydrogen fluoride solutions, and the need for fabricating rectangular channels, researchers have looked towards dry etching methods. Reactive ion etching of fused quartz and borosilicate glass has been demonstrated recently (Li et al., 2001, Ujiie et al., 2000). Following deposition and patterning of metal etch masks, the

exposed surfaces is attacked by high-density plasma containing ionized SF6 gas. Using this technique, microchannels with aspect ratios (height:width) greater than 10 have been fabricated.

Another approach for creating rectangular microchannels is based on laser-assisted ablation of glass surfaces. Short-duration pulses from a UV or IR CO_2 laser excite surface molecules and fragments bonds within the silica network. The forceful nature of the process also creates a shock wave that disperses the debris to the surroundings to leave a photoablated cavity. Microchannels as deep as 10 μm and 100 mm long have been fabricated outside a clean room and without the use of corrosive agents in less than 15 minutes. The channel width and depth can be altered by adjusting the laser beam spot size and scanning speed (Cheng et al., 2005). Since the laser is displaced with computer numerical control (CNC) machinery, repeatability and uniformity tend to become limiting issues.

In the absence of clean room facilities and expensive laser systems, traditional CNC milling and powder blasting techniques can be used to create microstructures with minimum feature size exceeding 100 μm. The substrate being cut, however, must be water insoluble to resist water-based coolants used during the process. One group used a 120 μm brass end-mill rotating at 5000 rpm to cut 50 μm deep grooves in zinc selenide windows (Marinkovic et al., 2000).

3.4.2 Spin-On Polymer Techniques

The costs associated with film deposition and plasma etching techniques have prompted researchers to look for a more economical technique for fabricating microchannels. Recent advances in polymer chemistry have led to the advent of photosensitive resists that can be deposited in thick layers on various substrates. Lithographic processing of polymers can create sub-100 micrometer deep channels with vertical sidewalls. The technique has led to microfluidic systems on quartz, borosilicate and calcium fluoride materials compatible with in-situ detection in the UV, visible and infrared regions, respectively (Hinsmann et al., 2001b), Jackman et al., 2001).

Epon-based polymer, SU-8 has become the photoresist of choice for structuring microchannels on various substrates. Upon cross-linking, it develops high mechanical and chemical strength, which makes it resilient to high pressure flows and aggressive chemicals. Despite these advantages, SU-8 films tend to develop cracks and delaminate easily during the fabrication process. This has been attributed to the thermal mismatch between the polymer and the underlying substrate. The problem occurs during the bake procedure when polymer chains shrink upon cross-linking and cause a buildup of stress at the material interface (Conradie and Moore, 2002). Efforts to mitigate these

problems have included the use of adhesion promoters prior to polymer coat, the deposition of a thin metal film with an expansion coefficient similar to that of SU-8, and the optimization of baking times and procedures (Anhoj et al., 2006, Dai et al., 2005, Vettiger et al., 1998).

3.4.3 Bonding

Microchannels etched in glass substrates are often sealed with another glass cover plate to permit access for optical probes and avoid intermediate bonding layers. The three most common techniques for bonding glass-to-glass substrates include thermal bonding, anodic bonding, and adhesion bonding. Thermal bonding is the least complicated of the three in terms of equipment demands. The process begins with the treatment of exposed glass regions to a Piranha solution (a mixture of sulphuric acid and hydrogen peroxide) which hydrates the bonds at the surface. Next, the substrates are dried, aligned, and transferred to a furnace where the temperature is slowly ramped to 600 °C (borosilicate) or 1000 °C (fused quartz). Elevated temperatures facilitate formation of covalent bonds between adjacent silanol groups at the interface (Cheng et al., 2005). For anodic bonding, a thin layer of silicon is sputter-deposited on the surface of the glass cover plate or patterned over the top walls off the microchannels (Ichiki et al., 2003). Adhesion bonding is a versatile technique that can bond two homogeneous or heterogeneous substrates at low temperature. It involves application of a thin layer of adhesive between substrates followed by a polymerization reaction such as UV exposure or thermal cure to solidify the epoxy. Since the epoxy can seep and permanently block the microchannel, the process requires extreme care.

Bonding between polymer-based microchannels has been accomplished by the clever use of structural SU-8 polymer films. Being a negative-tone resist, polymer chains within the irradiated regions of SU-8 get crosslinked while those in unexposed areas remain soft and tacky. In order to utilize unexposed regions for bonding purposes, researchers employed a patterned masking layer to limit exposure within certain regions of SU-8 (Kulka et al., 2004). Following the development of microchannels, the metal layer was removed and uncured regions of polymer were subsequently bonded using a thermal cure.

3.5 Detection Probes for Protein Folding Studies

The investigation of protein folding kinetics not only requires rapid initiation techniques that can trigger the reaction, but they also require detection probes that can monitor structural changes on fast timescales. A review of the literature indicates the predominance of spectroscopic techniques

for monitoring the progress of the folding reactions. Methods include circular dichroism, fluorescence, and infrared and Raman spectroscopies. Since protein folding rates cover different orders of magnitudes, a single detection technique cannot monitor all the changes occurring during the course of folding; instead, different techniques provide structural information that is generally complementary.

3.5.1 Fluorescence

The intrinsic fluorescence of tryptophan (Trp) residues can provide valuable information about the local environment in the vicinity of these amino acids. Variations in the wavelength maximum (λ_{max}) of fluorescent emissions are indicative of changes in the Trp environment usually resulting from large scales changes in the protein structure (Eftink, 1994). Blue shifting of λ_{max} is attributed to screening of Trp residues from aqueous conditions by the protein, whereas red shifting is indicative of solvation of Trp residues upon protein unfolding. With the use of extrinsic fluorophores such as 1-anilino-8-naphthalene sulfonate (ANS), the existence of intermediate states during protein folding can be investigated (Semisotnov et al., 1991). Being hydrophobic, the ANS molecule binds to solvent-accessible, apolar surfaces of the intermediate species. Binding leads to an increase in quantum yield that indicates the presence of hydrophobic clusters that are still exposed to the solvent.

The quantum yield of fluorescence is strongly influenced by changes in temperature, and as such, T-jump initiation techniques are seldom used in conjunction with fluorescence detection. Other factors that determine the quantum yield relate to protein structure transformation (Callender et al., 1998). Quenching of Trp fluorescence can occur due to spatial proximity of Trp residues to other residues such as His, Ala and Glu. This process was observed during the hydrophobic collapse of globular proteins, which reduces the distance between His and Trp residues (Capaldi et al., 2001). External quenchers of Trp such as acrylamide have also been used to monitor solvent accessibility (Kiefhaber et al., 1992). An increase in fluorescent yield in the presence of acrylamide signals the formation of a tightly packed tertiary structure that screens the residue from the quencher.

3.5.2 Infrared Spectroscopy

The first feasibility study employing FTIR detection in the study of protein folding was conducted in 1995 using stopped-flow mixing to induce a pH jump. Individual spectra, acquired in 6.25 seconds, were ratioed against the IR spectrum of the native protein, which allowed a

reconstruction of spectral features of the intermediate states. The signal- to-noise (S/N) ratio of the spectra was improved by carrying out repetitive pH jumps under identical conditions and subsequently co-adding the resulting spectra (White et al., 1995).

With the advent of rapid-scan interferometers, the time resolution for FTIR detection has been further improved to milliseconds. The state of the art rapid scan interferometers can acquire a single spectrum in as little as 25 μs. This has allowed researchers to investigate refolding kinetics of RNase, α-lactalbumin, cytochrome-C, and β-lactoglobulin with millisecond time resolution (Kauffmann et al., 2001, Marinkovic et al., 2000, Reinstadler et al., 1996, Troullier et al., 2000). Most of these experiments were conducted in D_2O buffers due to the fact that the H-O-H bending vibration of water (1645 cm^{-1}) masks the protein amide I band in the infrared spectrum whereas the D-O-D bending vibration occurs at lower wavenumbers (1210 cm^{-1}), thus clearing the amide I spectral window. The use of D_2O has also enabled an increase in the optical path length of the IR cell to 50 μm, which improves the S/N ratio and permits the use of less concentrated protein solutions.

Numerous approaches have been undertaken to increase the time resolution of rapid-scan FTIR spectroscopy. One technique uses a continuous-flow mixing device to initiate a chemical reaction that is monitored by a single point detector at various spots downstream from the mixer (Kauffmann et al., 2001). The knowledge of fluid velocity allows the series of spectra to be temporally resolved; however, due to the large spot size of the IR beam (180 μm), the time resolution of the technique is limited to 400 μs. An effort to reduce the diameter of the IR beam by a focusing lens led to a reduction in optical throughput, which degraded the signal response. Instead, another group of researchers replaced the IR source with a synchrotron radiation source that had a beam spot size of 20 μm. However, in this instance, no data was provided regarding the temporal resolution of the system (Kulka et al., 2004).

A breakthrough in FTIR imaging technology has led to the advent of focal plane array (FPA) detectors. A 32 x 32 FPA can simultaneously acquire 1024 spectra with a spatial resolution of 6 μm to provide an infrared image of a 180 μm^2 sampling area. This spatial resolution is converted into temporal resolution when a continuously flowing solution is imaged, with the temporal resolution achieved being dependant only on the rate of the sample flow and not on the spectral acquisition time. The feasibility of this approach with continuous-flow mixing was the subject of one paper (Kaun et al., 2006); however, the investigation did not deal with protein folding (Figure 3-12).

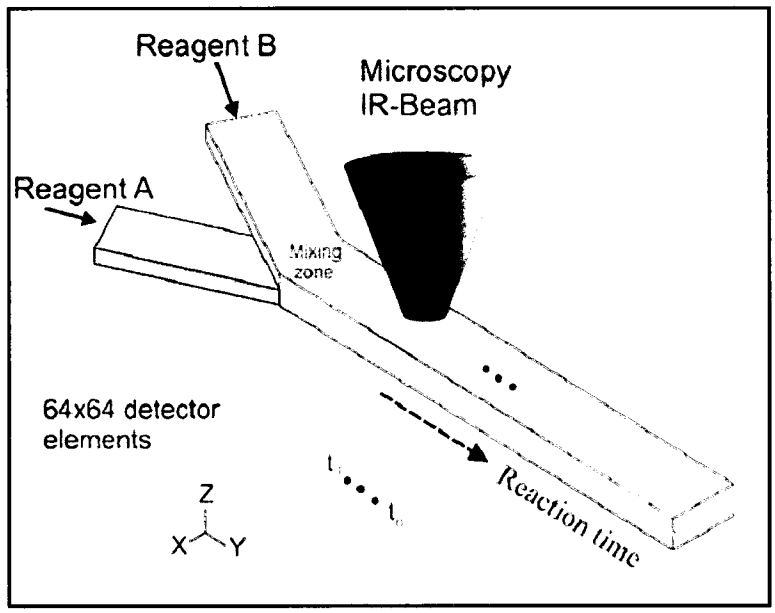

Figure 3-12: Continuous flow mixing with FPA-FTIR detection (Kaun et al., 2006)

3.5.3 Circular Dichroism

The principal CD signal in proteins is located in the far UV region (240 nm and below) of the electromagnetic spectrum. A CD spectrum can yield the relative proportions of secondary structure elements (α-helices, β-sheets, turns, and random coils) present in a protein. Hence time-resolved CD can monitor secondary structure changes resulting from protein folding.

Stopped-flow mixing techniques have been very popular triggers for investigating folding kinetic by CD. A protein, unfolded by Gdn-HCl or urea, is rapidly diluted with a refolding buffer after which the time evolution of conformation changes is recorded by CD. Despite advances in CD instrumentation, the time resolution of the technique has been limited to the millisecond timescale (Forge et al., 2000). As a result, a substantial change in the far-UV CD spectrum associated with protein refolding occurs during instrumental dead time. This rapid change, often characterized as the "burst-phase" intermediate, has been observed for several large globular proteins including RNase, apomyoglobin, and β-lactoglobulin (Houry et al., 1996, Jennings and Wright, 1993, Kuwajima et al., 1987).

3.6 Summary

Rapid mixing of reagents in microfluidic channels offers several advantages in terms of sample consumption, waste reduction, and throughput; therefore, such an approach is ideal for initiating protein folding reactions. Compared with other triggering mechanisms such as T-jump and P-jump, rapid mixing avoids the application of extreme temperatures and electrical currents, both of which have the potential for damaging biological samples. Furthermore, rapid mixing can be used in conjunction with various detection techniques such as infrared, fluorescence, NMR, SAXS, etc.

Due to the small dimensions of the channels, the prevalence of laminar flow conditions reduces the ability of microfluidic devices to mix reagents rapidly. In these devices, mixing is diffusion-limited; therefore, various approaches have been implemented to increase diffusion rates. One approach tries to generate a large concentration gradient by combining two liquids in a narrow channel. Mixing occurs at the material interface by virtue of molecular diffusion. Another approach seeks to even out the concentration gradient in rapid time by flow focusing using hydrodynamic constriction of a central stream by two sheath flows. This not only reduces the diffusion distance for molecules in the central stream, but also provides them with a greater diffusion area. The multi-lamination approach of combining multiple streams in an alternating manner also seeks to create a large surface area between liquid filaments. Finally, using artificial structures to distort the laminar nature of flow, chaotic flow mixers exponentially stretch and fold concentration profiles to create large concentration gradients and increase the diffusion area simultaneously. However, chaotic advection has the tendency to leave unmixed islands of fluid, which can complicate quantitative analysis of mixing.

Fabrication of microfluidic devices has been traditionally carried out in silicon substrates using processing techniques of the semiconductor industry. However, the need for optical and infrared detection of chemical processes has led to the usage of transparent, polycrystalline substrates such as quartz and calcium fluoride. Furthermore, polymer-processing techniques have been developed in recent years that avoid the use of aggressive chemicals common in chemical etching as well as the costly instrumentation required for physical etching. In particular, an Epon-based polymer, SU-8, can realize 100 μm deep channels while offering excellent chemical and mechanical properties. These techniques are addressed in detail in Chapter 4.

4. Fabrication Methods

4.1 Overview

Fabrication of microfluidic devices from spin-on polymer technology is a multi-tier process consisting of numerous stages during which a geometrical pattern on a mask is transferred onto a substrate by means of selective polymer etching. This chapter describes the various stages of device fabrication and reports on the optimization procedures implemented to create a reproducible model. A brief outline of the steps involved in device production is presented initially after which each step is discussed in detail in sections 4.3-4.11.

4.2 Fabrication Process

The process flow consists of the lithographic processing of the EPON based spin-on polymer, SU-8, to create microchannels on calcium fluoride substrates (Figure 4-1). Prior to polymer deposition, the substrate is thoroughly cleaned to facilitate film deposition and adhesion (4-1a). Next, a small volume of resist is dispensed over the substrate surface, which is then rotated at a high speed. This causes the polymer to spread out over the surface as a thin film (4-1b). A soft bake then reduces the solvent content of the film and densifies the polymer (4-1c). Afterwards, the resist is selectively irradiated through a quartz mask that bears the pattern of the microchannel (4-1d). The exposed regions undergo a chemical change that makes them inert to the action of a developer solution. A post exposure bake initiates the cross-linking of polymer within the exposed region (4-1e). The lithographic process concludes with development, whereby a developer solution etches away the unexposed regions of the resist and leaves a microchannel imprint (4-1f).

Using the above approach, a microchannel structured on a single substrate can be subsequently closed by a blank cover slip bearing inlet and outlet holes (4-2a). Conversely, two complementary microchannels can be fabricated on separate substrates that can be paired and bonded later on (4-2b). The former technique is easier to implement, but complications arising from film non-uniformity at higher thicknesses can prevent the cover slip from coming into close contact with the microchannel. Hence, there is a risk of liquid leakage especially under high pressure flows. The latter technique calls for the microchannel thickness to be reduced in half and thus circumvents the uniformity issues encountered with thicker films. However, inlet and outlet holes would need to be drilled carefully in the top substrate to avoid damaging the polymeric microchannel.

Whichever fabrication technique is implemented, the inlet and outlet holes would require alignment with the microchannel prior to bonding. This task is especially complicated for opaque substrates, which require backside alignment marks for precise positioning. After alignment, an intermediate layer composed of various organic compounds can facilitate bonding between two substrates such that a tight seal is formed between microchannels (Figure 4-3). Finally, the microchannel can be interfaced with fluid pumping instruments via miniature tubules glued onto the delivery holes.

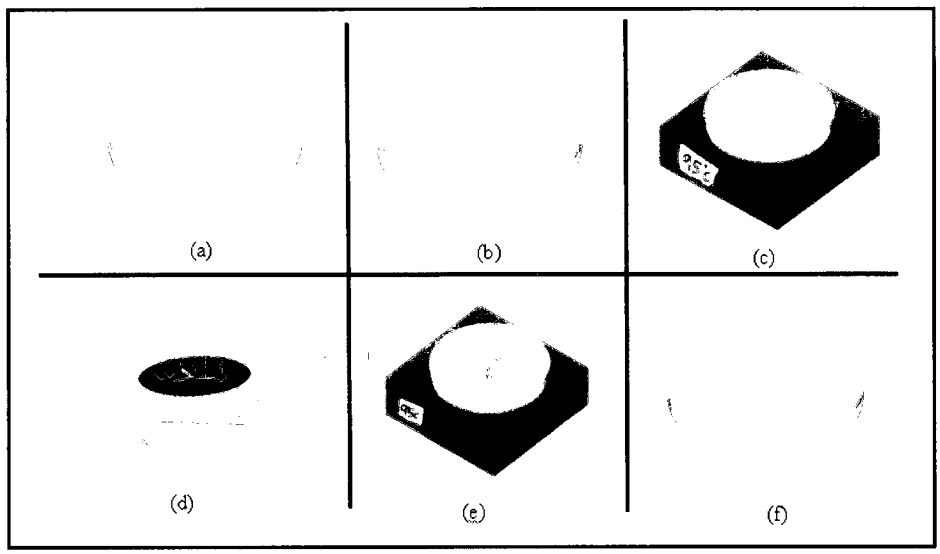

Figure 4-1: Different stages of polymer lithography. (a) Substrate Preparation; (b) Polymer Coating; (c) Soft Baking; (d) UV-exposure; (e) Post Exposure Bake; (f) Development

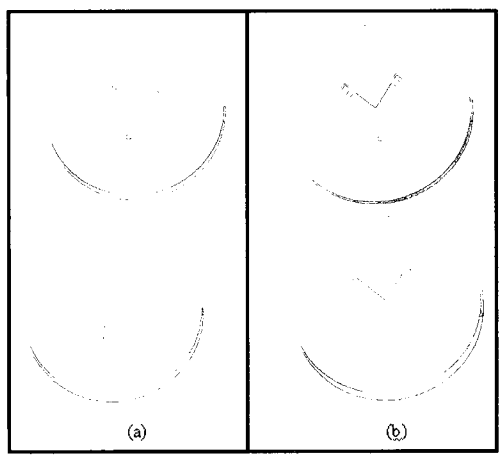

Figure 4-2: Mixer Configurations. (a) Single Channel Mixer; (b) Dual Channel Mixer

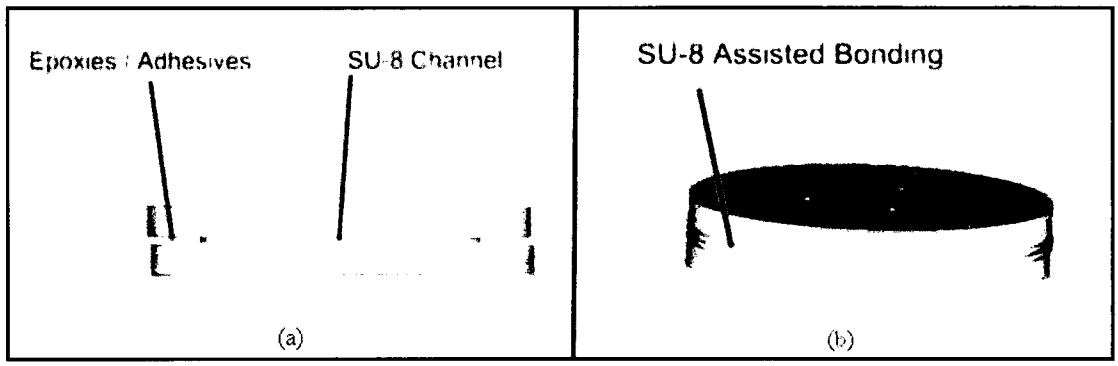

Figure 4-3: Bonding techniques. (a) Adhesive bonding; (b) SU-8-assisted bonding

4.3 Substrate Preparation

For this study, double side polished calcium fluoride (CaF_2) windows measuring 25 mm (diameter) by 2 mm (thickness) were used as base substrates (International Crystal Labs; Crystran Ltd). These windows were selected for their high transmittance in the visible and mid-IR regions, which enabled simultaneous detection of mixing by optical and IR means respectively. Furthermore, these windows can be used without an anti-reflective coating due to the low refractive index of CaF_2. Vendors however polish the substrate surface to lower transmission losses occurring due to light scatter. Polishing also removes surface defects such as minor cracks, scratches, or embedded impurities, and produces a smooth surface that ensures a uniform polymer coat.

Prior to SU-8 deposition, the substrate required a number of cleaning steps to remove fingerprint stains and other organic residues that might degrade film uniformity and its adhesion characteristics. Researchers have previously used a mixture of sulfuric acid and hydrogen peroxide in a 3:1 ratio to clean organic residues off silicon substrates (Li et al., 2003). This mixture, known as Piranha solution, is a strong oxidizer that not only attacks organic matter but also hydroxylates most surfaces making them hydrophilic. As an initial test, a calcium fluoride window was immersed in a Piranha solution for 5 minutes, after which it was rinsed with water. However, during the rinse process, a white layer of calcium oxide formed on the surface of the window. While examining this layer with a profilometer, a thickness variation of ± 5 μm was discovered on the surface. Since such a variation could complicate the polymer coating process, a less aggressive cleaning procedure was implemented in which the substrates were immersed in a 1:1 mixture of acetone and isopropanol (IPA) for 10 minutes, and then rinsed with water.

Due to the hydrophobic nature of SU-8, the presence of water molecules on the substrate surface could promote film delamination during the later processing stages (Larson, 2006). In order to avoid this scenario, the substrates were dehydrated in a convection oven at 120 °C for 2 hours, after which they were gently cooled to room temperature.

4.4 Resist Coating

Since its development in the early 1990's by IBM, SU-8 resist has gained prominence as a structuring material for fabricating high aspect ratio microstructures with ease. It has been available commercially since 1996 from Microchem Corporation, which supplies the polymer in different formulations of varying viscosities to cover a wide range of film thicknesses from 1.5 to 250 μm, in a single coating step (Table 4-1). Depending on the desired film thickness, an appropriate SU-8 variant is selected from the table. As mentioned in section 4.1, the process flow can be optimized to structure a 40 μm deep microchannel on resist deposited on a single CaF_2 substrate. Such a channel can be subsequently bonded to a blank coverslip containing pre-drilled inlet and outlet holes to create a closed network. On the other hand, two 20 μm deep microchannels can be structured on separate substrates that can be aligned and bonded to create a 40 μm deep channel. Both scenarios require a SU-8 formulation that can cover a thickness range from 20-40 μm. Consequently, SU-8 type 25 was selected for all the subsequent lithographic processing steps.

SU-8 type	Viscosity (cSt)	Thickness (μm)	Soft bake min at 65 °C	Soft bake min at 95 °C	Post-exposure 65 °C	Post-exposure 95 °C	Development (min)
SU-8 2	45	1.5–5	1	1–3	1	1	1
SU-8 5	290	5–15	1	3–5	1	1–2	1–3
SU-8 10	1050	10–30	2–3	5–7	1	2–3	2–5
SU-8 25	2500	15–40	3–5	5–15	1	2–4	3–6
SU-8 50	1250	40–100	5–10	15–30	1	4–10	6–10
SU-8 100	51 500	100–250	10–30	30–90	1	10–20	10–20

Table 4-1: SU-8 formulations based on viscosity (© Microchem)

Due to the hydrophobic nature of SU-8, the polymer has difficulty wetting hydrophilic surfaces, such as those of crystalline Si or CaF_2. Resist coverage over the surface suffers as a result, and uniform film coatings are difficult to achieve. Researchers have been able to improve SU-8 wetting by applying a thin layer of commercial primers, such as HMDS or OmniCoat, to the crystalline substrate prior to SU-8 coat. These low molecular weight compounds react with the substrate surface to form a thin organic layer that permits a more homogenous SU-8 coverage (Campo and Greiner, 2007). Accordingly, a thin layer of HMDS was spin coated over the calcium fluoride

windows. While significant improvements were observed in terms of resist coverage, the polymer film debonded from the calcium fluoride substrate upon development. Hence the procedure was abandoned because of adhesion failure, and a second technique was pursued to improve resist coverage.

All resist coating steps were carried out using a Spinball coater with an integrated resist dispensing mechanism. Automated dispensing of resist is a preferred technique since it is carried under pressure to prevent the formation of bubbles within the viscous polymer. Preliminary trials were conducted using automated dispense; however, it was discovered that due to surface tension the resist clustered together to form a bead at the center of the substrate. When spinning commenced, the bead disintegrated in a random manner that resulted in poor resist coverage across the surface of the substrate. To alleviate this problem, manual dispensing of resist was pursued, whereby approximately 1 ml polymer was spread across the surface using a plastic syringe prior to spinning. This not only improved SU-8 coverage but also prevented the polymer film from pulling from the edges during the baking process. Since manual dispensing ran the risk of introducing bubbles into the film, the syringe was kept in an upright position for 1 hour to allow bubbles to accumulate in the posterior portion of the barrel.

Once the resist was dispensed over the surface, the chuck was spun to 500 rpm at an acceleration of 100 rpm/s for 10 seconds. While this initial spin helped in spreading the resist across the surface, a prolonged final spin at higher speeds was necessary for achieving uniform film thickness. According to vendor specification (Figure 4-4), a final spin speed of 1175 rpm was required to achieve a 40 μm thick film with SU-8-25. In order to reach this velocity, the chuck was accelerated at 300 rpm/s, after which the final speed was held for 40 seconds. For accurate thickness measurements, the entire lithographic process including softbake, exposure, post exposure bake and development was implemented during the study. When the structural height of the pattern was measured at the center of the substrate, a significant discrepancy was observed between the measured height and that listed in the vendor specification. Since the vendor's recipe was optimized for 150 mm silicon substrates, this discrepancy could result due to a number of reasons including dimensional differences between substrates, variation in polymer wetting characteristics for silicon and calcium fluoride materials, and differences in operating conditions. Hence it was decided that a specific coating recipe for calcium fluoride substrates would need to be formulated if reproducible coatings were desired.

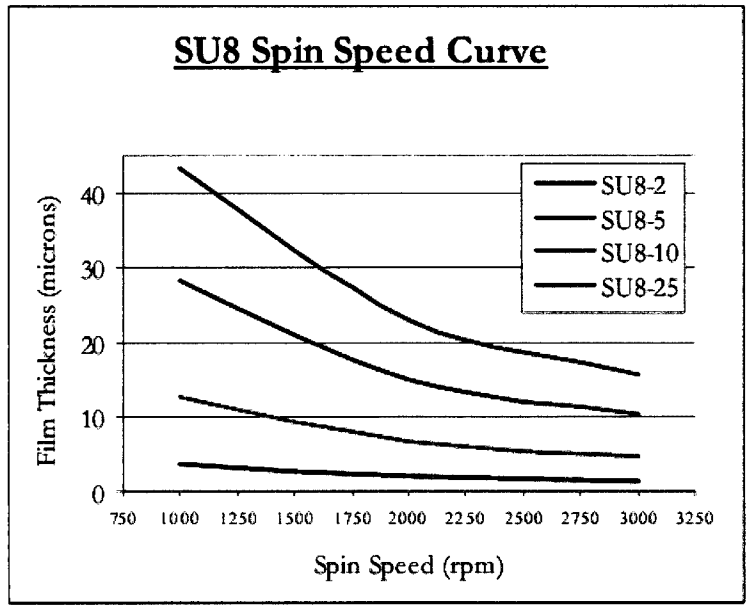

Figure 4-4: The influence of spin speed on achieving various film thicknesses (© Microchem)

4.4.1 Coating Recipe

In order to develop a spin coating recipe, a test mask bearing 13 small squares laid out in a bulls-eye pattern was fabricated (Figure 4-5). The outer diameter of the bulls-eye was restricted to 25 mm so that the entire calcium fluoride window could be utilized for thickness inspection. While examining the heights of the resulting cubic structures, a significant thickness variation was observed between the central and peripheral regions. This was attributed to the accumulation of resist at the edges of the substrate during the coating process (Lin et al., 2002). At the conclusion of the coating process, the edge bead started to recede back towards the center of the substrate thereby degrading film uniformity. For this reason, test points 6-13 were excluded from the thickness measurements and were instead use to quantify film homogeneity in section 4.4.2. Meanwhile, film thickness was measured at test points 1-5 for various spin speeds, and the resulting average thickness was plotted against the manufacturer's curve (Figure 4-6). While the two curves seemingly merge at higher speeds, a noticeable difference in film thickness can be discerned for low spin speeds.

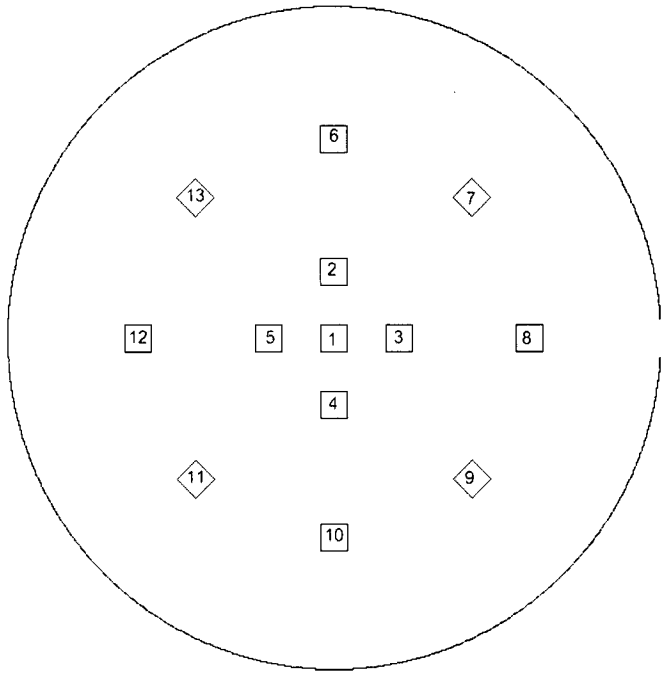

Figure 4-5: Test mask for polymer thickness measurements

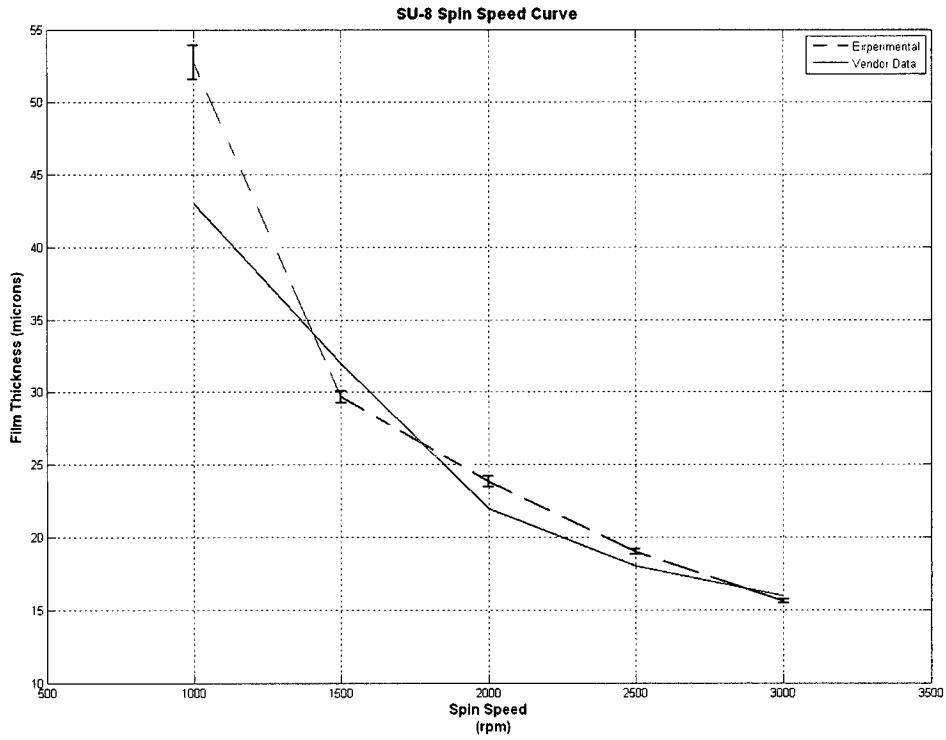

Figure 4-6: Influence of spin speed on polymer thickness. Experimental (Dashed/Blue) vs. Vendor (Solid/Red)

4.4.1.1 *Within-Wafer Deviation*

It is desirable to have a uniform film thickness across the surface of the wafer; however, variations in processing conditions and random errors give rise to deviations from the ideal thickness. For this reason, a methodology for investigating the uniformity of a film at various spin speeds needed to be devised. This methodology should examine within-wafer (WiW) thickness deviations from the norm, as well as wafer-to-wafer (WtW) reproducibility of a developed coating recipe. One approach to measure WiW uniformity relies on normalizing the thickness range of the five test points by their average thickness for a given spin speed (Equation 4-1). The resulting dimensionless number is multiplied by 100 to give percentage deviation from the norm (Smith et al., 1999). A high percentage deviation for within-wafer measurements is indicative of thickness fluctuations.

$$\textbf{Within Wafer} = \frac{(\textbf{Highest Thickness} - \textbf{Lowest Thickness})}{(2 \times \textbf{Average Thickness})} \times 100 \qquad \textbf{Equation 4-1}$$

Uniformity estimates for WiW variation produced by the Range-based statistic are tabulated in Table 4-2. Clearly, film thickness fluctuates to a larger degree at lower spin speed whereas higher speeds yield a more uniform film. At higher spin speeds, the centrifugal force pushes the resist off the edge and thus reduces the thickness of the polymer rim. Consequently, the resulting edge bead does not planerize during the subsequent baking step, and film uniformity within the central portion of the substrate is maintained.

4.4.1.2 *Wafer-to-Wafer Deviation*

Film thickness variation from Wafer-to-Wafer (WtW) can be expected even if the lithographic process is carried out under similar conditions. Numerous aspects that are beyond the control of the user can influence the nature of the process and cause substantial deviation between runs. These aspects include substrate quality, polymer composition, laboratory temperature, instrument calibration drift, and reagent concentration. Hence, it is necessary to quantify run-to-run variation for each spin speed and determine possible changes in recipe development in the event of poor repeatability. To assess WtW repeatability, a range based technique similar to the one mentioned before was used (Equation 4-2). Three wafers were processed at each spin speed, and the deviation of film thickness from the norm was measured. The results, plotted in Figure 4-7, indicate a WtW

variation of less than 2% for all spin speeds. Hence the recipe was deemed to have excellent reproducibility even for low spin speeds that displayed poor within-wafer film uniformity.

$$\textbf{Wafer to Wafer} = \frac{(\textit{Highest Avg Thickness} - \textit{Lowest Avg Thickness})}{(2 \times \textit{Overall Avg Thickness})} \times 100 \qquad \text{Equation 4-2}$$

Spin Speed (rpm)	Wafer	Average Film Thickness (µm)	Within Wafer Uniformity (%)
1000	1	51.4	2.5
	2	53.1	2.5
	3	53.7	2.3
1500	1	29.6	1.5
	2	30.2	1.4
	3	29.3	1.9
2000	1	22.9	1.3
	2	24.3	1.6
	3	24.3	1.2
2500	1	19.2	0.9
	2	19.0	0.9
	3	18.8	1.0
3000	1	15.7	0.8
	2	15.5	0.7
	3	15.6	0.6

Table 4-2: Within-Wafer Uniformity for various spin speeds

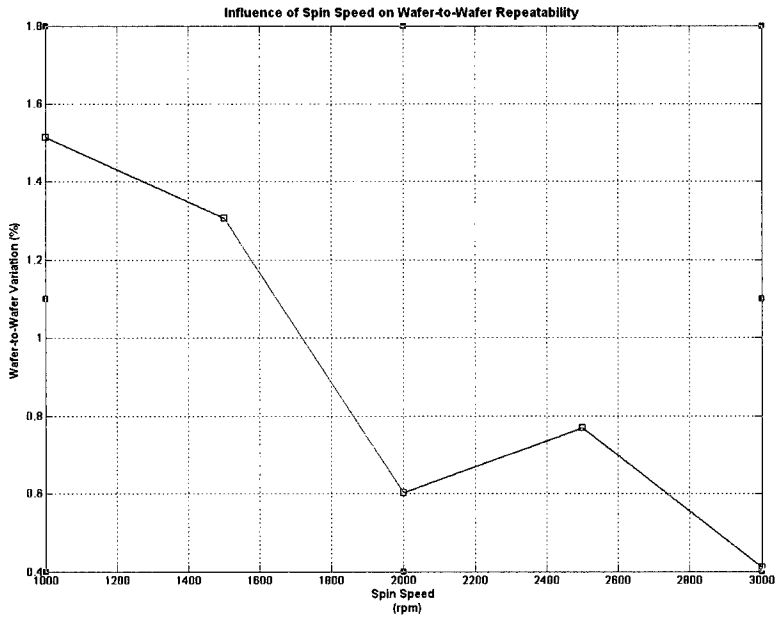

Figure 4-7: Wafer-to-Wafer Repeatability computed at various spin speeds

4.4.2 Edge Bead Investigation

As mentioned before, resist buildup at the edge of the substrate during polymer coating can severally degrade film uniformity. In addition, the edge bead can limit the resolution of the exposure process by preventing an intimate contact to form between the mask and substrate. Similarly, during substrate bonding, it can leave a gap between pairing microchannels, which can allow liquid to seep out during high pressure flow. For this reason, researchers have come up with innovative solutions to get rid of edge beads. One scenario involves directing a fluid jet to the peripheral region of a spinning substrate that forces the edge bead to flow off the surface (Anhoj et al., 2006). Unfortunately, this solution is not practical for smaller substrates. Instead, the edge of the calcium fluoride substrate was mechanically beveled using a file to facilitate polymer removal during the coating process (Figure 4-8). Upon examining film uniformity under low spin speed, no significant reduction in the edge bead was observed in the beveled piece. At this point, it was decided to restrict the channel geometry to the central part of the substrate where a uniform film can be utilized.

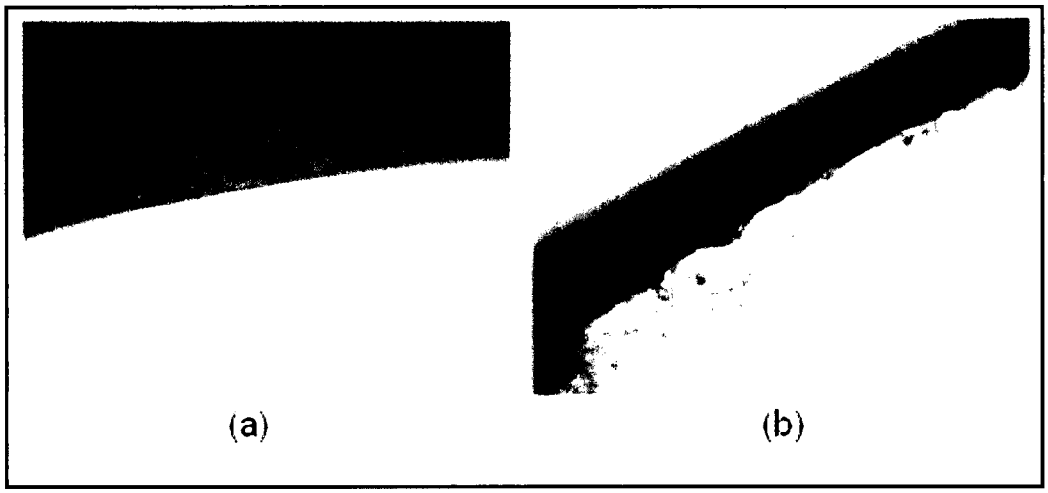

Figure 4-8: Mechanically beveling the calcium fluoride edge to facilitate polymer removal during spin coating. (a) Before Filing; (b) After Filing

Before laying out the design of the microchannel, it was necessary to measure the area on a 25 mm resist-covered calcium fluoride substrate over which the film thickness was uniform. For this purpose, film thickness at test points 6-13 was measured (Figure 4-5), and a surface map showing thickness deviation for a given spin speed was constructed (Figure 4-9). These maps illustrate the severity of the edge bead effect and its reduction in the area available for channel fabrication. Under the worst case scenario, a spin speed of 1000 rpm resulted in an edge bead of 120 μm thickness (128% deviation) and produced a uniform film over 35.8 mm^2 (out of a possible 450 mm^2 area). According to Figure 4-6, a spin speed of 1300 rpm would be required to deposit a 40 μm thick film. At this spin speed, not only would the within-wafer film uniformity suffer, but the microchannel footprint would have to be reduced significantly to utilize the uniform regions of the film. Consequently, a smaller microchannel will require inlet and outlet holes to be drilled in close proximity on a blank calcium fluoride cover plate. Drilling through crystalline materials is a complicated process that causes numerous microcracks to form around the hole. If the holes are close together, these microcracks can propagate in random directions causing extensive structural damage. For these reasons, it was decided to structure microchannels in 20 μm thick resist, deposited by spin coating the polymer at 2400 rpm (Figure 4-6). Such a layer is easier to deposit, has better film uniformity, and allows large geometrical footprints. By aligning two such microchannels against one another, a 40 μm channel can be fabricated.

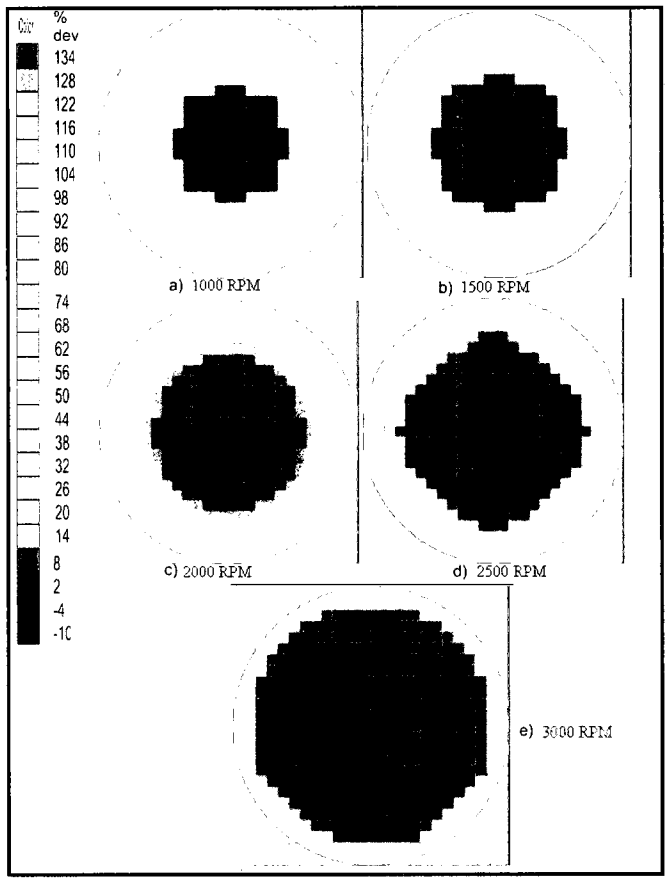

Figure 4-9: Influence of spin speeds on the film uniformity across surface

4.5 Soft Baking

At the completion of the coating process, the resist-covered substrates were placed on a flat surface for 10 minutes. This helped alleviate any intrinsic shear stress within the polymer film and allowed it to reflow and even out any surface non-uniformity. Next, the substrates were soft baked at a temperature of 95 °C. This process is necessary to reduce the solvent content of the film and improve its adhesion with the substrate. Since SU-8 is a thermoplastic polymer, a temperature rise above its glass transition point (55 °C) can cause reflow if the substrate is placed on an uneven surface (Lin et al., 2002). For this reason, all baking steps were carried out on a flat hotplate. Moreover, since calcium fluoride is sensitive to thermal shock, rapid heating was avoided by carrying out the baking process with progressive temperature increments of 1 °C/min from room temperature.

The duration of the softbake is crucial since a short baking interval can leave a wrinkled polymer during the post-exposure heat treatment (Heidermann, 2005). This is due to residual solvent content within the resist that evaporates during PEB to form craters on the surface. An increased solvent content can also promote diffusion of photoinitiator acid between the exposed and unexposed regions during PEB, which can reduce feature resolution of interfacial structures such as sidewalls (Becnel et al., 2005). On the other hand, an extended soft bake interval could evaporate the photoinitiator acid from the film, which would require prolonged resist irradiation to achieve the desired extent of cross-linking (Campo and Greiner, 2007). According to vendor specification, a soft baking duration of 7 minutes was recommended for 20 μm thick films. However, this duration was found to be insufficient for adequate solvent removal as subsequent development caused film debonding from the substrate. While the manufacturer's recipe was developed for silicon wafers that come in sub-millimeter thickness, the calcium fluoride windows used during the experiment were 2 mm thick, and hence required extended baking for the heat to reach the surface. To optimize the soft bake interval, substrates were baked at 95 °C for three different time intervals of 15, 30, and 60 minutes. An increase in bake duration showed a significant improvement in polymer adhesion, and therefore, all subsequent soft bakes were carried out for 60 minutes.

During heat treatment, the polymer and underlying substrate expand according to their thermal expansion coefficients: 55 ppm/K for SU-8 and 18.85 ppm/K for CaF_2 (Heidermann, 2005, (Larionov and Malkin, 1975). A large thermal mismatch causes internal stress to develop at the material interface, which results in film cracking and delamination on silicon substrates (Conradie and Moore, 2002). Typical soft bake procedures, which call for rapid cooling from bake temperatures, are incapable of relieving this stress, and subsequent developmental processes can exacerbate conditions by causing crack formation.

For this study, several temperature reduction schemes were evaluated once the substrates had been baked for 60 minutes. In the first scenario, the substrate was removed from the hotplate and cooled rapidly to room temperature by placing it on a cold surface. This rapid temperature change induced a thermal shock in the calcium fluoride window, causing it to crack instantly. The next experiment required cooling the substrate to the glass transition point of SU-8 at 5 °C/min, after which the substrate was cooled to room temperature rapidly. While the CaF_2 substrate was able to bear this transition, the structural integrity of the polymer film suffered from cracks as shown in

Figure 4-10a. For the last test, the substrate was cooled at a constant rate of 1 °C/min to room temperature. As illustrated in Figure 4-10b, a temperature decrement of 1 °C/min removed the occurrence of cracks and improved film adhesion with the substrate.

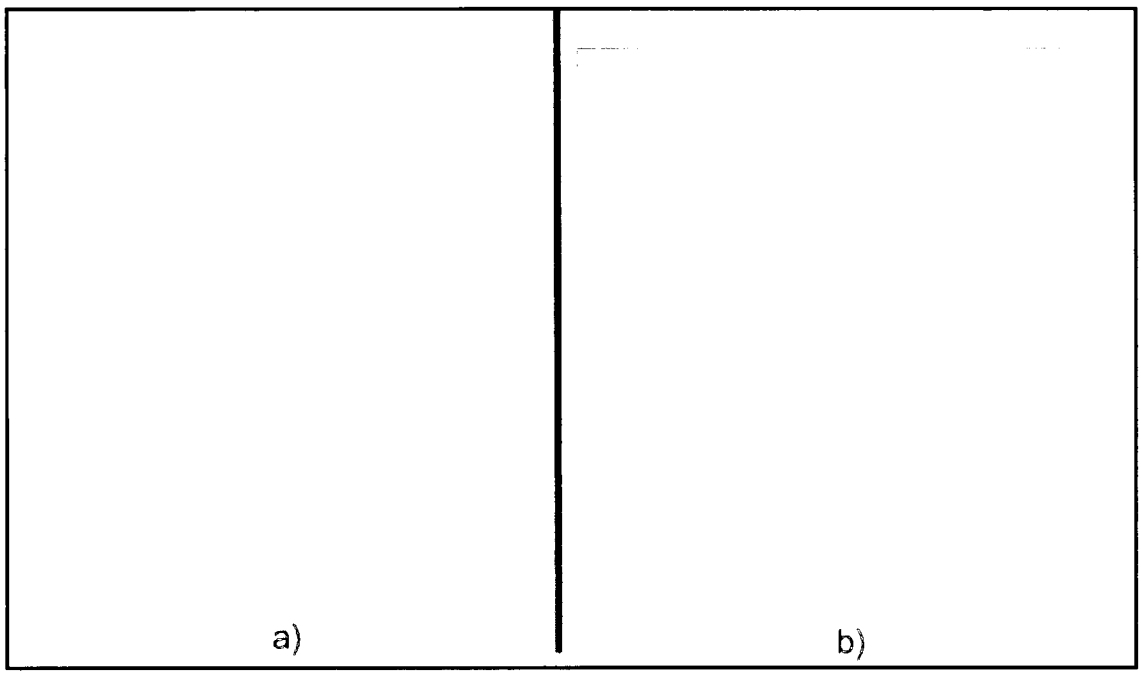

Figure 4-10: Influence of temperature ramping on SU-8 structure. (a) A 5 °C/min temperature decrement caused extensive cracking in the polymer film; (b) No cracking seen in the polymer at 1 °C/min

4.6 Exposure

Besides containing an Epon based epoxy resin, SU-8 is chemically modified by the addition of a photoinitiator that confers photosensitivity to the polymer. When the resist is exposed to UV light below 400 nm wavelength, the photoinitiator decomposes to generate a strong acid that cationically polymerizes the epoxy resin. Application of heat in a subsequent bake initiates polymeric crosslinking in the exposed regions of the resist. The wavelength of irradiation required for activating the photoinitiator needs to be optimized in order to obtain highly resolved structural features. Shorter wavelengths only skim the surface while longer wavelengths penetrate deeper into the resist film. As a result, a broadband UV source will overexpose the surface and underexpose the interior regions of the resist. During the post exposure bake, this promotes the formation of a surface crust consisting of a thin layer of highly cross-linked polymer (Yang et al., 2006). Hence researchers have used optical filters to narrow down the exposure wavelengths and avoid

wavelengths below 350 nm. Accordingly, an Omega optical filter (PL-360LP) which filters wavelengths below 360 nm was used during exposure.

All resist exposures were performed on EVG 620 mask aligner, which guided UV light (350-400 nm), generated by a mercury arc lamp, through the optical filter and mask onto a resist-coated substrate. For irradiating SU-8, the i-line (365 nm) wavelength of the source, with an exposure intensity of 10 mW/cm^2, was selected. Since the intensity of the source degrades over time, the intensity was measured using an optical meter prior to each exposure and optimal adjustments were made to ensure a similar energy dosage was used for each run. The resist manufacturer's data sheet was consulted to obtain the optimal exposure dose for a 20 μm thick film. Since exposure dosage depends on film thickness and the surface finish quality of the underlying substrate, exposure energy between 100-200 mJ/cm^2 was recommended for films on reflective substrates such as silicon. However, for optically transparent substrates such as calcium fluoride, a much higher energy dosage would be required for adequate exposure of 20 μm thick films. Hence an optimization procedure that determined the impact of exposure dose on structural features was implemented.

For dose optimization, test exposures were conducted at various energies on 20 μm thick SU-8 films that were deposited and softbaked under similar circumstances. The results demonstrate that at exposure energies under 200 mJ/cm^2, the resist displayed minor cracks in the exposed regions (Figure 4-11a). This was indicative of under-crosslinking of resist caused by insufficient exposure. As the exposure energy was increased to 400 mJ/cm^2, the cracks disappeared (Figure 4-11b). In order to investigate the impact of higher energy doses, exposures at 800 mJ/cm^2 and 1600 mJ/cm^2 were examined. As seen from Figures 4-11c & 4-11d, excess exposure had a negative impact on the resolution of interfacial structures and produced rough sidewalls and debris within the channel. This can be attributed to the edge bead effect mentioned earlier. Due to this effect, a gap is left between the mask and substrate during exposure that allows light to diffract and infiltrate regions which were meant to be protected by chrome. Hence the interface between exposed and unexposed regions loses its sharpness and leaves rough sidewalls.

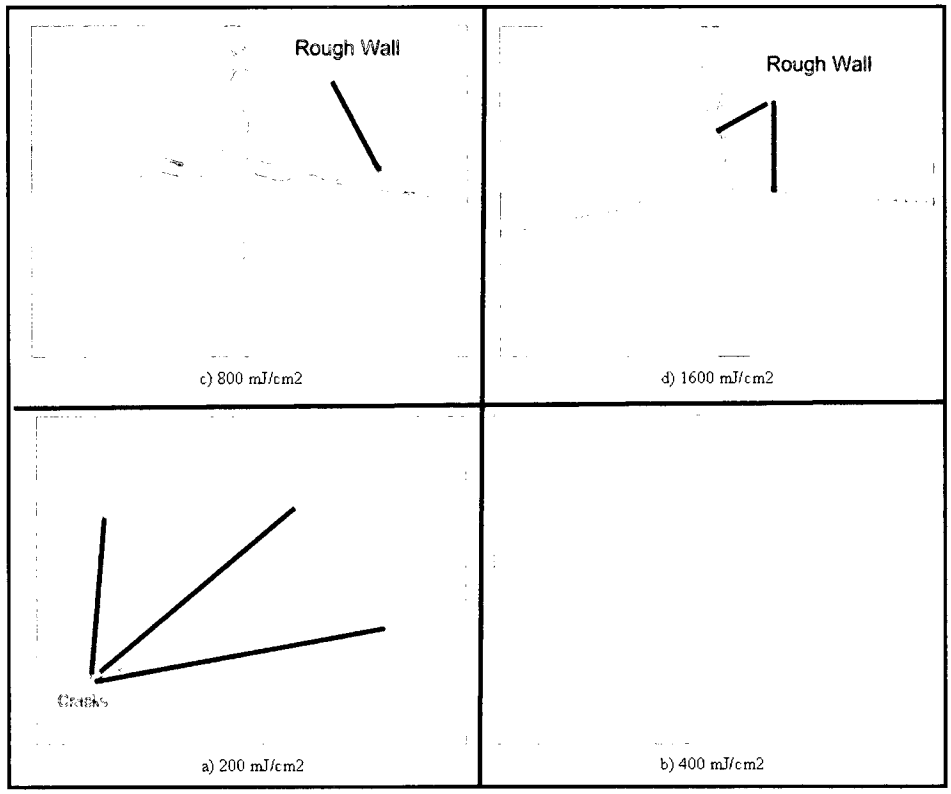

Figure 4-11: The influence of exposure dosage on film composition. (a) Exposure at 200 mJ/cm² show signs of cracking; (b) Exposure at 400 mJ/cm² are crack-free; (c) Exposures at 800 mJ/cm² show rough sidewalls; (d) Exposures at 1600 mJ/cm² exacerbate the condition

4.7 Post-Exposure Bake

A heat treatment following SU-8 exposure is an important lithographic step meant to cross-link the polymer chains in the exposed regions of the resist and make them insoluble to developer solutions. This process is conducted shortly after exposure to avoid photoinitiator diffusion between the exposed and unexposed regions, which can severally degrade feature resolution. It was performed in a manner similar to the earlier softbake procedure where the resist-coated substrate was ramped at 1 °C/min to a bake temperature of 95 °C on a flat hotplate. A slow ramp rate prevents a thermal shock from causing structural damage to the calcium fluoride substrate. The duration of the bake is dependent on exposure dosage; in fact, under exposure requires an extended bake time to initiate crosslinking and ensure optimum cross-link density between the polymer chains (Malic, 2005). For this reason, several films were post baked for various time intervals ranging between 15 to 45 minutes after having been irradiated at an exposure energy of 400 mJ/cm². One

reason for extending the bake duration from the vendor recommended time of 2 minutes was to allow heat to reach the surface of the thick calcium fluoride window. It was discovered that as soon as the temperature of the hotplate exceeded 50 °C, a latent image of the mask formed on the surface of the film. In addition, small wrinkles started to appear in the unexposed regions of the resist with a rise in temperature. The latter scenario could have complicated SU-8 assisted bonding of substrates addressed in Section 4.10. Fortunately, however, baking times exceeding 30 minutes alleviated this problem and the polymer reflowed to form a uniform film.

As mentioned before, any form of heat treatment may cause stress to develop at the material interface due to unmatched expansion of the polymer and substrate. If left untreated, this stress can relieve itself in the form of resist cracking and film delamination during the subsequent developmental stage. During softbaking, these problems can be resolved by temperature ramping cycles that prevent extreme thermal gradients from forming at the interface. However post exposure baking is complicated by the fact that while the substrate expands on heating, the film above shrinks due to polymerization of epoxy resin. Consequently, a buildup of residual stress during the cooling process can contribute to film debonding from the substrate. Hence cooling of substrates at the conclusion of PEB was performed at 0.5 °C/min temperature decrements. Furthermore, the substrates were allowed to relax overnight before development.

4.8 Resist Development

Guiding the lithographic process to its conclusion requires a final developmental procedure where a developer solution selectively etches regions of an irradiated resist to reveal a pattern corresponding to the geometry of the mask. Development of SU-8 resists is carried out by immersing the resist-coated substrate into propylene glycol methyl ether acetate (PGMEA) solution followed by gentle agitation. The time required for development is determined by the geometrical makeup of the patterns being developed, with high aspect ratio features requiring more time. However, prolonged interaction with the developer solution can have negative consequences such as resist swelling and delamination from the cross-linked regions. For this reason, researchers have employed ultra and megasonic agitation procedures to achieve quicker development times (Lin et al., 2002). Accordingly, the beaker containing the substrates and the developer solution was transferred to an ultrasonic bath. However, it was soon discovered that the strong vibrations induced by ultrasonic waves caused structural damage to the sidewalls, causing them to lift off from the surface

(Figure 4-12a). Hence the procedure was shelved in favor of a less aggressive technique that consisted of physically stirring the contents of the developer solution. This enabled development to complete 5 minutes, after which the substrates were removed from solution and rinsed with isopropanol (Figure 4-12b). At times, a milky layer formed within the channel during rinse, which indicated incomplete development. Hence the wafers were returned to a fresh batch of developer solution and stirred for an additional 3 minutes.

Figure 4-12: Influence of ultrasonic agitation on feature development. (a) Ultrasonic agitation unravels the channel structures. (b) Gentle stirring leaves the channel intact

4.9 Drilling

An important step prior to the bonding of microchannels to create a closed fluid network requires drilling inlet and outlet holes for fluid delivery and expulsion. These holes must match the layout of the microchannel to allow an equivalent fluid flow at all inlets. Since a two channel approach was implemented to avoid film uniformity issues, the holes would need to be drilled on a substrate carrying the top microchannel. While this automatically aligns the holes with the microchannel, the drilling procedure must proceed with utmost care to prevent the rotating drill bit from coming into contact with the polymer film. Several parameters such as drill bit material, operating speed, feed rate, drilling depth and coolant performance can play an important role in producing circular holes with straight sidewalls in calcium fluoride substrates.

For preliminary trials, a titanium coated stainless steel bit of 0.5 mm diameter was gently pressed against a test wafer while rotating at 8000 rpm. An oil-based coolant was deposited over the drill bit to provide lubrication to the cutting tool and protect the substrate from heat damage.

Unfortunately, the drill bit completely shattered the crystal as soon as it came into contact with the substrate. Hence diamond coated drill bits, which grind through the substrate instead of cutting it, were used at an operating speed of 8000 rpm, and lubricated with a special water-based coolant. The center of the inlet contour formed the insertion point for the drill bit where a bead of lubricant was applied prior to drilling. During operation, the drill was moved up and down to allow the lubricant to flush out the debris and cool the bit. Once the hole was completed, its surrounding area was inspected for chips and cracks under a microscope. Despite efforts to keep the hole in the center of the inlet rim, the drill bit veered into the microchannel sidewalls, causing minor structural erosion (Figure 4-13). Fortunately, this did not cause the film to debond from the substrate, and the piece was be utilized for device production.

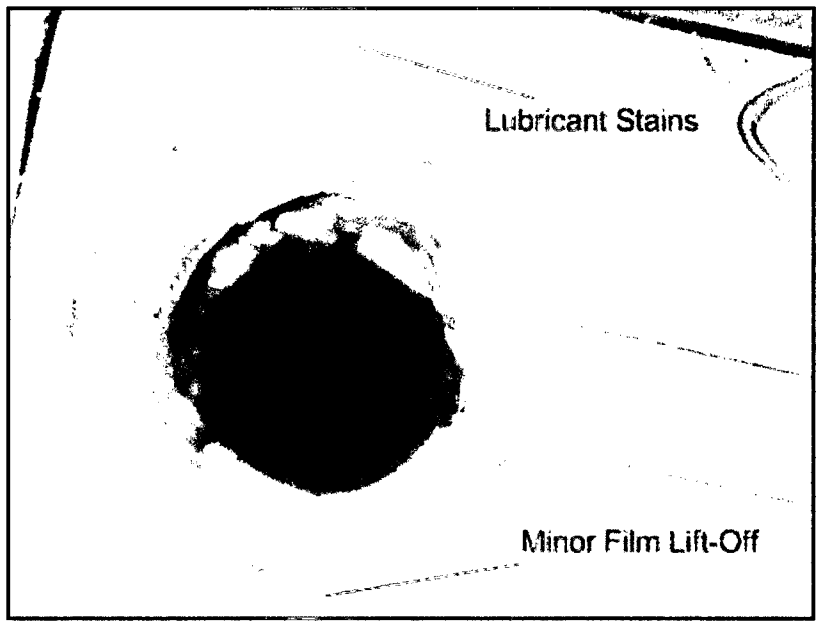

Figure 4-13: Polymer liftoff on drilling

4.10 Substrate Bonding

Successful bonding between substrates requires a clean surface devoid of any gaps, debris, particulates, and roughness. In addition, the surface must be completely dry to prevent water molecules from interacting with the adhesive and degrade bond quality. For this reason, the drilled substrate was rinsed in PGMEA to wash away the lubricant stains and dislodge any debris present within the holes. It was then dehydrated on a flat hot plate at 90 °C for 1 hour. A bonding technique utilizing an intermediate layer was pursued for bonding two calcium fluoride substrates. In the first

two attempts, commercial adhesives were used as an intermediate layer, while the last method utilized unexposed regions of SU-8 film to achieve bonding.

Various organic compounds have been used as intermediate layers to achieve successful bonding as reported in literature. The list of compounds includes PMMA, PDMS, thermal and UV curing adhesive, cyanoacrylates, photoresists, etc. For the first trial, a dab of a commercially available cyanoacrylate adhesive (Instant Krazy Glue ®) was deposited in the gap between two substrates, which were then pressed against one another to facilitate a tight seal formation. This brand of adhesive was selected for its ability to set quickly and form a water resistant bond in a matter of minutes. However, cyanoacrylate molecules have a viscosity similar to that of water and tend to flow easily under applied force prior to polymerization. It was discovered that once the calcium fluoride substrates were pressed together, the glue seeped into the microchannel causing it to block permanently (Figure 4-14).

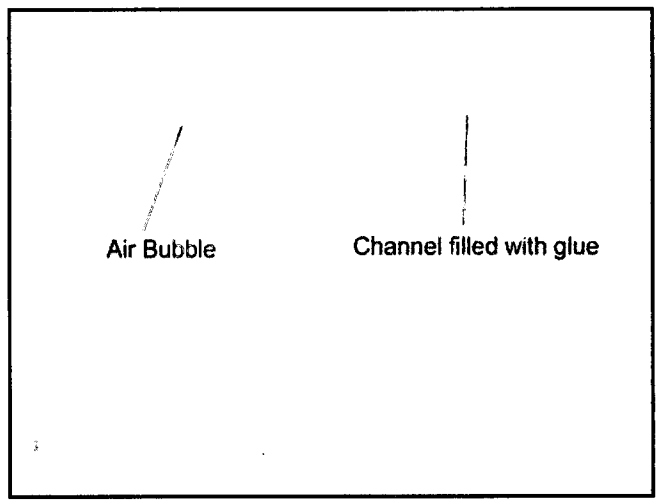

Figure 4-14: Channel blockage by seeping flow of low-viscosity epoxy

Hence for the next trial, a more viscous adhesive (Loctite 349 ®) that set under the influence of UV radiation was used. Once again, a bead of glue was applied within the substrate gap; however, this time a special bonder was used to press the substrates against one another. The wafer stack was placed within a clamp and a compressive force of 100 N was applied to expel excess glue through the sides and reduce the epoxy thickness to the height of the microchannel (40 μm). The force was maintained for 10 minutes, after which the wafer stack was transferred to EVG 620 mask aligner where it was irradiated for 1 minute. Since the epoxy thickness was reduced to micrometers, a complete cure was achieved during the exposure interval. Immediately after bonding, the quality of

the bond was inspected under a microscope. As seen in Figure 4-15a, a high quality bond interface was achieved between the superimposed microchannels. A faint air gap is visible next to the sidewalls along the microchannel. In order to examine bond strength, a crude method that required the flow of high-pressure nitrogen gas through the microchannel was employed. The flow of gas caused the air gap along the sidewalls to propagate outwards, which resulted in the formation of Newton rings (Figure 4-15b). Since fluid flow during a mixing experiment would exert a much greater force than air at the bonding interface, the technique was abandoned in favor of SU-8 assisted bonding.

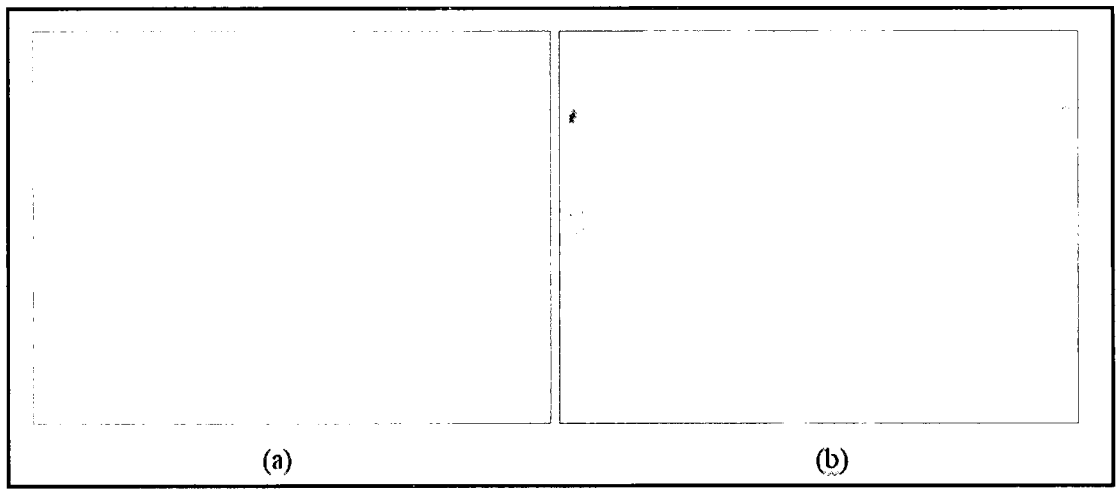

Figure 4-15: Bonding with UV-cure adhesive. (a) A high-quality bond between microchannels; (b) Bond starts to unravel on application of air pressure

Researchers have used SU-8 as an intermediate layer to bond various substrates; however, in most studies either a thin layer of SU-8, spin coated over the entire surface of the wafer, or an exposed region of the resist was used for bonding (Chuang et al., 2003). The former technique is not applicable in this study since the microchannel will have infrared losses emanating from SU-8 absorbance. Meanwhile exposed regions of SU-8 lose their thermoplasticity once they are irradiated. Thus, a bond between exposed SU-8 structures will be of low quality. For this purpose, a technique based on paper published in 2001 was implemented (Hinsmann et al., 2001a). In the original experiment, researchers deposited and patterned a thin layer of metal over unexposed regions of SU-8. This metal layer acted as a masking material to protect unexposed regions of the resist from the developer solution. After development, the masking layer was removed, and the unexposed regions were used as the bonding material. For the present study, however, a less complicated procedure was

followed. A tacky laminate-film resembling scotch tape was attached to polymer regions meant to be protected by the developer solution. In order to avoid the edge bead, only the interior portions of the resist were masked by the tape. After development, the tacky film was removed with ease leaving behind a clear polymer film without any residue (Figure 4-16).

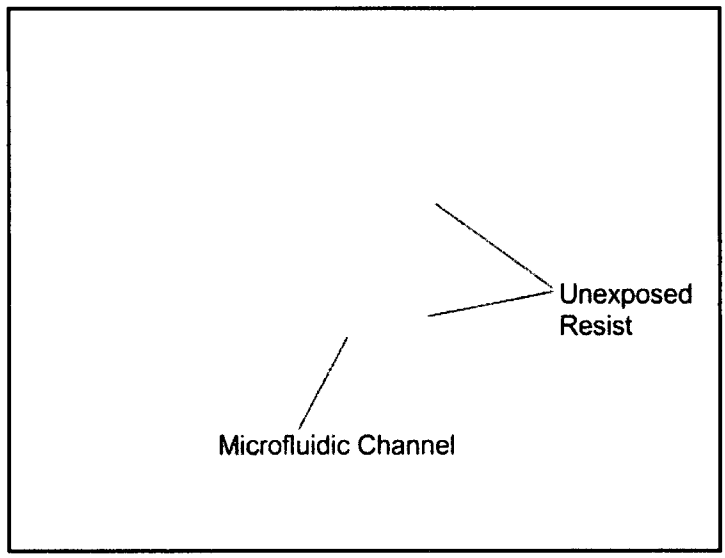

Figure 4-16: Use of a masking tape to protect unexposed region of SU-8 from developer solution

For bonding purposes, the microchannels were aligned manually and placed in EVG 501 wafer bonder. The temperature inside the machine chamber was gently elevated to 100 °C while the wafers were pressed together with a bonding force of 100 N. Temperatures above the glass transition point of unexposed SU-8 caused the polymer film to reflow and fill the gaps between the substrates. Meanwhile the compressive force ensured a close proximity between microchannels. The dark regions in Figure 4-17 attest to the gap filling ability of unexposed SU-8. The resulting bond was water tight as demonstrated by Figure 4-18 where a blue tracer was diluted with a colorless liquid without any fluid leakage from the microchannel.

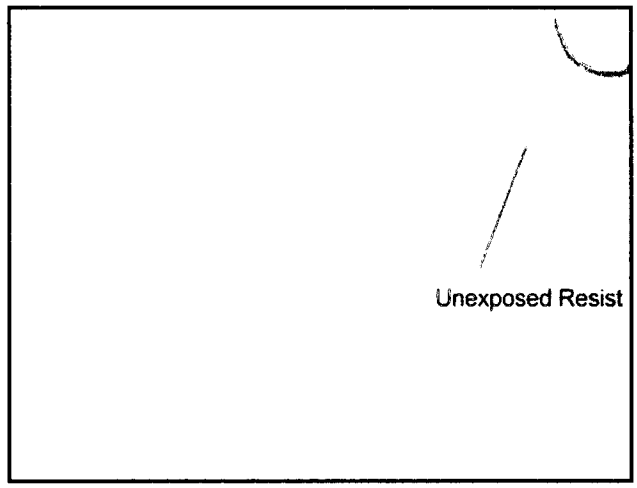

Figure 4-17: S U-8 assisted fusion bonding shows the void filling capacity of unexposed SU-8

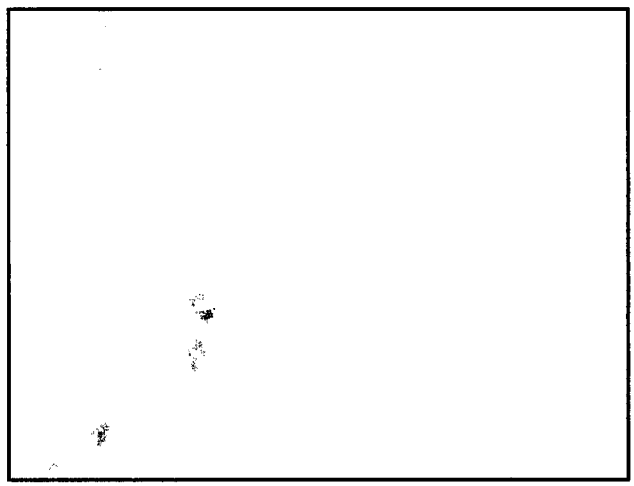

Figure 4-18: Leak-free flow through microchannel indicates high quality bond

4.11 Interfacing

The coupling of microchannels to macroscale instruments, such as a syringe pump, through miniature tubules must be capable of withstanding the tremendous backpressure encountered during high-speed flow. Furthermore, it must be reliable enough to prevent leakage of solvents and avoid introducing particulates into the mixer. Finally, it needs to ensure a dead-volume free connection that would otherwise result in the wastage of sample. Satisfying these requirements is a complicated task, and several studies have come up with innovative solutions, such as on-chip interconnects, to achieve a virtually dead-free connection (Westwood et al., 2008). However, most interfacing

methodologies fall into two categories: (1) Using adapters to secure tubing into the delivery holes, and (2) using adhesives to irreversibly bond tubing with the holes.

Nanoport adapters from Upchurch Scientific have gained prominence within the microfluidics community for their ability to easily interface polymer tubing with small assemblies. However due to their large footprint, these adapters occupy a large space around delivery holes. As a result, these adapters are incompatible with small sized calcium fluoride substrates used in this study. Hence a second approach employing direct bonding of tubules to delivery holes was pursued.

Initially PEEK tubing was inserted into each hole, followed by the placement of a rubber o-ring to form a gasket seal. Thereafter, quick setting epoxy (Instant Krazy Glue ®) was deposited within the crevices of the gasket to form a leak-free bond. However, due to its low viscosity, the glue crept into the microchannel and blocked it permanently. At the same time, the low surface energy of PEEK resulted in the formation of a low quality bond. Hence stainless steel tubing whose surface had been roughened to facilitate bond formation was used in combination with a more viscous adhesive (Devcon 5-Minute ® Epoxy). While this proved to be an excellent coupler in terms of bond strength, the inflexible nature of the material made it extremely difficult to interface long metal tubules with a syringe pump. In order to resolve this issue, syringe needles equipped with a LUER adapter were bonded directly to the mixer as shown in Figure 4-19. These adapters allowed easy interfacing with PEEK tubing that could be easily hooked to gastight syringes. Finally, the mixer was secured in a stainless steel enclosure to facilitate handling during analysis (Figure 4-20).

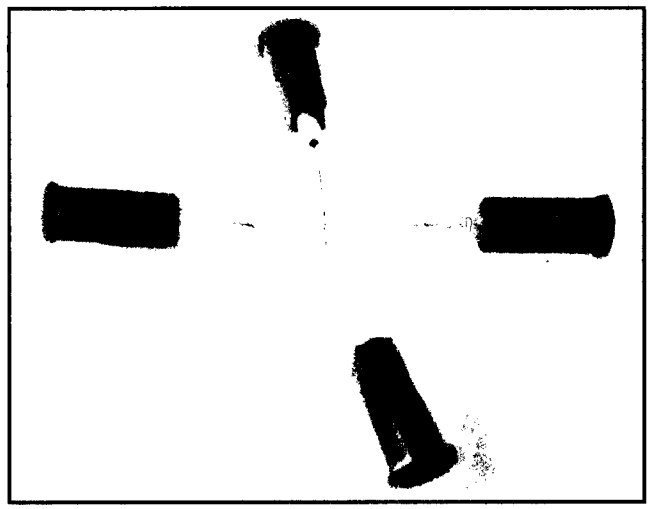

Figure 4-19: Direct bonding of syringe needles with LUER adapters to the microfluidic channel

Figure 4-20: Securing the mixer within a steel casing and interfacing the LUER adapters with PEEK tubing

5. Mixing Performance: Numerical and Experimental Results

5.1 Overview

Fabrication techniques discussed in chapter 4 were implemented to create three different micromixing devices. This chapter describes the numerical and experimental approaches undertaken to assess the mixing performance for each mixer. Briefly, a commercial CFD solver was used to simulate flow inside a T-junction mixer, and based on numerical results an optimum channel aspect ratio and flow rate range was defined over which mixing efficiency was maximum. Thereafter, a mixing experiment between a blue dye and a colorless solution was conducted to validate the results of the simulation. The procedure was repeated for a flow-focusing and a multi-lamination mixer in sections 5.5 and 5.6 respectively. A summary outlining the best-case scenarios for each mixing device under varying flow rates in presented at the end of the chapter.

5.2 Numerical Simulation

5.2.1 Rationale

The impact of various geometric configurations on mixing efficiency can be gauged through computational fluid dynamic (CFD) simulations prior to experimental prototyping. Using this approach, an actual microchannel can be represented by a computational model, which is subjected to various flow parameters and geometric variations, and accurate predictions concerning fluid dynamics and related phenomenon such as convective mixing are obtained. Hence fabrication costs can be reduced significantly as only those mixers that performed well in the simulations would need to be prototyped.

The success of any CFD simulation hinges primarily on two factors: mesh quality and discretizing methods. A simulation begins with a preprocessing stage in which the flow domain is split into a mesh comprising of smaller sub-domains called elements. The shape and density of the mesh elements determine the subsequent choice of numerical discretizing schemes. Uniformly structured meshes characterized by 3D cubic elements can improve the accuracy of numerical simulations; however, they are difficult to generate and require complex grid-generation algorithms. In contrast, unstructured meshes consist of irregularly shaped hexahedral elements generated from an algorithm based on Delaunay triangulation. This algorithm can mesh complex geometries in little

time; however, numerical discretizing schemes require more computer resources to achieve convergence on unstructured grids.

Once the flow domain is partitioned, a discretizing algorithm replaces the Navier-Stokes equations describing flow within each element with an equivalent system of algebraic relations. An incorrect representation of the original partial differential equations could jeopardize the outcome of the computational model; hence, the choice between different discretizing methods becomes crucial. Finite different method can only discretize structured mesh elements, and therefore cannot be used with complex geometries. In contrast, finite volume method is a much more versatile technique that can handle both structured and unstructured grids. It is based on the conservation principle and attempts to balance incoming and outgoing fluxes over the surface of each element.

5.2.2 Methodology

For the present study, a commercial CFD solver (Fluent ®) that employs a finite volume discretizing method was used to simulate flow inside various channel geometries. Prior to numerical investigation, the flow domain was split into a mesh using a mesh-generation software (Gmsh ®). Since the tool could only generate unstructured meshes, the density of hexahedral elements was increased to obtain a more accurate numerical simulation. This placed an increased demand on computer resources with a typical simulation completing in 5 hours on a dual core Pentium 4 machine with 2 gigabytes of memory.

At the start of the simulation, two fluids (A & B), possessing the properties of water at 25 °C, were defined to enter the inlets of the mixer. The flow field within the mixer was considered to be laminar, and standard non-slip boundary conditions were imposed on the walls. A tracer substance ($D = 6.0\text{x}10^{-10}$ m^2/s) added to Fluid A permeated into Fluid B as a result of mixing between the two fluids during the simulation. Once a steady flow profile had developed, a numerical estimate of the degree of mixing was obtained by the monitoring the mass fraction distribution of the tracer substance in the mixing channel.

Figure 5-1 illustrates the mass distribution of tracer in a mixing experiment between fluids A and B in a simple T-mixer. Due to lack of mixing, the tracer is confined to fluid A (mass fraction = 1.0) coming from the left inlet. However, complete mixing is established in a thin region at the interface as indicated by the mass fraction of 0.5. In order to gain a quantitative measure of mixing performance, the mass fraction distribution (c) is extracted from a plane spanning the entire width of the channel (w), located at a distance from the junction (graph in Figure 5-1), and plugged into

Equation 5-1 (Jeon et al., 2000). The initial mass fraction prior to mixing and the final mass fraction at complete mixing are denoted by c_0 and c_∞ respectively.

$$m_{eff} = \left[1 - \frac{\int_0^w |c - c_\infty|}{\int_0^w |c_0 - c_\infty|}\right] \times 100 \qquad \text{Equation 5-1}$$

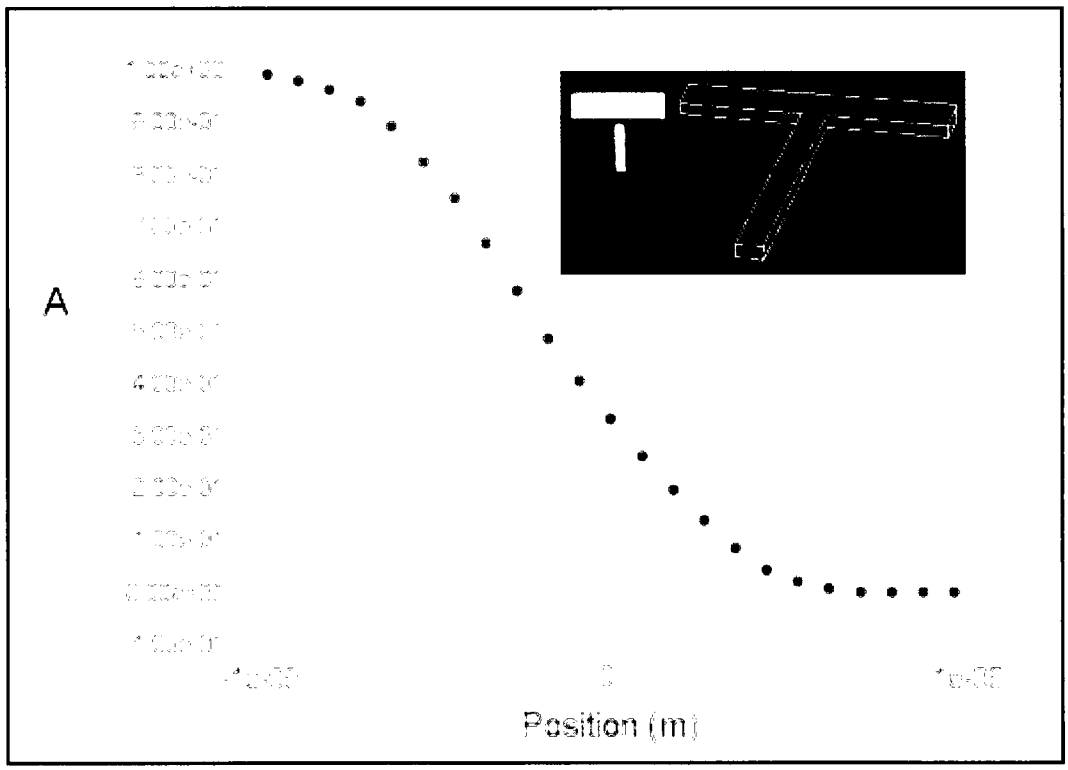

Figure 5-1: Tracer distribution along the width of the channel. Inset shows the progression of red (mass fraction = 1) to blue (mass fraction = 0)

5.3 Experimental Methods

Despite the benefits of simulation models in predicting mixing phenomenon within microchannels, problems stemming from solver convergence and mesh artifacts can compromise the validity of the numerical model. Hence it is necessary to verify the results of numerical simulations with experiments carried using under flow parameters. These experiments also require a detection technique that can faithfully capture the extent of mixing and report the results in a way that allows comparison with those obtained from the simulation. For the present study, two

detection methods, optical and infrared, were employed to monitor the permeation of a blue color dye into a colorless solution due to mixing.

5.3.1 Optical Detection

The extent of mixing was monitored optically by observing the variation in color intensity of a commercially available blue color dye (Sigma-Aldrich ®). After being diluted to 50% by volume in water, the dye was introduced from one inlet of the mixer, while a colorless potassium thiocyanate solution was introduced from the second inlet. As a precaution, these liquids were pre-filtered through a 2 μm pore size filter to remove particulates from entering the mixer. Furthermore, gas tight syringes (Hamilton Ltd ®) were used to dispense the liquids into the mixer to avoid the introduction of bubbles during high-pressure flow. In order to achieve a uniform dispense rate, the syringes were mounted on an electronic syringe pump (New Era Ltd ®) that was programmed to dispense at a constant flow rate.

Mixing performance at each flow rate was quantified by mapping the variation in blue color intensity across the length of the outlet channel. Colored images of the mixing process were captured through a microscope at 40X magnification with a CCD camera. These images were read into Matlab® where the blue channel data was normalized and converted into a matrix of concentration values by using a calibration technique discussed in section 5.3.1.1. Since each row within this matrix represented the distribution of blue color across the width of the channel, a row corresponding to a predefined distance from the T-junction was selected to quantify the mixing performance. Once again, Equation 5-1 was used to obtain a numerical value of mixing efficiency. However, in this instance, c corresponded to dye concentration at a point across the width (n) of the channel, c_∞ to the concentration at complete mixing, and c_0 to the initial dye concentration prior to mixing.

5.3.1.1 Calibration

A calibration experiment was conducted to determine the α and β constants in the Beer-Lambert law (Equation 5-2), which was subsequently used to correlate light absorbance with dye concentration in the experimental run. The optical calibration process involved filling the microchannel with solutions of known dye concentration and capturing color images from a CCD camera (Figure 5-2). The resulting images were broken down into their respective red, green and blue pixel values in Matlab®. Since a blue color dye was used as a tracer to follow the progress of

mixing, only the blue pixel value was used as an index for quantification. In order to limit background interference, each blue pixel value was normalized by dividing it by the sum of red, blue, and green values. These normalized values were plotted against their respective concentration values, and linear regression was performed to obtain a linear relationship.

$$Y(concentration) = \beta X(absorbance) + \alpha \qquad \text{Equation 5-2}$$

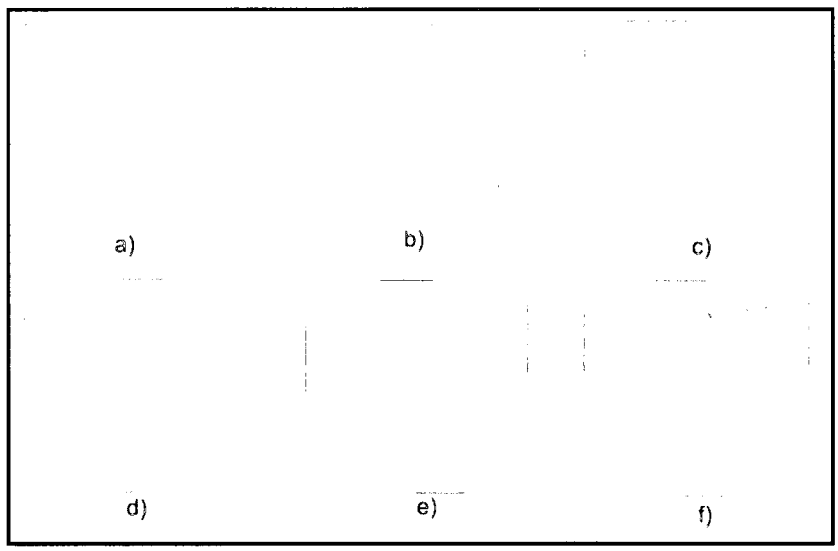

Figure 5-2: CCD images of dye solutions employed for formulating a calibration equation based on Beer-Lambert law. Dye concentration (by volume): (a) 1% (b) 5%, (c) 10%, (d) 20%, (e) 30%, (f) 40%

5.3.2 Infrared Detection

The extent of mixing was monitored using FTIR spectroscopy by observing the variation in band intensity of a 4% potassium thiocyanate (KSCN) solution. Infrared detection was accomplished by means of a focal plane array (FPA) detector that consisted of 1024 tiny elements laid out in a 32x32 square grid. An infrared light beam originating from a Duraglow® mid IR source passed through the outlet channel, and the infrared spectrum of the sample within the channel was recorded by each element of the FPA detector at a spatial resolution of ~ 6 μm.

Since potassium thiocyanate (KSCN) solution was injected through the second inlet of the mixer, certain peaks from its infrared spectrum could be used as markers to assess mixing performance. For this purpose, the area under the peak at 2065 cm^{-1}, originating from the stretching vibration of the C≡N band, was used to obtain a quantitative estimate of chemical distribution

within the FPA's field of view (180 μm^2). Furthermore, this area was related to solution concentration by means of a calibration approach discussed in section 5.3.2.1.

5.3.2.1 Calibration

In order to perform the FTIR calibration, known concentrations of KSCN solutions were flown through the microchannel. Thereafter, for each sample, the 1024 spectra acquired by the FPA detector were averaged, and the area under the 2065 cm^{-1} peak was integrated between 2200 and 2000 cm^{-1} (Figure 5-3). The resulting values were plotted against the corresponding solution concentrations, after which linear regression was performed to obtain the calibration equation

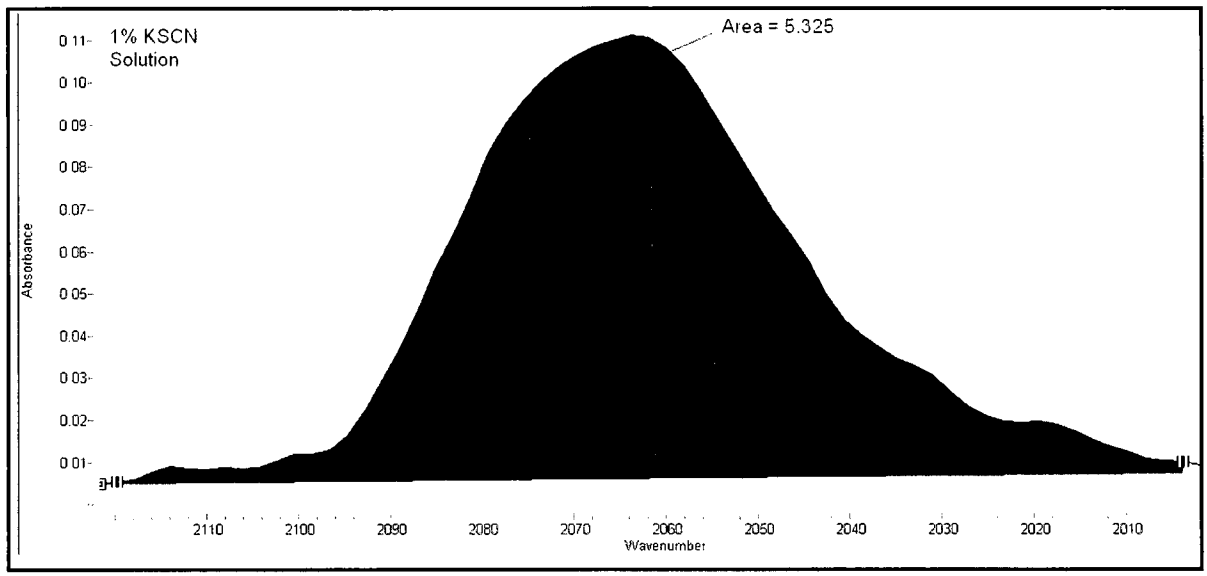

Figure 5-3: Area under the 2065 cm^{-1} peak between 2200 and 2000 cm^{-1} for a 1% KSCN solution

5.4 T-Mixer

Due to their planar features and relatively inexpensive fabrication techniques, T-junction mixers have been the focus of research studies investigating mixing performance as a function of various functional parameters. These mixers combine two streams along a channel, and mixing is achieved by virtue of molecular diffusion across the fluid interface.

The aspect ratio of the mixer is an important dimensionless parameter obtained by dividing the channel height by the channel width. A large aspect ratio accelerates the molecular exchange rate between adjacent streams and consequently leads to greater mixing efficiency. Hence researchers try to maximize aspect ratios by increasing the height of the channel relative to its width, or by

decreasing the width of the channel relative to its height (Gobby et al., 2001). For practical applications, the former approach is pursued because it incurs a smaller pressure drop during fluid flow.

The flow rate of the inlet streams also determines the extent of mixing in T-Junction mixers (Engler et al., 2004). At low flow rates, the laminar regime restricts flow segmentation and mixing is diffusion limited. With increasing flow rates, vortices begin to form as the opposite streams collide at the junction, and eventually cause a complete breakdown of ordered flow trajectories. Hence mixing quality improves substantially at higher flow speeds ($Re > 50$).

For this study, a cross-shaped mixing device with three inlets and one outlet was fabricated on a calcium fluoride substrate using polymer spin-on techniques addressed in Chapter 4. The dimensions of the mixer are shown in Figure 5-4. In order to realize a T-shaped configuration, the top inlet was blocked by forcing a plug through its external connecter. Furthermore, the channels near the junction were convoluted to disrupt the orderly flow pattern observed in the laminar regime. It was expected that flow past these serpentine elements would induce flow separation and eddy generation. Eddies would not only reduce the molecular diffusion distance, but they would also create a larger diffusional area between adjacent streams to facilitate the mixing process.

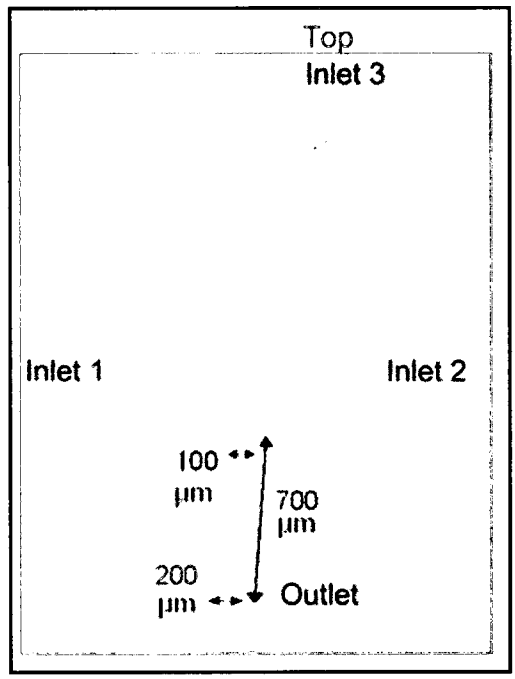

Figure 5-4: Image of Cross-Shaped Mixing Device. Mixing performance was analyzed at 700 micrometers from the junction

5.4.1 Numerical Simulations

Figure 5-5 represents a 3D hexahedral-element mesh generated in Gmsh® prior to running the numerical simulation. For investigating the influence of aspect ratio on mixing performance, the channel width was fixed to 200 μm at a distance of 700 μm from the junction, while the channel height was varied such that the aspect ratio increased from 0.1 to 1. Data from an observation plane spanning with width of the channel was plugged into Equation 5-1 to obtain mixing efficiency. The results, tabulated in Table 5-1, indicate that increasing the aspect ratio improved mixing efficiency and relieved the pressure drop within the mixer.

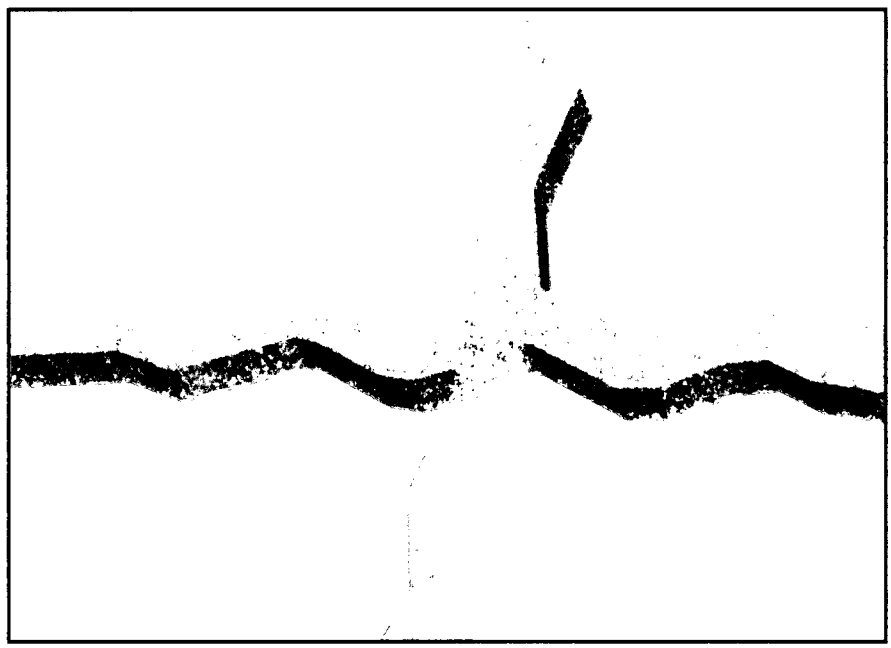

Figure 5-5: Image of Cross-Shaped Mesh used for numerical modeling of flow. The volume of the mesh is 46.80 nL

Aspect Ratio	Mixing Efficiency (%)	Pressure Drop (MPa)
0.20	15.0	10.6E-03
0.40	18.8	3.20E-03
0.60	23.0	1.83E-03
1.00	31.2	1.01E-03

Table 5-1: Influence of channel aspect ratio of mixing performance and pressure drop

The serpentine elements integrated into the outlet channel of the T-junction mixer also started to play an important role with increasing aspect ratios. As seen from Figure 5-6, the interface of the two liquids started to curl under the action of flow circulations brought about by the bends. Since the curling motion was time-independent, quantitative analysis of mixing by infrared detection could be complicated. If the degree of mixing at any particular point in the channel was varying with time, then co-addition of spectra collected over time to increase the S/N ratio would not be valid since this practice is based on the assumption that the signal is invariant.

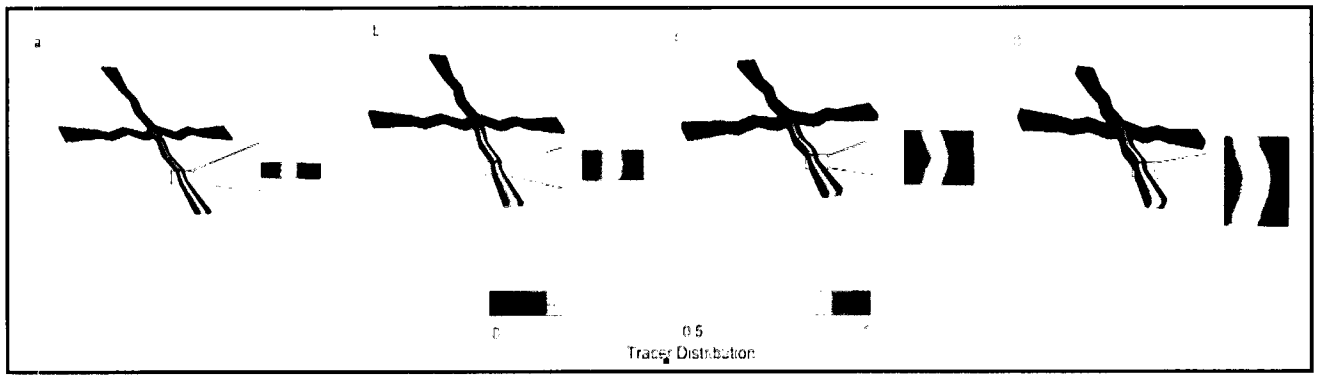

Figure 5-6: Mass Fraction Contours showing the influence of aspect ratio on mixing homogeneity. Tracer is introduced from the left inlet. (a) Aspect Ratio = 0.2, (b) Aspect Ratio = 0.4, (c) Aspect Ratio = 0.6 & (d) Aspect Ratio = 1.0

For investigating the influence of flow rates on mixing efficiency, the flow rates of Fluids A and B were varied between 0.05 and 0.6 ml/min, while the channel aspect ratio was fixed at 0.4. As the two fluids converged into the outlet channel, the flow velocity increased under the influence of pressure. For the above volumetric flow rate range, these speeds varied between 0.04 and 0.44 m/s respectively. With knowledge of flow speeds (v) and channel dimension (D), the Reynolds number (Re) was determined by Equation 2-1 using the viscosity of water ($\nu=1\times10^{-06}$ m^2/s). Table 5-2 lists the mixing efficiency obtained for each Reynolds number at 700 μm from the junction. Since the number was below 50, mixing performance was significantly poor. However, it does show signs of improvement at higher flow rates indicating the onset of turbulence.

Furthermore, the fluid stirring effect stemming from the serpentine elements was also absent within this speed range. This can be observed from Figure 5-7, which displays the mass fraction contours at 700 μm from the junction for four different inlet velocities. The figure also illustrates the diffusive broadening of a completely mixed solution confined to the central portion of the mixer.

Inlet Flow Rate (ml/min)	Outlet Channel Liquid Velocity (m/s)	Reynolds Number	Mixing Efficiency (%)
0.050	0.042	2.7	12
0.15	0.11	6.7	12
0.30	0.24	14	14
0.60	0.44	27	24

Table 5-2: The influence on flow rate on mixing performance in T-Junction mixers. Mixing efficiency was computed at 700 μm from the junction

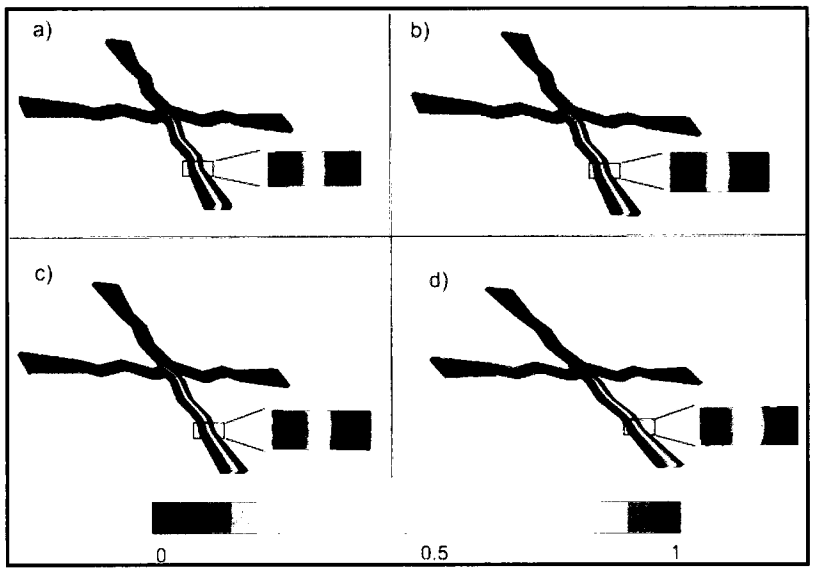

Figure 5-7: Mass Fraction Contours showing the influence of Reynolds number on mixing performance. Tracer is introduced from left inlet. (a) Re = 2.70; (b) Re = 6.7; (c) Re = 14; & (d) Re = 27

5.4.2 Experimental Validation

During the fabrication of the T-Junction mixer, the height of the microchannel was fixed at 40 micrometers, and therefore the effect of aspect ratio on mixing performance could not be validated experimentally. Nonetheless, several measurements were made to investigate the influence of inlet flow rates on mixing efficiency within the T-mixer. These experiments relied on optical detection to

quantify the extent of mixing of a blue color dye with a colorless solution. Hence a calibration curve was formulated (Figure 5-8) using an approach discussed in section 5.3.1.1.

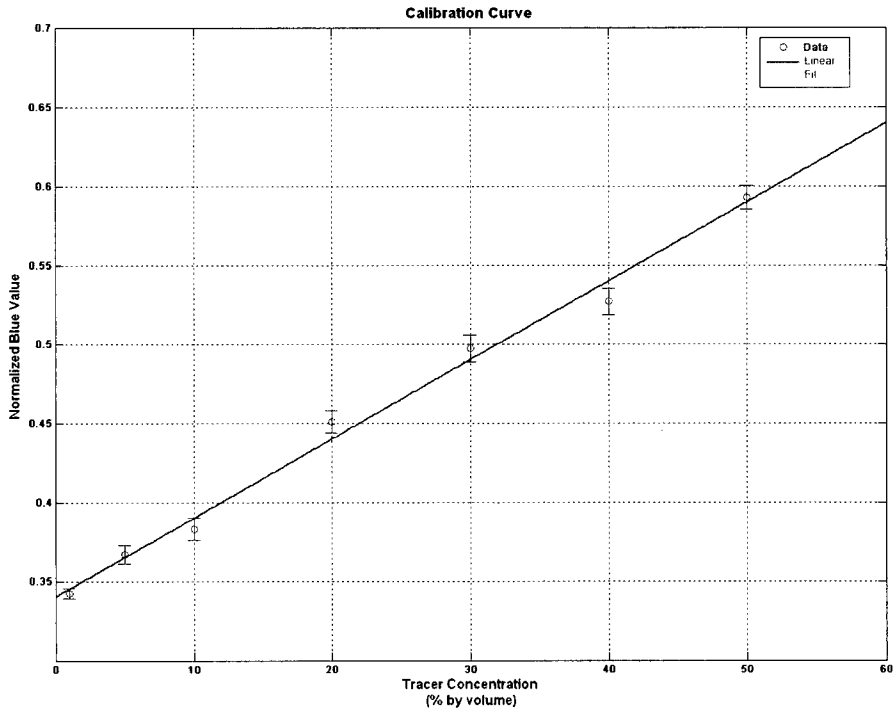

Figure 5-8: Calibration Curve for dye-based solutions. Linear regression analysis gives a line with slope (β) = 0.005, intercept (α) = 0.341 and R^2 = 0.992

For the purpose of comparison with numerical predictions, the solutions were injected at flow rates between 0.05 and 0.6 ml/min. Images of the mixing process were captured after a delay of 1 minute following the arrival of solutions into the mixer. This time interval was sufficient to allow a steady flow profile to develop. Thereafter, each image was converted into a matrix of concentration values using the calibration curve of Figure 5-8. A row from the matrix of concentration values, corresponding to a distance of 700 μm from the junction, was used to calculate mixing efficiency.

The graph in Figure 5-9 plots the mixing efficiency versus inlet flow rate for the numerical and experimental runs. Interestingly, the numerical prediction of mixing performance starts to deviate from the experimental result at higher flow rates. This disagreement could be attributed to computational errors in the numerical model; however, images captured from the junction indicate a flow artifact as a possible reason for the improved mixing in experimental runs (Figure 5-10). Despite efforts to block the top inlet with a plug, it was observed that the blue dye solution had an

increasing tendency to infiltrate the top inlet at higher flow rates. As vortices began to develop at the junction, some fluid elements from the stagnant blue dye solution broke away from the top inlet and formed striations that entered the outlet channel. This increase in dye concentration in the outlet channel accounted for the apparent improvement in mixing efficiency.

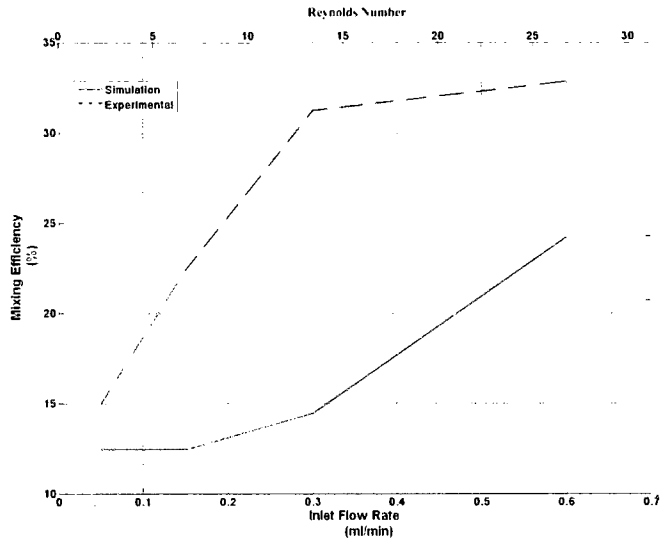

Figure 5-9: Graph showing the influence of flow rates on mixing efficiency in a T-junction mixer. Numerical (red/solid) versus Experimental (blue/dashed)

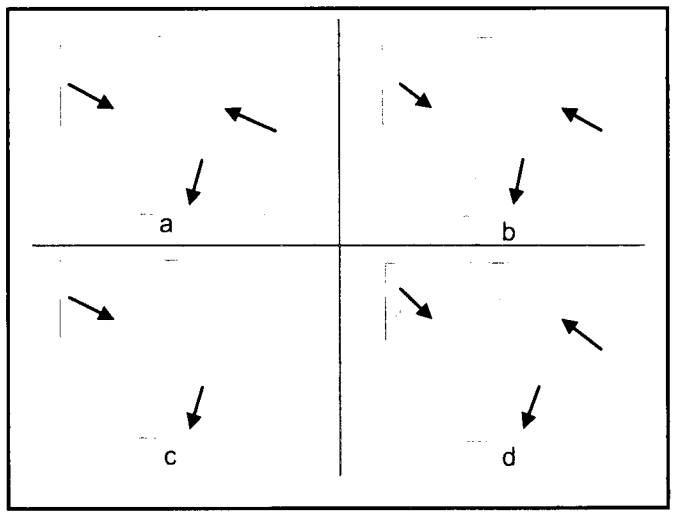

Figure 5-10: Mixing performance as a function of flow rates. (a) 0.05 ml/min, (b) 0.15 ml/min, (c) 0.30 ml/min and (d) 0.6 ml/min. Arrows indicate direction of flow. The apparent increase in mixing at higher flow rates is an experimental artifact (see text)

5.5 Flow-Focusing Mixer

Flow focusing by hydrodynamic or geometric constriction squeezes adjacent fluid streams into close proximity that consequently decreases the molecular diffusion distance and improves mixing performance. Hydrodynamic focusing uses sheath flows to envelope a central stream in order to achieve ultra-fast mixing (Knight et al., 1998). However, the approach does not yield a homogenous sample as mixing is confined to the central portion of the channel.

Studies conducted with flow-focusing mixers indicate the importance of flow rate differential between the top and side inlets on the width of the focused stream (Knight et al., 1998). A dimensionless number, α, obtained by dividing the side inlets velocity by the top inlet velocity determines the nature of flow within the mixer. Above $\alpha_{max} = 1.28$, the fluid from the side inlets forces its way into the top inlet. On the other hand, fluid from the top inlet enters the side inlets below $\alpha_{min} = 0.48$. Hence it is crucial to remain within this range if flow focusing is desired.

The benefits of flow focusing by hydrodynamic means were investigated by employing the cross shaped mixer shown in Figure 5-1. The top inlet of the mixer, which had previously been blocked to accomplish a T-junction configuration, was opened to function as a conduit for the central stream.

5.5.1 Numerical Simulations

The influence of α on the flow profile in a flow-focusing mixer was investigated using numerical simulations. The volumetric flow rate of Fluid A from the side inlets was kept at a constant value of 0.05 ml/min, while the flow rate of Fluid B from the top inlet was varied between 0.05 and 0.2 ml/min. Values extracted from the resulting velocity profile for each scenario are tabulated in Table 5-3.

Case	Side Inlets Velocity	Top Inlet Velocity	Outlet Velocity	Reynolds number	α (side ÷ top)
	(m/s)	(m/s)	(m/s)		
1	0.040	0.040	0.12	7.1	1.0
2	0.040	0.080	0.15	8.8	0.50
3	0.040	0.16	0.20	11	0.25

Table 5-3: The influence of α on fluid velocity in the outlet channel

It was expected that with decreasing values of α, Fluid B would start to penetrate the side inlets, but this was not observed in the mass fraction surface contour plots shown in Figure 5-11. It appears that due to the inefficient meshing within the junction, the simulation was unable to correctly resolve flow trajectories emanating from the top channel. Consequently, the numerical prediction of mixing behavior for this mixer was used as a qualitative estimate.

Mixing efficiency was obtained through statistical treatment of the mass fraction of tracer present in Fluid A at an observation plane located 700 μm from the junction. The results are presented in Table 5-4. As anticipated, increasing the top inlet velocity (decreasing α) allowed an excess of tracer to enter the outlet channel and resulted in a broader focused stream (Figure 5-11c). Mixing was essentially complete within this focused plug, which was seen to broaden downstream from the junction. This was in contrast to a reported study (Knight et al., 1998) in which the focused stream maintained its width. Such a discrepancy was attributed to the increase in channel width downstream from the junction, as well as the influence of serpentine elements within the outlet. Under these circumstances, the focused stream was influenced by secondary flows occurring within the bends at faster flow speeds.

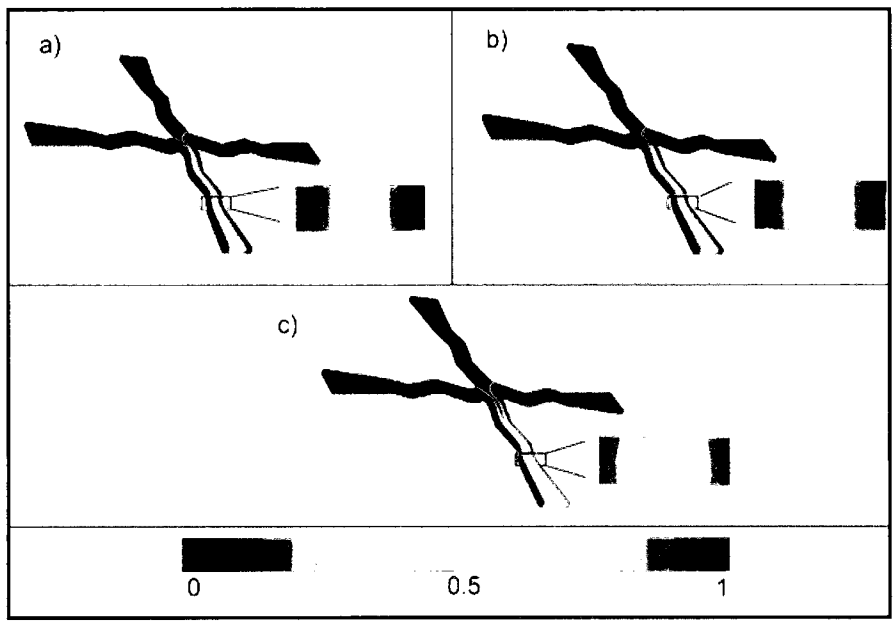

Figure 5-11: Mass fraction contours at different values of α. Tracer is introduced from the side inlets. (a) α=1.0, (b) α=0.5 and (c) α=0.25

Top Inlet Flow Rate (ml/min)	Side Inlets Flow Rate (ml/min)	Outlet Channel Flow Speed (m/s)	α	Mixing Efficiency (%)
0.050	0.050	0.12	1.0	22
0.10	0.050	0.15	0.50	32
0.20	0.050	0.20	0.25	45

Table 5-4: Influence of α on the mixing performance of a flow focusing mixer

5.5.2 Experimental Validation

Due to inconsistencies present in the numerical predictions of flow phenomena within the focusing region, it became essential to experimentally investigate the dependence of flow behavior on different magnitudes of α-values (side inlet velocity ÷ top inlet velocity). The extent of mixing was monitored optically by observing the variation in color intensity of a blue color dye as a function of top inlet flow rate. The dye was injected from the side inlets while a colorless solution was introduced from the top inlet. For the purpose of comparison with numerical predictions, the flow rate of the blue color dye was kept constant at 0.05 ml/min while the flow rate of the solution was varied between 0.05 and 0.2 ml/min. Once a steady flow profile had developed, colored images of the mixing process from the junction as well as the outlet channel were captured through a microscope at 40X magnification with a CCD camera.

Experimental results illustrating the phenomenon of flow focusing within the junction are shown in Figure 5-12. For $\alpha = 0.25$ (Scenario c), the colorless solution is seen to penetrate the upper regions of the side channels. This penetration is greater for the right channel due to its geometrical proximity with the top inlet. Based on a similar argument, it can be claimed that flow from the top inlet would be unable to completely halt the supply of blue dye from the left inlet for $\alpha < 0.25$. However, this assumption could not be verified because the syringe pump was incapable of injecting fluid at a higher flow rate into the top inlet.

Images captured from the outlet channel were mathematically processed using the techniques mentioned in Section 5.3.1. Since the same cross-shaped mixer was used for the flow-focusing investigation, the calibration equation computed for the T-junction mixer was used. In order to quantitatively determine the extent of mixing as a function of α, data from a row corresponding to a distance of 700 μm from the X-junction was inserted into Equation 5-1. The resulting mixing

efficiency was plotted against flow rate, and the graph is displayed in Figure 5-13. For comparative purposes, the numerical predictions of mixing are also plotted on the graph. An obvious discrepancy is observed between numerical simulations and experimental results, with the former predicting greater mixing. This difference is due to the excessive amount of fluid transfer between the top inlet and the outlet in the numerical model, which tends to over-predict mixing performance.

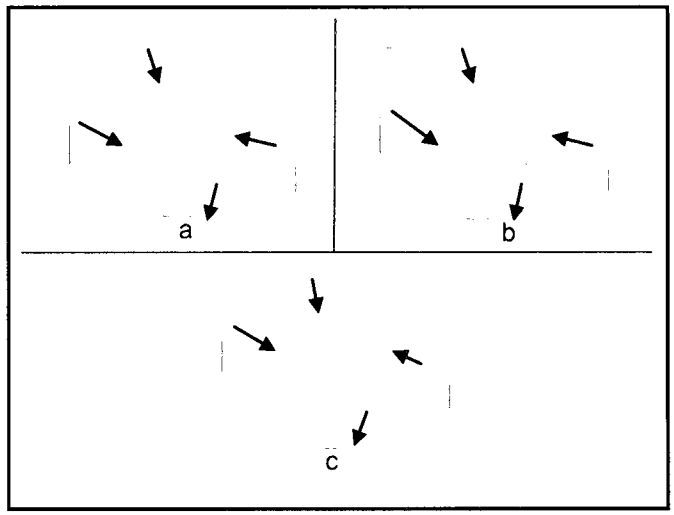

Figure 5-12: Experimental investigation into the influence of α on flow patterns. (a) α = 1.0, (b) α = 0.5 and (c) α = 0.25. Arrows indicate direction of flow

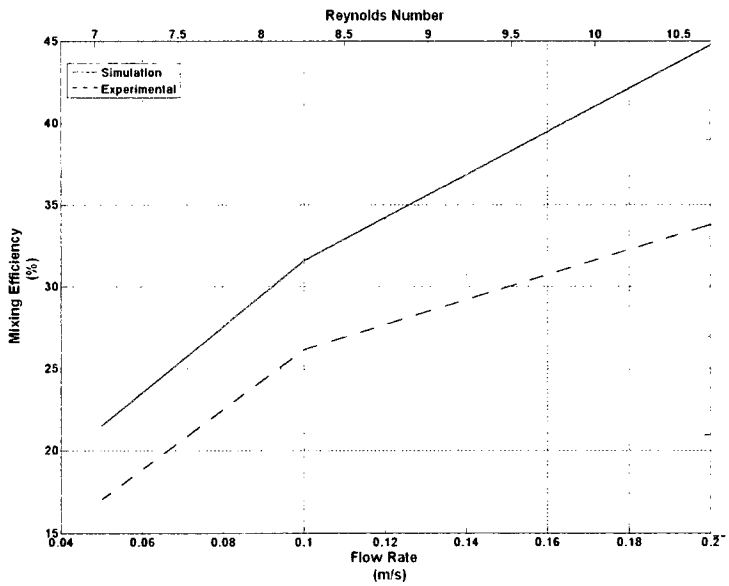

Figure 5-13: Graph showing the influence of flow rates on mixing efficiency of flow focusing mixer. Numerical (Red/Solid) versus Experimental (Blue/Dashed)

5.6 Multi-Lamination Mixer

As evidenced by the results reported so far, mixing efficiency improves with an increase in contact area between adjacent streams and with a reduction in the molecular diffusion distance. Both these traits can be combined in multi-lamination mixers, which integrate multiple streams into a single channel in a manner that creates alternating layers of differing fluids. These mixers can be realized either through two-dimensional parallel lamination, whereby multiple inlets converge into a central stream or through an interdigital feed arrangement of smaller laminae.

For this study, the latter technique was implemented. A three-dimensional mesh was used to split an incoming stream into six filaments, each having a width of 30 μm. These filaments were superimposed onto another set of filaments formed from a second stream such that an interdigital feed arrangement was accomplished. Hence 12 alternating layers of fluids A and B were combined in a 300 μm wide outlet channel where mixing was monitored. The dimensions of the channel are shown in Figure 5-14.

Optimal flow rate is essential for achieving a homogenous blend between two liquids in a multi-lamination mixer. Studies have shown that higher flow rates tend to reduce the residence time of fluids in the outlet channel (Koch et al., 1999). Consequently, filaments of differing fluids have less time to interact with one another, resulting in poor mixing performance. On the other hand, slow rates can promote premixing of fluids within the overlapping mesh region prior to the point of confluence.

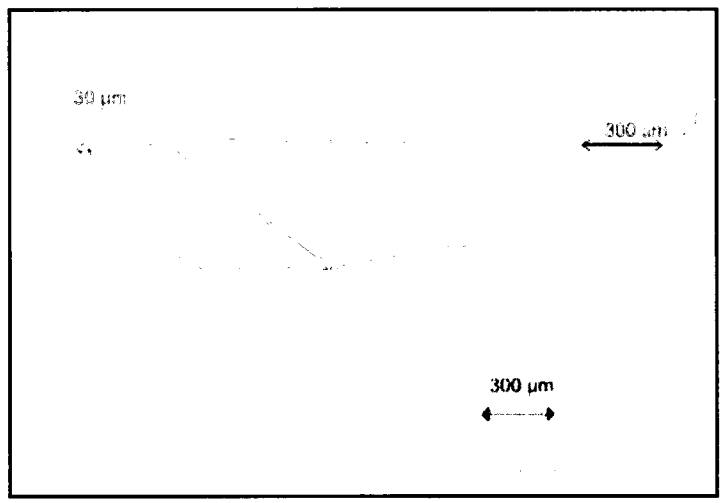

Figure 5-14: Image of a multi-lamination mixing device. Flow performance was investigated at 200 micrometers from the point of merger

5.6.1 Numerical Simulations

Due to the complex geometry of the multi-lamination mixer, the characteristic length of each mesh element was reduced to generate a highly dense mesh comprising of 662,884 hexahedral elements and filling a mixer volume of 49.13 nL. Figure 5-15 illustrates a central portion of the mesh.

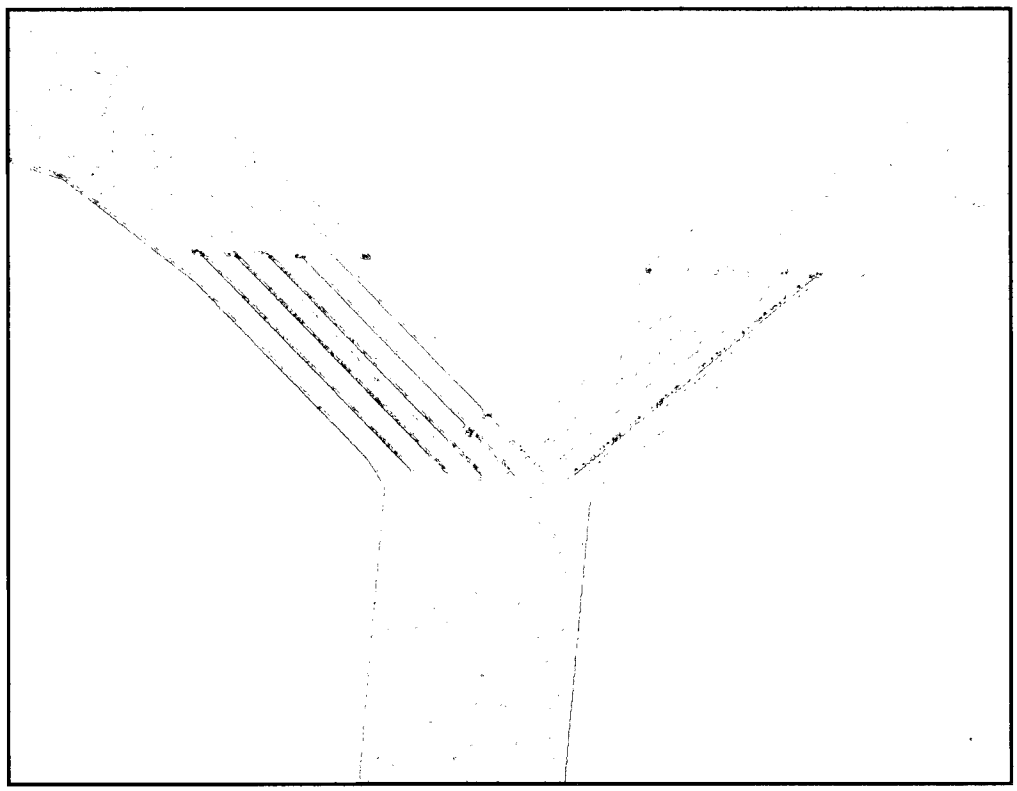

Figure 5-15: A 662,884-element mesh occupying a volume of 49.13 nL used for modeling of mixing in a multi-lamination mixer

Given the significant influence of fluid velocity on mixing behavior, the mixing of Fluids A and B was simulated at flow rates ranging between 0.05 and 0.2 ml/min. However, as seen from the simulation results presented in Table 5-5, mixing performance is marginally influenced by changing flow rates. In order to gain a better understanding of the mixing phenomenon and rule out the occurrence of premixing in the overlapping domain, cross-sections at various length of the outlet channel are displayed in Figure 5-16. While the mass fraction contours indicate signs of slight premixing within the mesh, the bulk of mixing occurs in the outlet channel.

Flow Speed in Outlet Channel (m/s)	Reynolds Number	Mixing Performance (%)
0.015	1.1	64
0.025	1.8	64
0.052	3.7	63
0.11	7.4	65

Table 5-5: Influence of flow speeds on mixing performance in a multi-lamination mixer

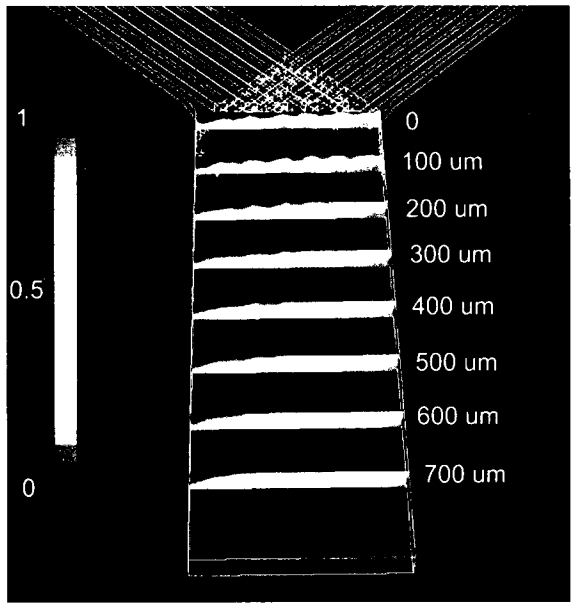

Figure 5-16: Mass fraction contours at various lengths downstream from the point of merger. Fluid velocity in the outlet channel was 0.015 m/s

5.6.2 Experimental Validation

To support the result obtained from the simulations, it was necessary to undertake an experimental approach in which two different liquids were mixed within the multi-lamination device. The syringe supplying the right inlet was filled with pre-filtered blue color dye that had been diluted to 50% with water. The left inlet was supplied with a 4% colorless potassium thiocyanate solution. The pump was programmed to dispense at a set flow rate, and mixing was simultaneously observed using optical and infrared detection. In order to obtain meaningful data that could be compared with

results from the simulation, optical and infrared calibration was performed using techniques addressed in sections 5.3.1 and 5.3.2. Figure 5-17 illustrates the linear relationship between blue dye concentration and the resulting pixel weight, while Figure 5-18 represents the linear relationship between potassium thiocyanate concentration and the resulting peak area.

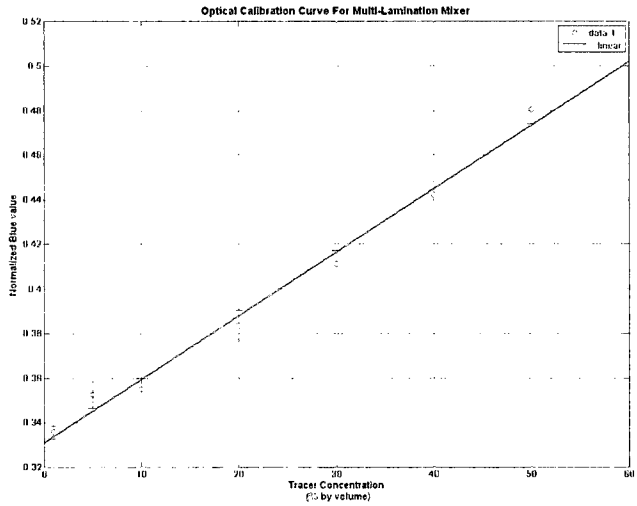

Figure 5-17: Calibration curve obtained from optical detection of different concentrations of blue dye in the multi-lamination mixer. Linear regression gives a line with slope (β) = 0.003, intercept (α) = 0.331 and $R^2 = 0.989$

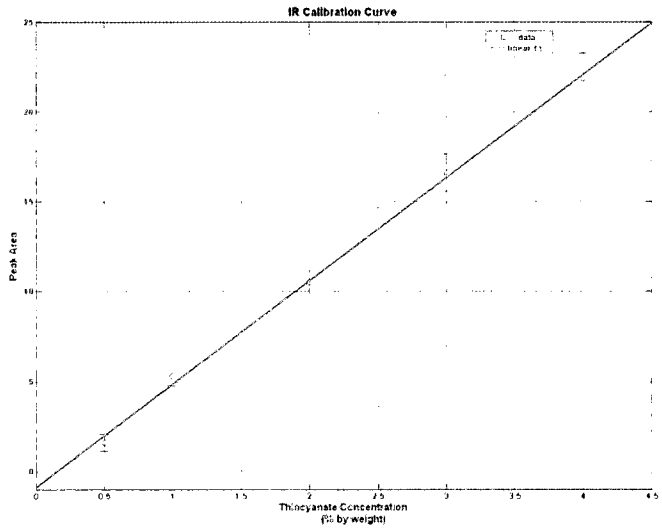

Figure 5-18: Calibration curve obtained from infrared analysis of potassium thiocyanate solutions of different concentrations in the multi-lamination mixer. Linear regression gives a line with slope (β) = 5.74, intercept (α) = -0.88 and $R^2 = 0.998$

Mixing performance at each flow rate was quantified optically by mapping the variation in blue color intensity across the length of the outlet channel. Data from a specific row corresponding to a distance of 200 μm from the point of confluence was extracted from the concentration matrix and inserted into Equation 5-1. The resulting mixing efficiency was plotted against the flow rate, and the graph is displayed in Figure 5-19. The plot shows a very good correlation between numerical predictions and experiments.

As mentioned before, the distribution of potassium thiocyanate (KSCN) was quantitatively monitored through infrared detection. Prior to the actual experiment, the mixer was carefully positioned such that the region of interest, located at 200 μm from the point of confluence, was located within the field of view of the FPA detector. Once a steady flow profile had developed, an infrared image was collected by co-adding 32 scans at a resolution of 8 cm^{-1}. This image was represented by 16-by-16 pixel elements, with each pixel corresponding to the area under the 2065 cm^{-1} peak in the KSCN spectrum. Using the calibration curve obtained from Figure 5-18, the infrared image was transformed into a concentration matrix. Figure 5-20 illustrates four concentration maps for flow rates of 0.05, 0.1, 0.2, and 0.4 ml/min. Data from a specific row corresponding to a distance of 200 μm from the point of confluence was entered into Equation 5-1 and the resulting mixing efficiency is tabulated in Table 5-6. There is good agreement between the results of the optical and infrared experiments.

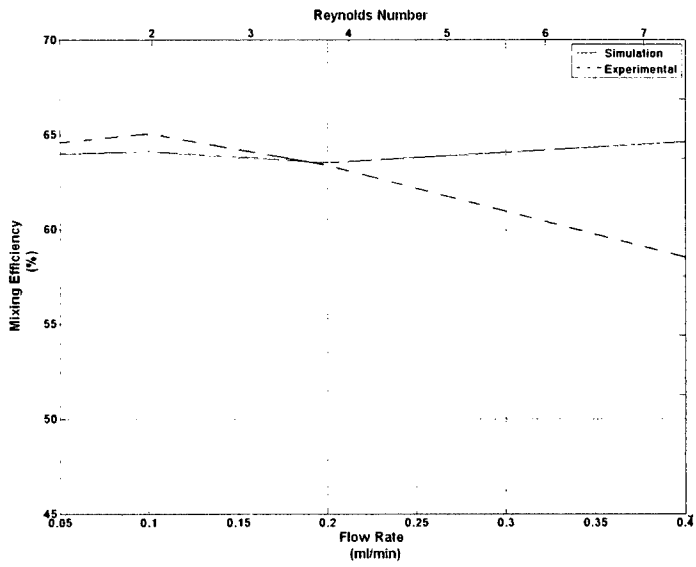

Figure 5-19: Graph showing the influence of flow rates on mixing efficiency of the multi-lamination mixer. Numerical (red) versus Experimental (blue)

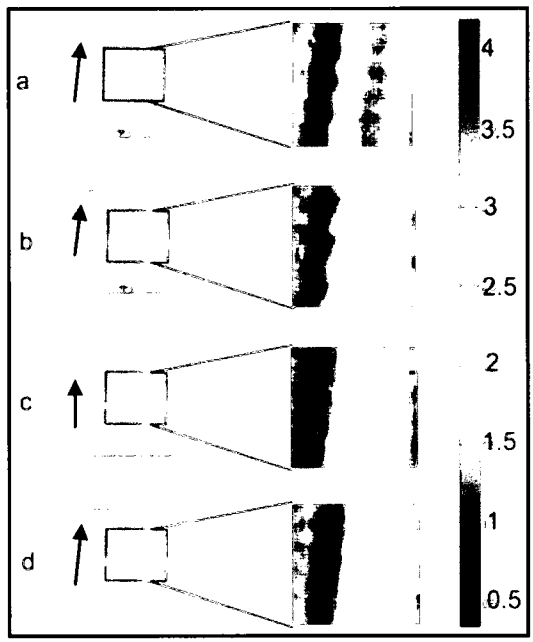

Figure 5-20: FTIR detection of mixing between potassium thiocyanate (red) and water (blue) at various flow rates. (a) 0.05 ml/min, (b) 0.1 ml/min, (c) 0.2 ml/min and (d) 0.4 ml/min. Optical images of mixing between a blue dye and clear KSCN solution are shown for comparison.

Inlet Flow Rate (ml/min)	Fluid Speed in Center Channel (m/s)	Reynolds Number	Mixing Efficiency (Optical) (%)	Mixing Efficiency (Infrared) (%)
0.05	0.015	1.1	65	64
0.10	0.025	1.8	65	58
0.20	0.052	3.7	63	65
0.40	0.11	7.4	59	58

Table 5-6: A comparison between optical and infrared detection techniques used to investigate mixing in a multi-lamination device at 200 micrometers from the point of merger

5.6.3 Chemical Reaction

The cross-sectional depictions of tracer mass fraction in Figure 5-16 showed that unmixed liquids were stratified horizontally within the outlet channel. This could result in an over-estimation

of mixing performance (Wong et al., 2004). Hence it was important to monitor the extent of mixing by visualizing a chemical reaction that produced a color change only upon complete mixing of two reactant liquids.

For this reason, a reaction between ferric chloride and potassium thiocyanate was investigated. This reaction resulted in an instantaneous formation of an iron-thiocyanate complex characterized by a dark red color. A 4% colorless potassium thiocyanate solution was injected into the right inlet while a mildly yellowish 0.4% ferric chloride solution was introduced into the left inlet. Both solutions were flown at a volumetric flow rate of 0.2 ml/min.

Due to the small pathlength (40 μm) of the mixer, the iron-thiocyanate complex appeared as light brown as shown in Figure 5-21. The color change was apparent right from the point of confluence between liquid filaments and maintained its color intensity towards the end of the outlet channel. Based on this observation, it was concluded that improvement in mixing performance for the multi-lamination mixer was not an artifact resulting from averaging the absorption of horizontally stratified blue dye solutions.

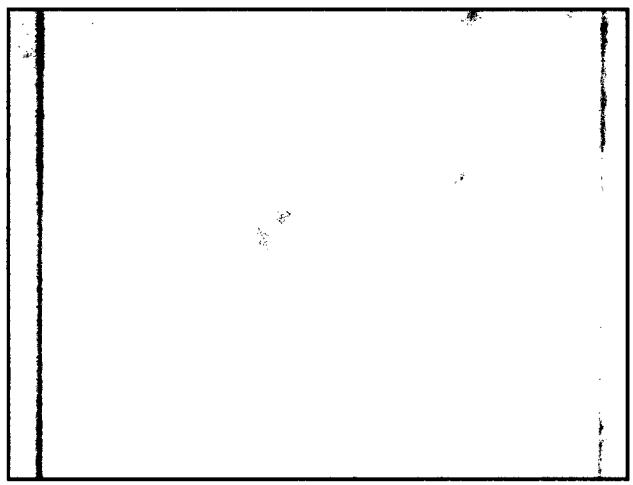

Figure 5-21: Visualization of a rapid chemical reaction between ferric chloride and potassium thiocyanate. The fluids were injected at a rate of 0.4 ml/min. Homogenous mixing is indicated by the formation of a brown colored iron-thiocyanate complex

5.7 Summary

Polymer spin-on techniques were used to fabricate three different micromixing devices whose performance was investigated using optical and infrared detection. Table 5-7 presents the best case scenario in terms of mixing efficiency for the three devices. A substantial improvement in mixing

efficiency is evident for the multi-lamination mixer. This is not surprising since the device increases the area available for diffusion by segmenting the flow into minuscule liquid filaments. By combining filaments of differing fluids in an alternating fashion, the diffusion distance that the molecules must travel is reduced significantly. Hence the increase in diffusion rate allows mixing to complete on a shorter timescale. It is also interesting to note that mixing performance in the multi-lamination mixer was marginally affected by the flow rate. This has important ramifications for researchers wishing to investigate dynamic events on different timescales.

Mixing Device	Mixing Efficiency (%)	Fluid velocity at optimum mixing efficiency (m/s)
T-Junction	33	0.45
Flow Focusing	34	0.19
Multi-Lamination	65	0.02-0.11

Table 5-7: A comparison between three mixing devices in terms of mixing performance. Also presented are fluid velocities in the outlet channel at optimum mixing efficiency

6. Investigating of Protein Folding Kinetics

6.1 Overview

This chapter focuses on the application of a rapid mixing device to initiate a conformational change in the secondary structure of milk protein, β-Lactoglobulin. The progress of the reaction was monitored by time resolved Fourier transform infrared (FTIR) spectroscopy with the use of a focal plane array (FPA) detector. For the first experiment, the monomeric protein was rapidly diluted with an alkaline solution to initiate a monomer→dimer transition. Equilibrium studies were conducted for a range of pH values to obtain reference spectra for the subsequent kinetic experiment. In a second experiment, the conformational changes in native β-Lactoglobulin induced by rapid mixing with trifluoroethanol (TFE) were monitored in real time.

6.2 pH Jump via Rapid Dilution

The conformational equilibrium of proteins can be destabilized by a rapid change in their environment causing them to unfold. Similarly, a favorable change such as a pH jump administered to a protein kept under unstable conditions can trigger it to fold back to its native state. In order to capture important kinetic events occurring during the protein refolding process, it is essential to induce a chemical change from fully denaturing to strongly stabilizing conditions in the shortest time interval. Rapid dilution using continuous flow mixing techniques can instigate such a change as evidenced from recent studies (Lapidus et al., 2007, Marinkovic et al., 2000).

The objective of this study was to investigate the conformational changes induced in β-Lactoglobulin resulting from a pH jump. A multi-lamination mixing device designed to achieve rapid mixing of liquids was used as a triggering agent. The process was monitored by time resolved FTIR spectroscopy, which has proven to be an effective probe for the investigation of reaction kinetics and protein-ligand interactions in recent years (White et al., 1995).

In order to conserve reagent volume and reduce sampling time, simultaneous detection of numerous points within a sampling region was achieved with a focal plane array (FPA) detector. This approach allowed decoupling the temporal limitation of the infrared detection technique from the process under investigation. Instead, the time resolution was determined by the spacing of adjacent detector elements in the FPA and the flow rate within the mixing device. Hence it was possible to achieve variable time resolutions by adjusting the flow rate.

6.2.1 Equilibrium Studies

6.2.1.1 Procedure

β-Lactoglobulin AB (Davisco Foods®) powder was dissolved directly in deuterated 0.1 M phosphate buffers adjusted to pH 2, 3, 4, 5.5 and 7, at a concentration of 70 mg/ml (7%). Each sample was kept in a refrigerator for 48 hours to allow for complete hydrogen-deuterium exchange. Then these samples were individually deposited between two calcium fluoride windows separated by a 50 μm spacer and transferred to an IR spectrometer (DaIRy, Thermo-Nicolet) equipped with a DTGS detector for infrared measurements.

For each spectrum, a 512-scan interferogram was collected in a single-beam mode at 4 cm^{-1} resolution. Following Fourier transformation of interferogram, the resulting spectrum was treated with a second-order derivative function between 1700 and 1600 cm^{-1} to resolve the overlapping peaks in the amide I band. The second-derivative spectrum contained negative peaks corresponding to the absorbance bands of the secondary structure (Dong et al., 1990).

6.2.1.2 Results & Discussion

Figure 6-1 presents the infrared spectra of the amide I band of β-Lactoglobulin AB as a function of pH. At neutral pH, an absorbance maximum at 1634 cm^{-1} can be observed from the figure. This wavenumber indicates a predominantly β-sheet structure based on the results of earlier studies (Papiz et al., 1986). Contributions from other secondary structure at this pH can be observed in a resolution-enhanced second-derivative spectrum (Figure 6-2a). This spectrum exhibits six bands at 1680, 1664, 1650, 1634, 1624 and 1610 cm^{-1}. These bands have been assigned to various secondary structures in previous studies (Casal et al., 1988, Dong et al., 1996).

The predominance of β-sheet structure is highlighted by peaks at 1680, 1634, and 1624 cm^{-1}. The band at 1624 cm^{-1} is suggested to play a crucial role in intramolecular interactions between adjacent β-strands as well as intermolecular interactions between dimer units (Arrondo et al., 1988). Meanwhile, the contributions from α-helix, random coils, and turns are represented by bands at 1654, 1645, and 1664 cm^{-1} respectively. However, due to an overlap between bands emanating from α-helix and random coils, the exact contribution from either component cannot be verified.

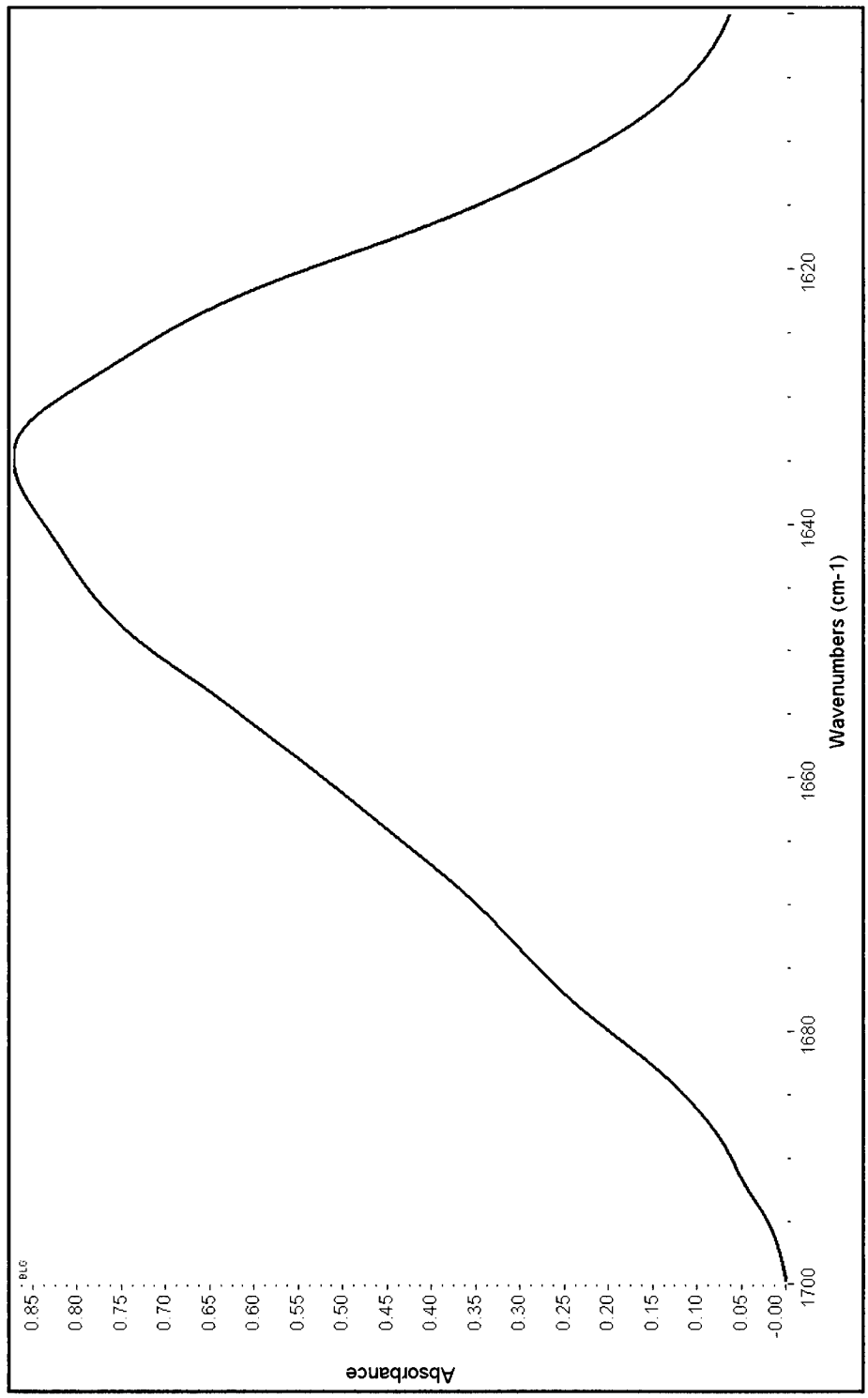

Figure 6-1: Amide I Band in the FTIR Spectrum of β-Lactoglobulin at pH 7.0

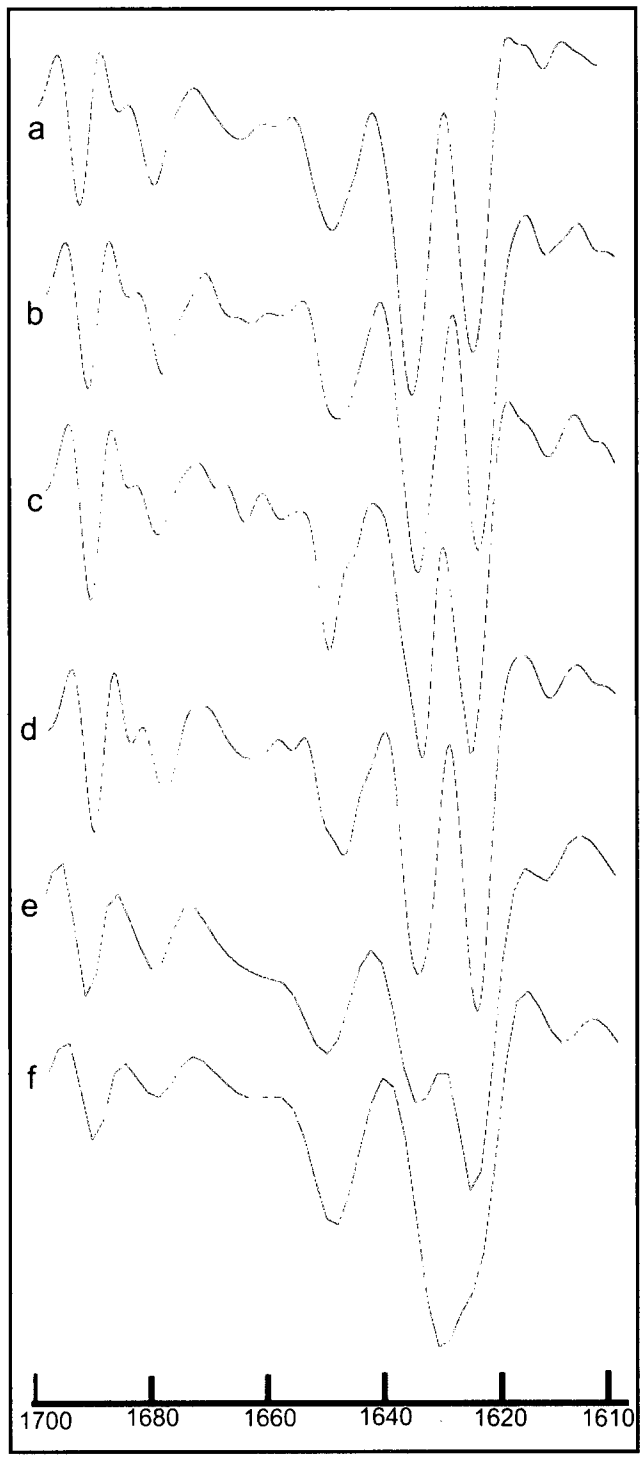

Figure 6-2: Second order derivative spectra of the Amide I band at various pH levels. (a) pH = 7.0, (b) pH = 6.0, (c) pH = 5.0, (d) pH = 4.0, (e) pH = 3.0 and (f) pH= 2.0

At pH 6.0, the spectrum resembles the native spectrum indicating negligible differences between the protein conformations at these two pH values. However, further acidification of the protein solution from pH 6.0 to 5.0 leads to a noticeable decrease of the bands at 1680 and 1634 cm^{-1} (Figure 6-2c). Since these bands are ascribed to anti-parallel β-sheets that feature prominently in the hydrophobic core of the protein, it is suggested that mildly acidic conditions affect the stability of the protein (Lefèvre and Subirade, 2001). This trend is seen to persist as the pH of the protein solution is lowered to 4.0. Beyond this pH, a modification in the quaternary structure of the protein yields octamers and other higher order oligomers (Pessen et al., 1985). Intermolecular interactions within the oligomers results in an increase in band intensity at 1624 cm^{-1} relative to the 1634 cm^{-1} band. Between pH 2.0 and 3.0, the protein depolymerizes into monomer subunits resulting in a partial loss of anti-parallel β-sheets as evidenced by the disappearance of 1634 cm^{-1} band, the relative decrease in the 1680 cm^{-1} band, and the shift of the 1624 cm^{-1} band to higher wavenumbers (Figure 6-2f).

6.2.2 Kinetic Experiment

6.2.2.1 Procedure

The multi-lamination mixer fabricated during the course of this thesis was used in continuous flow mode for administrating a pH jump to a protein sample kept under unstable conditions. This mixer was chosen for its ability to mix two distinct liquids in the shortest time possible as predicted by numerical simulations and confirmed by experimental results of Chapter 5. A FTIR spectrometer (660, Varian Inc.) equipped with a Focal Plane Array (FPA) detector coupled to a microscope was used to monitor chemical events occurring within the mixing device. The field of view of the FPA allowed the detector to probe a sampling region occupying an area of (5.6 μm x 32 μm) 180 μm^2 with a spatial resolution of ~6 μm. With knowledge of liquid flow velocities within the outlet channel, this spatial resolution could be converted into temporal resolution, thereby allowing the separation of chemical events in the time domain. For this study, the liquids were injected into the mixer at a volumetric flow rate of 0.15 ml/min. This translated into a center channel speed of 0.05 m/s as predicted by numerical simulations (Chapter 5). At this flow speed, chemical events within the mixer could be resolved with a temporal resolution of 120 μs.

Protein solutions in D_2O at pH 2.0, prepared during equilibrium experiments, were injected into the right inlet of the mixer, while a deuterated 0.1 M phosphate buffer adjusted to pH 12.0, with dilutions from NaOD, was injected into the left inlet. These solutions were pre-filtered through a

2 μm porosity filter and injected using gastight syringes (Hamilton Ltd ®) mounted on a programmable syringe pump (New Era Scientific ®). The flow profile within the mixer was allowed to stabilize before proceeding with infrared measurements. Each spectrum collected was an average of 32 scans acquired at 4 cm^{-1} resolution. In order to separate the amide I band into its components, a second-order differentiated signal was obtained from each spectrum.

6.2.2.2 Result & Discussion

In order to capture the earliest conformational changes occurring during the pH jump, the focal plane array detector was placed closest to the point of confluence between the liquid filaments as depicted in Figure 6-3. Also shown are the mass fraction contours at various lengths along the outlet channel. These contours display the degree of mixing when two liquids were simulated to mix at an inlet flow rate of 0.05 ml/min. Due to the interdigital arrangement of flow, a significant amount of horizontal stratification of unmixed liquids is seen in the initial segments of the stream. This could complicate the detection of subtle changes occurring within the protein as it transitioned from monomeric to a dimeric configuration. However, since the liquids were injected at a flow rate higher than the one used for the simulations, it was assumed that premixing in the overlapping regions of the mesh would be negligible. Furthermore, data points were collected from the center most elements of the focal plane array, along the direction of flow, where horizontal stratification of unmixed liquids was minimal. This also enabled the co-addition of spectra collected by adjacent elements along the width of the channel to improve the signal-to-noise ratio.

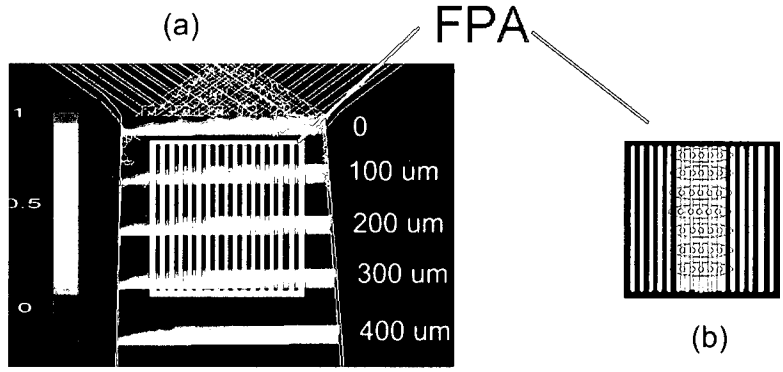

Figure 6-3: Mass fraction contours along the length of the mixing channel. (a) To collect data from regions where mixing was homogenous, only the center 5 channels (shown in pink) of the FPA were selected for data collection , (b) To improve S/N ratio, data from adjacent pixels was co-added

The stack plot in Figure 6-4 represents a series of second-order spectra showing negative peaks corresponding to the absorbance peaks of the amide I bands. Each spectrum is separated by a time delay of 120 μs, which represents the temporal resolution of the detection technique. At time, t = 0, the spectrum resembles the second-order derivative spectrum of a protein at pH 2.0, with two prominent bands at 1630 cm^{-1} (β-sheet) and 1656 cm^{-1} (α-helix). The absence of the low-frequency β-sheet component at 1624 cm^{-1} indicates that the protein is still in a monomeric state, and premixing prior to the point of confluence is negligible. With the passage of time, the effects of the pH jump surface with a decrease in the intensity of the 1656 cm^{-1} band ascribed to α-helix relative to the 1630 cm^{-1} band. By t = 2 ms, the 1656 cm^{-1} component starts to migrate towards 1645-1640 wavenumbers, a region associated with random coils. This in addition to the visible increase in turns (1665 cm^{-1}) around 3 ms indicates that the protein partially unfolds during the pH jump.

NMR data on the monomer state of β-Lactoglobulin suggests that the major α-helix of the protein reorients itself with respect to the calyx at low pH (Uhrinova et al., 2000). Furthermore, the EF loop restricts access to the binding site within the calyx by moving over it. These structural modifications, together with disordering of the terminal regions, alter the surface electrostatic properties of the protein (Fogolari et al., 1998). Hence during the pH jump, a rapid ionic change in the vicinity of the loop-α-helix interface can result in the collapse of the α-helix and an increase in disordered structure. The fact that the β-sheet content of the protein remains unaffected signifies that the β-barrel preserves its shape.

The results obtained from the pH jump experiment indicate that the monomer→dimer transition of β-Lactoglobulin is a time-consuming process that does not occur during the first 4 ms of observation. Furthermore, it proceeds through a progressive unfolding of the protein as indicated by the loss of α-helix and an accompanying increase in turns and random coils. An attempt was made to monitor events at an even higher temporal resolution; however, the mixing device was unable to accommodate the required flow rate. In addition, the alkaline buffer solution, essential for initiating the pH jump, attacked the polymer resin (SU-8) used to fabricate the microchannel. Hence repetitive pH jump experiments led to the formation of cracks, which compromised the structural integrity of the device. This scenario can be prevented by structuring the channel with polymers that are chemically resistant to strongly alkaline solutions.

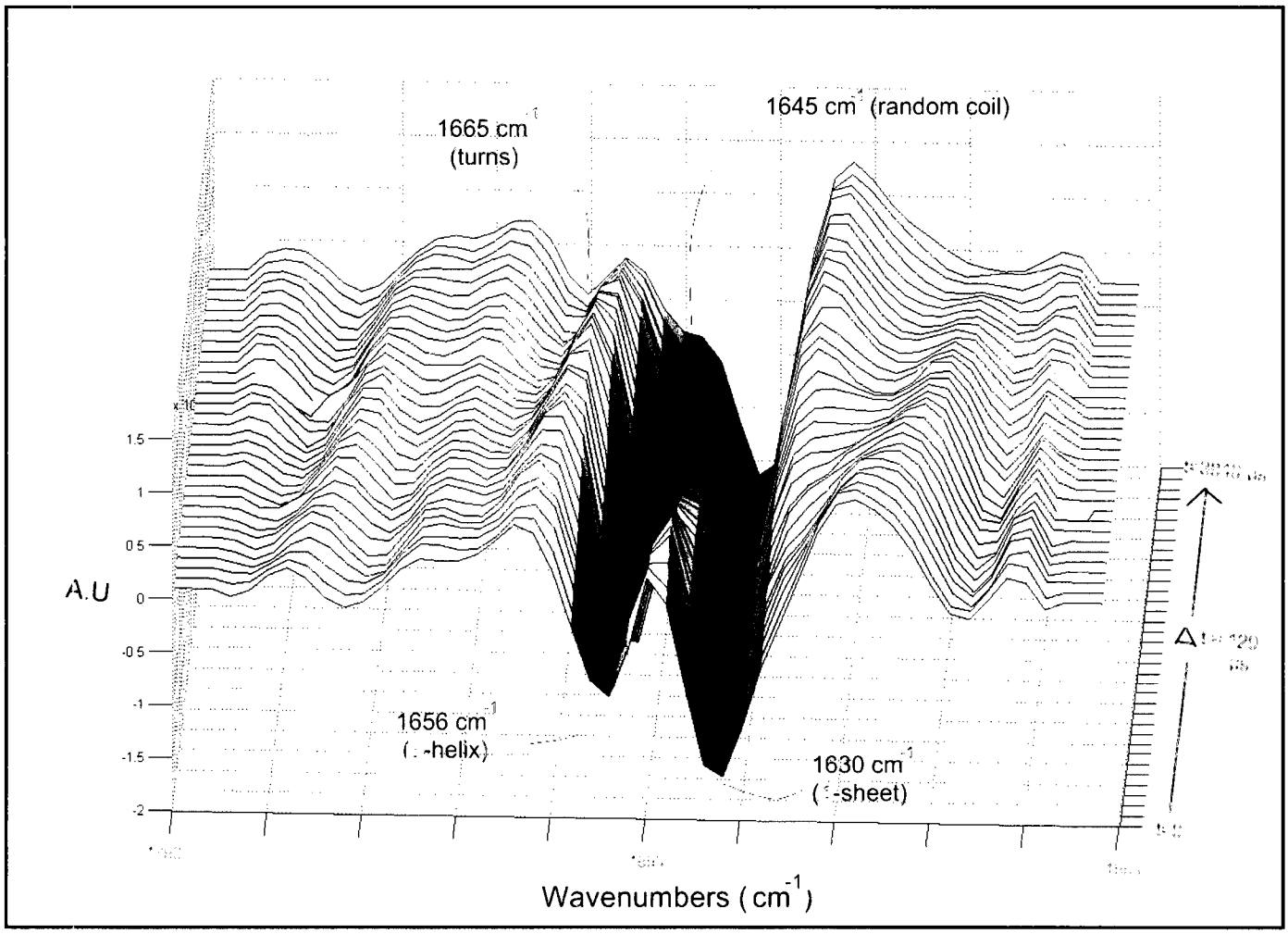

Figure 6-4: Stack plot showing a series of spectra (second order derivative) acquired during the pH Jump. Each spectrum has a time delay of 120 μs

6.3 TFE-Induced Transition

Cosolvents such as 2,2,trifluoroethanol (TFE) and ethylene glycol have been used to induce structural changes in proteins. TFE has been known to stabilize α-helices in predominantly β-sheet proteins that possess a structural preference for α-helices (Kuwata et al., 1999). It accomplishes this feat by forming hydrophobic clusters in aqueous media that weaken the non-local interactions within a protein molecule, and help establish non-native alpha-helical structures (Reiersen, 2000). In

rare instances, the alcohol has also shown to induce β hairpins and β-strands (Sonnichsen et al., 1992).

6.3.1 Kinetic Experiment

6.3.1.1 Procedure

β-Lactoglobulin AB powder was dissolved in a 0.1M deuterated phosphate buffer adjusted to a neutral pH, at a concentration of 70 mg/ml (7%). The suspension was kept in a refrigerator for 48 hours to allow for hydrogen-deuterium exchange. Meanwhile, a 60% TFE solution was prepared by adequate dilution into a 0.1M phosphate buffer also adjusted to neutral pH. Both solutions were pre-filtered through a 2 μm porosity filter prior to injection. Fluid dispensing was accomplished through a programmable syringe pump that utilized screw-actuation to deliver a constant flow rate. The protein sample was injected into the left inlet, while the TFE solution was injected into the right inlet of the multi-lamination mixer.

For this study, the flow of samples was defined at two distinct volumetric rates of 0.05 and 0.2 ml/min. Numerical modeling of flow at these rates translated to a fluid velocity of 0.01 and 0.1 m/s respectively, within the outlet channel of the mixer. Hence it was possible to monitor chemical events at two different time resolutions (600 μs and 60 μs) downstream from the point of mixing using focal plane array (FPA) detection.

The flow was allowed to stabilize for a period of 2 minutes before sampling was initiated. In order to acquire a 128-scan interferogram at a nominal resolution of 4 cm^{-1}, the flow had to be kept on for 3 minutes. After scanning, each interferogram recorded by 1024 detector elements of the FPA was Fourier transformed to yield a corresponding infrared spectrum. Absorption bands emanating from the vibrational motions of secondary structures were obscured within the Amide I band, and hence required Fourier self-deconvolution for resolving overlapping signals. The bandwidth used for the deconvolution was 22.2 cm^{-1} with a narrowing factor of 2.2.

6.3.1.2 Results & Discussion

As mentioned in section 6.2.2.2, flow artifacts occurring in the initial segments of the outlet channel can introduce spectral variability in the infrared signal. Hence data from the center most pixels of the FPA along the direction of flow was selected. These pixels sampled a fluid segment where horizontal stratification of liquids was negligible.

Low Temporal Resolution

Figure 6-5 and Figure 6-6 present the stack plot of deconvoluted amide I band spectra acquired at a low temporal resolution. Each spectrum is separated by a time delay of 600 μs. At t=0, the spectrum has a band missing at 1624 cm^{-1}. This band is assigned to exposed β-sheets that play a crucial role in intramolecular interactions between adjacent β-strands as well as intermolecular interactions between higher order structures. The disappearance of this band suggests that premixing had occurred prior to the region being monitored by the FPA. Since the experiment was carried out at a low flow rate, it is possible that the increased residence time of overlapping liquid filaments in the interdigital chamber allowed mixing to occur. Nevertheless, the spectra can still provide valuable information concerning events within a transitioning protein.

With the passage of time, a shoulder starts to develop at 1618 cm^{-1}. Eventually, this shoulder transforms into a distinct band by t = 10 ms. During the same time interval, the alpha-helical content of the protein remains unaffected as evidenced by stable band at 1650 cm^{-1}. In the next 10 ms, the newly formed band at 1618 migrates to 1614 cm^{-1}, while the 1650 cm^{-1} band increases in intensity relative to the 1636 cm^{-1} band assigned to anti-parallel β-sheets. In Figure 6-6, which represents a time window between t=21 and t=40 ms, both bands at 1614 and 1650 cm^{-1} continue to rise in intensity relative to the 1636 cm^{-1} band. The 1618/1614 bands are indicative of the formation of intermolecular β-sheet networks seen readily during aggregation and gel-formation (Jackson and Mantsch, 1992). It is also worth mentioning that the liquid coming out of the mixer had a creamy white texture resembling a gel.

A study investigating the influence of TFE on β-Lactoglobulin under equilibrium conditions reported the formation of a non-native alpha-helix transient immediately after mixing (Dong et al., 1998). This intermediate was formed at the expense of the intramolecular β-sheet whose band at 1624 cm^{-1} was absent from the initial spectra. Thereafter, the TFE-induced α-helical band decreased in time, accompanied by an increase in the intensities of bands at 1614 and 1680 cm^{-1}. Due to the time delay inherent the experiment, the authors were not able to determine the exact rates of appearance of the β-sheet aggregate bands.

Based on the results of the TFE-induced transition followed in real time, it can be suggested that the aggregate band between 1618 and 1614 cm^{-1} begins to appear in the first 10 ms following mixing, and emerges as a distinct band after 20 ms. However, the second band at 1680 cm^{-1} also

assigned to β-sheet was present during the course of the experiment. Moreover, the TFE-induced alpha-helix band at 1650 cm^{-1} was relatively stable after 40 ms and did not decrease in intensity as a function of time. This observation was contrary to the results presented in the equilibrium study mentioned above. It is plausible that the transient α-helix facilitates the formation of the intermolecular hydrogen bonded β-sheet structures that are crucial in gel formation.

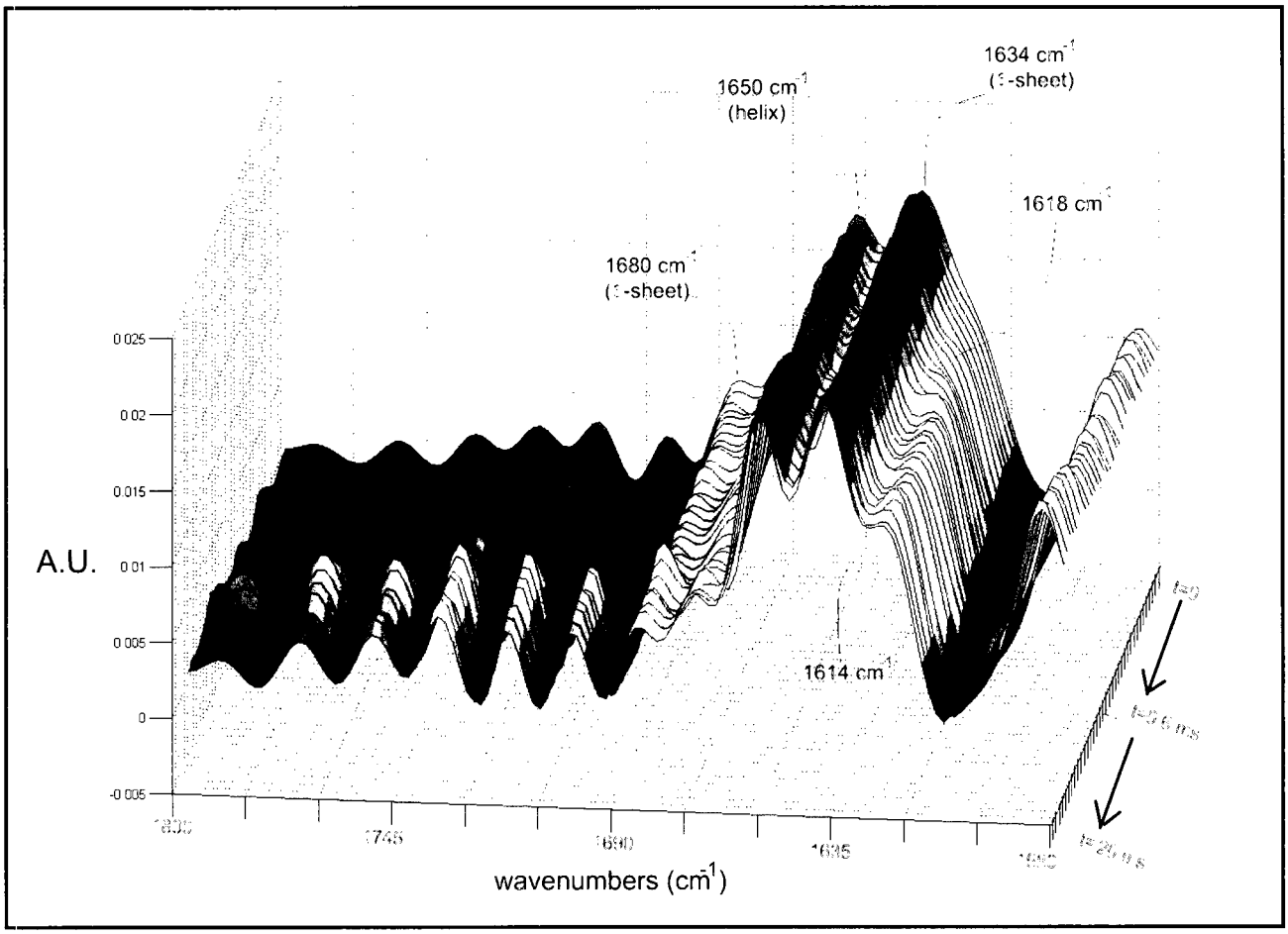

Figure 6-5: Stack plot showing a series of spectra (Self deconvoluted) obtained in the first 20 ms following TFE-BLG mixing. Each spectrum is separated by 0.6 ms

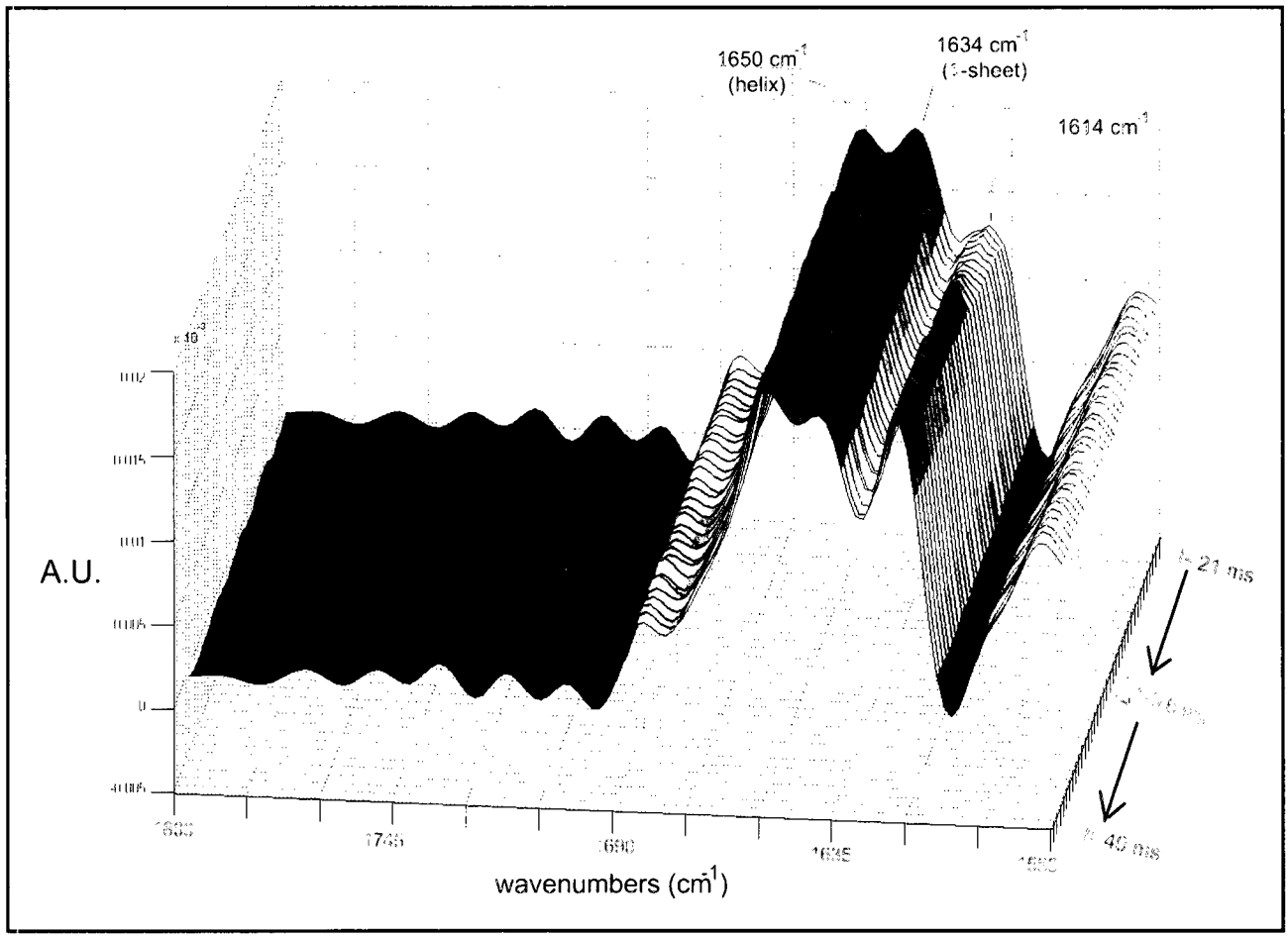

Figure 6-6: Stack plot showing a series of spectra (Self deconvoluted) obtained between 21 and 40 ms following TFE-BLG mixing. Each spectrum is separated by 0.6 ms

High Temporal Resolution

The results from the low resolution experiment indicate a significant amount of premixing between TFE and β-Lactoglobulin solutions prior to the sampling region. This was attributed to a prolonged contact between the overlapping filaments of two fluids which resulted in increased diffusion rates. Hence the next experiment was carried out at a higher flow rate of 0.4 ml/min to prevent this occurrence. Due to the proportionality between flow speed and temporal resolution, a higher flow rate also enabled the resolution of kinetic events in a microsecond time range.

Figure 6-7 presents the stack plot of deconvoluted amide I band spectra acquired at different time intervals along the direction of flow. The time delay between each spectrum is 60 μs. At t=0, the spectrum resembles the native spectrum of β-Lactoglobulin thus ruling out the occurrence of

premixing. Interestingly the augmentation of the α-helical band at 1650 cm^{-1} does not occur during the course of the experiment. Instead, the band at 1624 cm^{-1} is seen to increase and reach parity with the 1634 cm^{-1} band ascribed to anti-parallel β-sheets after 500 μs. Furthermore, another β-sheet band at 1684 cm^{-1} rises in intensity while a small shoulder appears in the 1616-1614 cm^{-1} region.

These results are surprising in light of evidence that TFE stabilizes α-helices at the expense of β-sheets in proteins with an intrinsic helical propensity (Sonnichsen et al., 1992). Data from circular dichroism spectroscopy has provided important details into the formation of a burst phase intermediate possessing a higher level of α-helical content. However, since the intermediate forms within the dead time of the experiment (18 ms), crucial information about reaction kinetics is lost (Kuwata et al., 2001). Nevertheless, it has been argued that the alcohol suppresses the action of non-local interactions from stabilizing the β-sheet network. Consequently, local interactions between adjacent residues facilitate the formation of non-native α-helices. While these TFE-induced changes may occur on millisecond timescales, the increase in β-sheet structures on the sub-millisecond time scale may be attributed to oligomerization between intermolecular β-sheets at 1624 cm^{-1}.

6.4 Summary

The effects of a pH jump on the monomer→dimer conformational change in β-Lactoglobulin were investigated by FTIR spectroscopy. The results indicate a progressive loss of α-helical content in the monomer during the course of the event. Within 20 ms of mixing, the absorbance band at 1650 cm^{-1}, ascribed to α-helix, decreases in intensity and shifts to lower wavenumbers associated with coils. This change is accompanied by the appearance of a small component at 1660 cm^{-1} related to turns. These findings are contrary to the results of an equilibrium experiment where conformational changes in protein were investigated for a range of pH values. A prominent band at 1624 cm^{-1} was present in all spectra of the amide I region of β-Lactoglobulin above pH 3.0. This band results from strongly bonded β-strands and distinguishes dimers from monomers. Hence it was suggested that despite a rapid pH jump, the protein takes time to undergo a monomer→dimer conformational change, and that partial unfolding of secondary structure might precede such a change.

Another experiment designed to explore the effects of TFE on the conformational state of β-Lactoglobulin exhibited a solvent-induced α-helix rich intermediate. This result corroborates the conclusion drawn from time-resolved circular dichroism studies where a burst-phase intermediate,

characterized by non-native α-helices, formed in the first 20 ms of observation. However, by using a much faster time resolution (0.6 ms), this study reports the formation of non-native α-helices in 10 ms following rapid dilution with TFE. Furthermore, the protein was seen to readily aggregate as evidenced by the increase in the 1624 cm^{-1} band intensity and the formation of a white gel at the outlet of the mixer. This was attributed to two primary factors: (1) a high protein concentration (7 mg/ml) occluded solvent penetration thereby favoring aggregation between intramolecular β-strands, and (2) at neutral pH, the monomer↔dimer equilibrium is shifted towards dimeric form, in which intermolecular interactions between β-sheets result in oligomerization towards higher order structures.

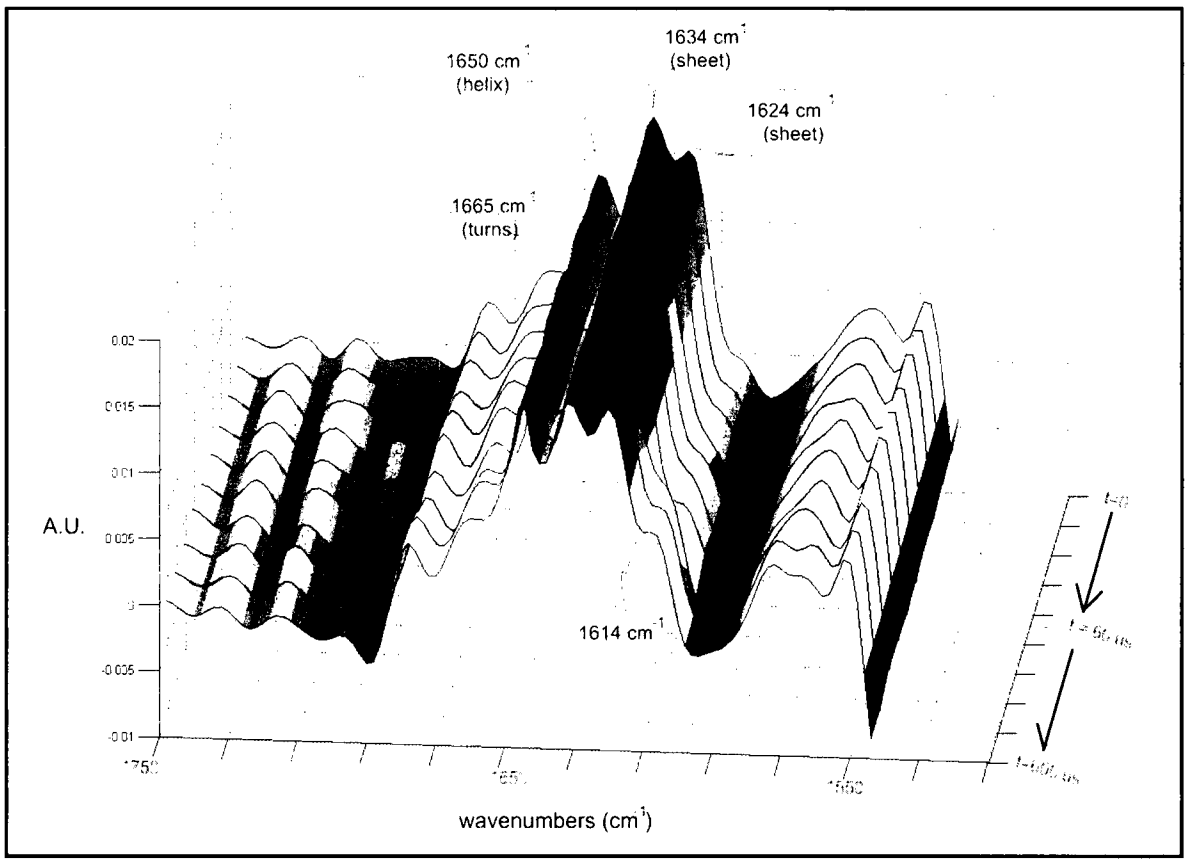

Figure 6-7: Stack plot showing a series of spectra (Self deconvoluted) obtained between 0 and 600 μs following TFE-BLG mixing. Each spectrum is separated by 60 μs

7. Conclusion

7.1 Contribution

The influence of geometric variations and flow speeds on the mixing performance of three microfluidic devices has been investigated in this thesis through numerical modeling and experimental verification. The mixers were fabricated by lithographic processing of SU-8 on polished calcium fluoride substrates. This enabled in-situ detection of the mixing process by using visible and infrared absorption spectroscopy. A dye-based visualization method was employed for numerically quantifying the mixing performance in each device. Based on the results, it was shown that a multi-lamination mixer performed better than a modified T-junction mixer and a flow-focusing mixer, in terms of mixing efficiency. Finally, rapid mixing of reagents in a multi-lamination mixer was used as a triggering mechanism to induce conformational changes in the secondary structure of β-Lactoglobulin. The progress of the reaction was monitored by time-resolved FTIR spectroscopy with the use of a focal plane array detector.

Based on the results of these experiments, the following conclusions can be drawn:

(i) The effect of a pH jump on β-Lactoglobulin

Upon a pH jump from pH 2 to neutral pH, the time-evolving spectra indicated a gradual loss in the α-helical content of β-Lactoglobulin. Furthermore, an increase was observed in the contributions from random coils and turns. These results were contrary to the findings of pH-induced changes under equilibrium conditions where a monomer→dimer transition was seen to occur above pH 2.

(ii) TFE-induced transition at low temporal resolution

At low flow speeds, premixing of reagents prevented the investigation of the early stages of the kinetic process. However, an increase in α-helical content and the formation of intermolecular β-sheet structures, indicative of protein aggregation, were observed during the first 10 ms.

(iii) TFE-induced transition at high temporal resolution

At higher flow rates, the α-helical content of the protein remains unchanged; however, the 1624 cm^{-1} absorption band ascribed to intramolecular β-strands and intermolecular β-sheets increases at the expense of the 1634 cm^{-1} band assigned anti-parallel

β-sheets. This was attributed to a high protein concentration that led to increased dimer-dimer interactions under the influence of the TFE. It was concluded that oligomerization between dimers precedes β→α transition, in terms of time-sequence, by an order of magnitude.

These results indicate that the multi-lamination mixer designed and fabricated in this study is well suited for investigations of protein dynamics on the micro- to millisecond timescale by time-resolved FTIR spectroscopy.

7.2 Future Work

Future studies geared towards the investigation of kinetic events can be classified into two categories: (a) Design and fabrication, and (b) Protein folding studies

There is a need to design efficient mixers capable of mixing at even faster flow rates. This will entail a combination of multi-lamination and flow focusing techniques to enhance diffusion rates. Furthermore, while SU-8 has proven to be a structurally viable polymer for fabricating microchannels, it has a tendency to unravel under strongly alkaline conditions. Therefore, there is a need to explore other epoxy-based polymers that display the mechanical strength of SU-8, while remaining chemically resistant to aggressive solutions.

The multi-lamination mixer developed in the course of this thesis can be used to investigate the folding kinetics of other globular proteins. Ideal candidates include Rnase, apomyoglobin, cytochrome C, and α-lactalbumin. Since time-resolved CD data exists for all the above proteins, it would be appropriate to confirm the results with complementary infrared experiments. Using a continuous flow mixer coupled to a FPA-FTIR imaging system, it is possible to attain an order of magnitude improvement in time resolutions over CD spectroscopy.

8. References

ANFINSEN, C. B., HABER, E., SELA, M. & WHITE, F. H., JR. (1961) The kinetics of formation of native ribonuclease during oxidation of the reduced polypeptide chain. *Proceedings of the National academy of Sciences of the United States of America,* 47, 1309-1314.

ANHOJ, T. A., JORGENSEN, A. M., ZAUNER, D. A. & HUEBNER, J. (2006) The effect of soft bake temperature on the polymerization of SU-8 photoresist. *Journal of Micromechanics and Microengineering,* 16, 1819-1824.

ARAI, M., ITO, K., INOBE, T., NAKAO, M., MAKI, K., KAMAGATA, K., KIHARA, H., AMEMIYA, Y. & KUWAJIMA, K. (2002) Fast compaction of alpha -lactalbumin during folding studied by stopped-flow x-ray scattering. *Journal of Molecular Biology,* 321, 121-132.

AREF, H. (1990) Chaotic Advection of Fluid Particles. *Royal Society of London Philosophical Transactions Series A,* 333, 273-288.

ARRONDO, J. L. R., YOUNG, N. M. & MANTSCH, H. H. (1988) The solution structure of concanavalin A probed by FT-IR spectroscopy. *Biochimica et Biophysica Acta, Protein Structure and Molecular Enzymology,* 952, 261-268.

BALBACH, J., FORGE, V., LAU, W. S., JONES, J. A., VAN NULAND, N. A. J. & DOBSON, C. M. (1997) Detection of residue contacts in a protein folding intermediate. *Proceedings of the National Academy of Sciences of the United States of America,* 94, 7182-7185.

BECNEL, C., DESTA, Y. & KELLY, K. (2005) Ultra-deep x-ray lithography of densely packed SU-8 features: I. An SU-8 casting procedure to obtain uniform solvent content with accompanying experimental results. *Journal of Micromechanics and Microengineering,* 15, 1249-1259.

BESSOTH, F. G., DEMELLO, A. J. & MANZ, A. (1999) Microstructure for efficient continuous flow mixing. *Analytical Communications,* 36, 213-215.

BHAGAT, A. A. S., PETERSON, E. T. K. & PAPAUTSKY, I. (2007) A passive planar micromixer with obstructions for mixing at low Reynolds numbers. *Journal of Micromechanics and Microengineering,* 17, 1017-1024.

BILSEL, O., KAYATEKIN, C., WALLACE, L. A. & MATTHEWS, C. R. (2005) A microchannel solution mixer for studying microsecond protein folding reactions. *Review of Scientific Instruments,* 76, 014302-014307.

CALLENDER, R. H., DYER, R. B., GILMANSHIN, R. & WOODRUFF, W. H. (1998) Fast events in protein folding: the time evolution of primary processes. *Annual Review of Physical Chemistry,* 49, 173-202.

CAMPO, A. D. & GREINER, C. (2007) SU-8: a photoresist for high-aspect-ratio and 3D submicron lithography. *Journal of Micromechanics and Microengineering,* 17, R81-R95.

CAPALDI, A. P., SHASTRY, M. C. R., KLEANTHOUS, C., RODER, H. & RADFORD, S. E. (2001) Ultrarapid mixing experiments reveal that Im7 folds via an on-pathway intermediate. *Natural Structural Biology,* 8, 68-72.

CARR, G. L., HANFLAND, M. & WILLIAMS, G. P. (1995) Midinfrared beamline at the National Synchrotron Light Source port U2B. AIP.

CASAL, H. L., KOHLER, U. & MANTSCH, H. H. (1988) Structural and conformational changes of beta-lactoglobulin B: an infrared spectroscopic study of the effect of pH and temperature. *Biochimica et Biophysica Acta,* 957, 11-20.

CHANCE, B., GIBSON, Q. H., EISENHARDT, R. H. & LONBERG-HOLM, K. K. (1964) Rapid Mixing and Sampling Techniques. *Science,* 146, 1697-1699.

CHEN, E., WEN, Y., LEWIS, J. W., GOLDBECK, R. A., KLIGER, D. S. & STRAUSS, C. E. M. (2005) Nanosecond laser temperature-jump optical rotatory dispersion: Application to early events in protein folding/unfolding. *Review of Scientific Instruments,* 76, 083120-083127.

CHENG, J.-Y., YEN, M.-H., WEI, C.-W., CHUANG, Y.-C. & YOUNG, T.-H. (2005) Crack-free direct-writing on glass using a low-power UV laser in the manufacture of a microfluidic chip. *Journal of Micromechanics and Microengineering,* 15, 1147-1156.

CHIEM, N. & HARRISON, D. J. (1997) Microchip-based capillary electrophoresis for immunoassays: analysis of monoclonal antibodies and theophylline. *Analytical Chemistry,* 69, 373-378.

CHUANG, Y. J., TSENG, F. G., CHENG, J. H. & LIN, W. K. (2003) A novel fabrication method of embedded micro-channels by using SU-8 thick-film photoresists. *Sensors and Actuators A: Physical,* 103, 64-69.

COLLEY, C. S., GRIFFITHS-JONES, S. R., GEORGE, M. W., SEARLE, M. S. & CLARK, I. P. (2000) Steady state and time-resolved IR spectroscopy of the native and unfolded states of bovine ubiquitin: protein stability and temperature-jump kinetic measurements of protein folding at low pH. *Chemical Communications,* X, 1493-1494.

CONRADIE, E. H. & MOORE, D. F. (2002) SU-8 thick photoresist processing as a functional material for MEMS applications. *Journal of Micromechanics and Microengineering,* 12, 368-374.

DAI, W., LIAN, K. & WANG, W. (2005) A quantitative study on the adhesion property of cured SU-8 on various metallic surfaces. *Microsystem Technologies,* 11, 526-534.

DONG, A., HUANG, P. & CAUGHEY, W. S. (1990) Protein secondary structures in water from second-derivative amide I infrared spectra. *Biochemistry,* 29, 3303-3308.

DONG, A., MATSUURA, J., ALLISON, S. D., CHRISMAN, E., MANNING, M. C. & CARPENTER, J. F. (1996) Infrared and Circular Dichroism Spectroscopic Characterization of Structural Differences between Beta-Lactoglobulin A and B. *Biochemistry,* 35, 1450-1457.

DONG, A., MATSUURA, J., MANNING, M. C. & CARPENTER, J. F. (1998) Intermolecular beta-Sheet Results from Trifluoroethanol-Induced Nonnative alpha-Helical Structure in beta-Sheet Predominant Proteins: Infrared and Circular Dichroism Spectroscopic Study. *Archives of Biochemistry and Biophysics,* 355, 275-281.

EFTINK, M. R. (1994) The use of fluorescence methods to monitor unfolding transitions in proteins. *Biophysical Journal,* 66, 482-501.

ENGLER, M., KOCKMANN, N., KIEFER, T. & WOIAS, P. (2004) Numerical and experimental investigations on liquid mixing in static micromixers. *Chemical Engineering Journal,* 101, 315-322.

FABIAN, H. & NAUMANN, D. (2004) Methods to study protein folding by stopped-flow FT-IR. *Methods,* 34, 28-40.

FOGOLARI, F., RAGONA, L., ZETTA, L., ROMAGNOLI, S., DE KRUIF, K. G. & MOLINARI, H. (1998) Monomeric bovine beta-lactoglobulin adopts a beta-barrel fold at pH 2. *FEBS Letters,* 436, 149-54.

FORGE, V., HOSHINO, M., KUWATA, K., ARAI, M., KUWAJIMA, K., BATT, C. A. & GOTO, Y. (2000) Is Folding of beta-Lactoglobulin Non-hierarchic? Intermediate with Native-like beta-Sheet and Non-native alpha-Helix. *Journal of Molecular Biology,* 296, 1039-1051.

GOBBY, D., ANGELI, P. & GAVRIILIDIS, A. (2001) Mixing characteristics of T-type microfluidic mixers. *Journal of Micromechanics and Microengineering,* 11, 126-132.

GREEN, J., HOLD, E., A. & KHAN, A. (2007) A review of passive and active mixing systems in microfluidic devices. *The International Journal of Multiphysics,* 1, 1-32.

HARDT, S. & SCHONFELD, F. (2007) *Microfluidic technologies for miniaturized analysis systems,* New York, Springer.

HARDT, S. & SCHÖNFELD, F. (2003) Laminar mixing in different interdigital micromixers: II. Numerical simulations. *AIChE Journal,* 49, 578-584.

HESSEL, V., HARDT, S., LÖWE, H. & SCHÖNFELD, F. (2003) Laminar mixing in different interdigital micromixers: I. Experimental characterization. *AIChE Journal,* 49, 566-577.

HEIDERMANN, P. (2005) Microchem Support Staff. Email to the author

HINSMANN, P., FRANK, J., SVASEK, P., HARASEK, M. & LENDL, B. (2001a) Design, simulation and application of a new micromixing device for time resolved infrared spectroscopy of chemical reactions in solution. *Lab Chip,* 1, 16-21.

HINSMANN, P., HABERKORN, M., FRANK, J., SVASEK, P., HARASEK, M. & LENDL, B. (2001b) Time-Resolved FT-IR Spectroscopy of Chemical Reactions in Solution by Fast Diffusion-Based Mixing in a Micromachined Flow Cell. *Applied Spectroscopy,* 55, 241-251.

HOLDEN, M. A., KUMAR, S., BESKOK, A. & CREMER, P. S. (2003) Microfluidic diffusion diluter: bulging of PDMS microchannels under pressure-driven flow*. *Journal of Micromechanics and Microengineering,* 13, 412-418.

HOURY, W. A., ROTHWARF, D. M. & SCHERAGA, H. A. (1996) Circular Dichroism Evidence for the Presence of Burst-Phase Intermediates on the Conformational Folding Pathway of Ribonuclease A&#x2020. *Biochemistry,* 35, 10125-10133.

ICHIKI, T., SUGIYAMA, Y., TAURA, R., KOIDESAWA, T. & HORIIKE, Y. (2003) Plasma applications for biochip technology. *Thin Solid Films,* 435, 62-68.

JACKMAN, R. J., FLOYD, T. M., GHODSSI, R., SCHMIDT, M. A. & JENSEN, K. F. (2001) Microfluidic systems with on-line UV detection fabricated in photodefinable epoxy. *Journal of Micromechanics and Microengineering,* 11, 263-269.

JACKSON, M. & MANTSCH, H. H. (1992) Halogenated alcohols as solvents for proteins: FTIR spectroscopic studies. *Biochimica et Biophysica Acta,* 1118, 139-43.

JACOB, M., HOLTERMANN, G., PERL, D., REINSTEIN, J., SCHINDLER, T., GEEVES, M. A. & SCHMID, F. X. (1999) Microsecond Folding of the Cold Shock Protein Measured by a Pressure-Jump Technique&#x2020. *Biochemistry,* 38, 2882-2891.

JACOBSON, S. C. & RAMSEY, J. M. (1997) Electrokinetic Focusing in Microfabricated Channel Structures. *Analytical Chemistry,* 69, 3212-3217.

JENNINGS, P. A. & WRIGHT, P. E. (1993) Formation of a molten globule intermediate early in the kinetic folding pathway of apomyoglobin. *Science,* 262, 892-896.

JEON, N. L., DERTINGER, S. K. W., CHIU, D. T., CHOI, I. S., STROOCK, A. D. & WHITESIDES, G. M. (2000) Generation of Solution and Surface Gradients Using Microfluidic Systems. *Langmuir,* 16, 8311-8316.

JOHNSON, T. J., ROSS, D. & LOCASCIO, L. E. (2002) Rapid Microfluidic Mixing. *Analytical Chemistry,* 74, 45-51.

KAUFFMANN, E., DARNTON, N. C., AUSTIN, R. H., BATT, C. & GERWERT, K. (2001) Lifetimes of intermediates in the beta-sheet to alpha-helix transition of beta-lactoglobulin by using a diffusional IR mixer. *Proceedings of the National Academy of Sciences of the United States of America,* 98, 6646-6649.

KAUN, N., VELLEKOOP, M. J. & LENDL, B. (2006) Time-Resolved Fourier Transform Infrared Spectroscopy of Chemical Reactions in Solution Using a Focal Plane Array Detector. *Applied Spectroscopy,* 60, 1273-1278.

KIEFHABER, T., SCHMID, F. X., WILLART, K., ENGELBORGHS, Y. & CHAFFOTTE, A. (1992) Structure of a rapidly formed intermediate in ribonuclease T1 folding. *Protein Science,* 1, 1162-1172.

KNIGHT, J. B., VISHWANATH, A., BRODY, J. P. & AUSTIN, R. H. (1998) Hydrodynamic Focusing on a Silicon Chip: Mixing Nanoliters in Microseconds. *Physical Review Letters,* 80, 3863-3866.

KOCH, M., WITT, H., EVANS, A. G. R. & BRUNNSCHWEILER, A. (1999) Improved characterization technique for micromixers. *Journal of Micromechanics and Microengineering,* 9, 156-158.

KOCKMANN, N., KIEFER, T., ENGLER, M. & WOIAS, P. (2006) Convective mixing and chemical reactions in microchannels with high flow rates. *Sensors and Actuators B: Chemical,* 117, 495-508.

KRIMM, S. & BANDEKAR, J. (1986) Vibrational spectroscopy and conformation of peptides, polypeptides, and proteins. *Advances in Protein Chemistry,* 38, 181-364.

KUBELKA, J., HOFRICHTER, J. & EATON, W. A. (2004) The protein folding 'speed limit'. *Current Opinion in Structural Biology,* 14, 76-88.

KULKA, S., KAUN, N., BAENA, J. R., FRANK, J., SVASEK, P., MOSS, D., VELLEKOOP, M. J. & LENDL, B. (2004) Mid-IR synchrotron radiation for molecular specific detection in microchip-based analysis systems. *Analytical and Bioanalytical Chemistry,* 378, 1735-1740.

KUWAJIMA, K., YAMAYA, H., MIWA, S., SUGAI, S. & NAGAMURA, T. (1987) Rapid formation of secondary structure framework in protein folding studied by stopped-flow circular dichroism. *FEBS Letters,* 221, 115-8.

KUWAJIMA, K., YAMAYA, H. & SUGAI, S. (1996) The burst-phase intermediate in the refolding of beta-lactoglobulin studied by stopped-flow circular dichroism and absorption spectroscopy. *Journal of Molecular Biology,* 264, 806-822.

KUWATA, K., HOSHINO, M., FORGE, V., ERA, S., BATT, C. & GOTO, Y. (1999) Solution structure and dynamics of bovine beta-lactoglobulin A. *Protein Science,* 8, 2541-2545.

KUWATA, K., SHASTRY, R., CHENG, H., HOSHINO, M., BATT, C. A., GOTO, Y. & RODER, H. (2001) Structural and kinetic characterization of early folding events in beta-lactoglobulin. *Natural Structural Biology,* 8, 151-155.

LAPIDUS, L. J., YAO, S., MCGARRITY, K. S., HERTZOG, D. E., TUBMAN, E. & BAKAJIN, O. (2007) Protein Hydrophobic Collapse and Early Folding Steps Observed in a Microfluidic Mixer. *Biophysical Journal,* 93, 218-224.

LARIONOV, A. L. & MALKIN, B. Z. (1975) Thermal expansion of calcium fluoride. *Physica B: Condensed Matter,* 68, K103-K105.

LEFÈVRE, T. & SUBIRADE, M. (2001) Molecular structure and interaction of biopolymers as viewed by Fourier transform infrared spectroscopy: model studies on [beta]-lactoglobulin. *Food Hydrocolloids,* 15, 365-376.

LARSON, S. (2006) SU-8 Properties. <http://memscyclopedia.org/su8.html>

LI, S., FREIDHOFF, C. B., YOUNG, R. M. & GHODSSI, R. (2003) Fabrication of micronozzles using low-temperature wafer-level bonding with SU-8. *Journal of Micromechanics and Microengineering,* 13, 732-728.

LI, X., ABE, T. & ESASHI, M. (2001) Deep reactive ion etching of Pyrex glass using SF6 plasma. *Sensors and Actuators A: Physical,* 87, 139-145.

LIN, C.-H., LEE, G.-B., CHANG, B.-W. & CHANG, G.-L. (2002) A new fabrication process for ultra-thick microfluidic microstructures utilizing SU-8 photoresist. *Journal of Micromechanics and Microengineering,* 12, 590-597.

LÜDEKE, S., FONFRÍA, V. A. L., SIEBERT, F. & VOGEL, R. (2006) Time-resolved rapid-scan Fourier transform infrared difference spectroscopy on a noncyclic photosystem: Rhodopsin photointermediates from Lumi to Meta II. *Biopolymers,* 83, 159-169.

MALIC, L. (2005) Investigation of an integrated optical detection system for fluorescence and absorption spectroscopy. McGill University

MARINKOVIC, N. S., ADZIC, A. R., SULLIVAN, M., KOVACS, K., MILLER, L. M., ROUSSEAU, D. L., YEH, S.-R. & CHANCE, M. R. (2000) Design and implementation of a rapid-mixer flow cell for time-resolved infrared microspectroscopy. *Review of Scientific Instruments,* 71, 4057-4060.

MENGEAUD, V., JOSSERAND, J. & GIRAULT, H. H. (2002) Mixing processes in a zigzag microchannel: finite element simulations and optical study. *Analytical Chemistry,* 74, 4279-86.

NGUYEN, N.-T. & WU, Z. (2005) Micromixers-a review. *Journal of Micromechanics and Microengineering,* 15, R1-R16.

PAN, T., KELLY, R. T., ASPLUND, M. C. & WOOLLEY, A. T. (2004) Fabrication of calcium fluoride capillary electrophoresis microdevices for on-chip infrared detection. *Journal of Chromatography,* 1027, 231-235.

PAPIZ, M. Z., SAWYER, L., ELIOPOULOS, E. E., NORTH, A. C., FINDLAY, J. B., SIVAPRASADARAO, R., JONES, T. A., NEWCOMER, M. E. & KRAULIS, P. J. (1986) The structure of beta-lactoglobulin and its similarity to plasma retinol-binding protein. *Nature,* 324, 383-385.

PESSEN, H., PURCELL, J. M. & FARRELL, H. M., JR (1985) Proton relaxation rates of water in dilute-solutions of beta-lactoglobulin - Determination of cross relaxation and correlation with structural changes by the use of 2 genetic-variants of a self associating globular protein. *Biochimica et Biophysica Acta, Protein Structure and Molecular Enzymology,* 828, 1-12.

REGENFUSS, P., CLEGG, R. M., FULWYLER, M. J., BARRANTES, F. J. & JOVIN, T. M. (1985) Mixing liquids in microseconds. *Review of Scientific Instruments,* 56, 283-290.

REIERSEN, H. (2000) Trifluoroethanol may form a solvent matrix for assisted hydrophobic interactions between peptide side chains. *Protein Engineering,* 13, 739-743.

REINSTADLER, D., FABIAN, H., BACKMANN, J. & NAUMANN, D. (1996) Refolding of thermally and urea-denatured ribonuclease A monitored by time-resolved FTIR spectroscopy. *Biochemistry,* 35, 15822-15830.

REYES, D. R., IOSSIFIDIS, D., AUROUX, P.-A. & MANZ, A. (2002) Micro Total Analysis Systems. 1. Introduction, Theory, and Technology. *Analytical Chemistry,* 74, 2623-2636.

RODER, H., MAKI, K. & CHENG, H. (2006) Early events in protein folding explored by rapid mixing methods. *Chemical Reviews,* 106, 1836-61.

RODER, H. & SHASTRY, M. R. (1999) Methods for exploring early events in protein folding. *Current Opinion in Structural Biology,* 9, 620-626.

RONGGUI, S. & RIGHINI, G. C. (1991) Characterization of reactive ion etching of glass and its applications in integrated optics. *Journal of Vacuum Science & Technology A: Vacuum, Surfaces, and Films,* 9, 2709-2712.

SCHWARZ, M. A. & HAUSER, P. C. (2001) Recent developments in detection methods for microfabricated analytical devices. *Lab Chip,* 1, 1-6.

SEMISOTNOV, G. V., RODIONOVA, N. A., RAZGULYAEV, O. I., UVERSKY, V. N., GRIPAS, A. F. & GILMANSHIN, R. I. (1991) Study of the "molten globule" intermediate state in protein folding by a hydrophobic fluorescent probe. *Biopolymers,* 31, 119-28.

SHASTRY, M. C., SAUDER, J. M. & RODER, H. (1998) Kinetic and Structural Analysis of Submillisecond Folding Events in Cytochrome c. *Accounts of Chemical Research,* 31, 717-725.

SMITH, T., BONING, D., FANG, S., SHINN, G. & STEFANI, J. (1999) *A study of within-wafer non-uniformity metrics,* Piscataway, NJ, USA, Purchased from: IEEE Service Center Single Publication Sales Unit.

SONNICHSEN, F. D., VAN EYK, J. E., HODGES, R. S. & SYKES, B. D. (1992) Effect of trifluoroethanol on protein secondary structure: an NMR and CD study using a synthetic actin peptide. *Biochemistry,* 31, 8790-8.

STROOCK, A. D., DERTINGER, S. K. W., AJDARI, A., MEZIC, I., STONE, H. A. & WHITESIDES, G. M. (2002) Chaotic Mixer for Microchannels. *Science,* 295, 647-651.

TROULLIER, A., REINSTADLER, D., DUPONT, Y., NAUMANN, D. & FORGE, V. (2000) Transient non-native secondary structures during the refolding of alpha-lactalbumin detected by infrared spectroscopy. *Natural Structural Biology,* 7, 78-86.

UHRINOVA, S., SMITH, M. H., JAMESON, G. B., UHRIN, D., SAWYER, L. & BARLOW, P. N. (2000) Structural changes accompanying pH-induced dissociation of the beta-lactoglobulin dimer. *Biochemistry,* 39, 3565-74.

UJIIE, T., KIKUCHI, T., ICHIKI, T. & HORIIKE, Y. (2000) Fabrication of Quartz Microcapillary Electrophoresis Chips Using Plasma Etching. *Japanese Journal of Applied Physics,* 39, 3677-3682.

VETTIGER, P., BRUGGER, J., DESPONT, M., LORENZ, H., FAHRNI, N. & RENAUD, P. (1998) High-aspect-ratio, ultrathick, negative-tone near-UV photoresist and its applications for MEMS. *Sensors and Actuators A: Physical,* 64, 33-39.

WANG, H., IOVENITTI, P., HARVEY, E. & MASOOD, S. (2002) Optimizing layout of obstacles for enhanced mixing in microchannels. *Smart Materials and Structures,* 11, 662-667.

WESTWOOD, S. M., JAFFER, S. & GRAY, B. L. (2008) Enclosed SU-8 and PDMS microchannels with integrated interconnects for chip-to-chip and world-to-chip connections. *Journal of Micromechanics and Microengineering,* 18, 064014-064023.

WHITE, A. J., DRABBLE, K. & WHARTON, C. W. (1995) A stopped-flow apparatus for infrared spectroscopy of aqueous solutions. *Biochemical Journal,* 306, 843-849.

WIGGINS, S. & OTTINO, J. M. (2004) Foundations of chaotic mixing. *Philosophical Transactions. Series A, Mathematical, Physical, and Engineering Sciences,* 362, 937-970.

WONG, S. H., BRYANT, P., WARD, M. & WHARTON, C. (2003) Investigation of mixing in a cross-shaped micromixer with static mixing elements for reaction kinetics studies. *Sensors and Actuators B: Chemical,* 95, 414-424.

WONG, S. H., WARD, M. C. L. & WHARTON, C. W. (2004) Micro T-mixer as a rapid mixing micromixer. *Sensors and Actuators B: Chemical,* 100, 359-379.

YANG, R., JIANG, J., MENG, W. J. & WANG, W. (2006) Numerical simulation and fabrication of microscale, multilevel, tapered mold inserts using UV-Lithographie, Galvanoformung, Abformung (LIGA) technology. *Microsystem Technologies,* 12, 545-553.